Taking Snapshots of Atomic Wave Functions with a Photoionization Microscope

Aneta S. Stodolna

Cover: Pictures on the cover show three photoelectron images of the hydrogen atom, which were recorded with the use of a photoionization microscope, for slightly different excitation energies (increasing from left to right). The central image diverges significantly in its shape and size as in this particular case a Stark state is excited and an atomic wave function dominates the observed structure. This image, which directly shows an electronic orbital in hydrogen is the most important result of the thesis and has received a significant attention in the scientific and social media all over the world (e.g. 70.000 'likes' on Facebook).

ISBN: 978-90-77209-80-6
Copyright © 2014 by Aneta S. Stodolna.
An electronic copy of this thesis is available at www.amolf.nl/publications.

Taking Snapshots of Atomic Wave Functions with a Photoionization Microscope

Proefschrift

ter verkrijging van de graad van doctor
aan de Radboud Universiteit Nijmegen
op gezag van de rector magnificus prof. mr. S.C.J.J. Kortmann,
volgens besluit van het college van decanen
in het openbaar te verdedigen op vrijdag 20 juni 2014
om 10.30 uur precies

door

Aneta Sylwia Stodolna

geboren op 20 maart 1984
te Ostroda, Polen

Promotor:	Prof. dr. M.J.J. Vrakking
Manuscriptcommissie:	Prof. dr. D.H. Parker Prof. dr. H. Helm (Freiburg University, DE) Prof. dr. H.J. Bakker (FOM Institute AMOLF)

The work described in this thesis was performed at the FOM Institute for Atomic and Molecular Physics (AMOLF), Science Park 104, 1098 XG Amsterdam, The Netherlands. This work is part of the research programme of the 'Stichting voor Fundamenteel Onderzoek der Materie (FOM)', which is financially supported by the 'Nederlandse Organisatie voor Wetenschappelijk Onderzoek (NWO)'.

To My Husband

Contents

1 Introduction

1.1 Old Quantum Mechanics

Towards the end of the 19^{th} century various branches of physics had been integrated in a general and coherent theory – *Classical Physics*. The classical program divided objects into two categories: *matter* – perfectly localizable corpuscles obeying Newton's laws of classical mechanics and *radiation* – exhibiting a wave-like behavior, manifested in the phenomena of interference and diffraction, and following Maxwell's laws of electromagnetism. The undeniable success of classical physics lies in the fact that almost all known phenomena at that very time could be explained by the theory of matter and radiation. Whenever the explanation could not be found the failure was attributed to the mathematical difficulties in solving the problem – but the classical program was never questioned.

Physicists of the classical period, proceeding towards greater unity of various branches of science, attributed more unity to the classical theory than it essentially had. The most striking example comes from a consideration of the wave propagation phenomenon. First observed for matter, e.g. surface waves of a liquid, provided physicists with a clue that similarly to surface waves on the water also light needs a medium to transmit its waves. This medium, the *aether*, was assumed to have a set of highly unusual properties since light and material bodies pass through it without any drag or friction [1]. In the 19^{th} century numerous experiments did not reveal the nature of the expected medium. Moreover, the famous Michelson - Morley experiment in 1887 [2], designed to measure the speed of the aether with high precision, gave a negative result that was later explained by Einstein [3] in 1905 within the framework of the special theory of relativity. Finally the concept of the aether was abandoned.

At the turn of the 20^{th} century various experiments exploring the structure of matter and its interaction with electromagnetic radiation brought unexpected results which could not be understood in a classical manner. It became evident that the classical physics is not as general as physicists believed.

The first disagreement emerged by studying radiation of the *black body*. According to the classical physics this is a body that absorbs all incident electromagnetic radiation and while being at thermal equilibrium emits radiation proportional to frequency squared [4]. Consequently, with an increase of frequency the emitted ra-

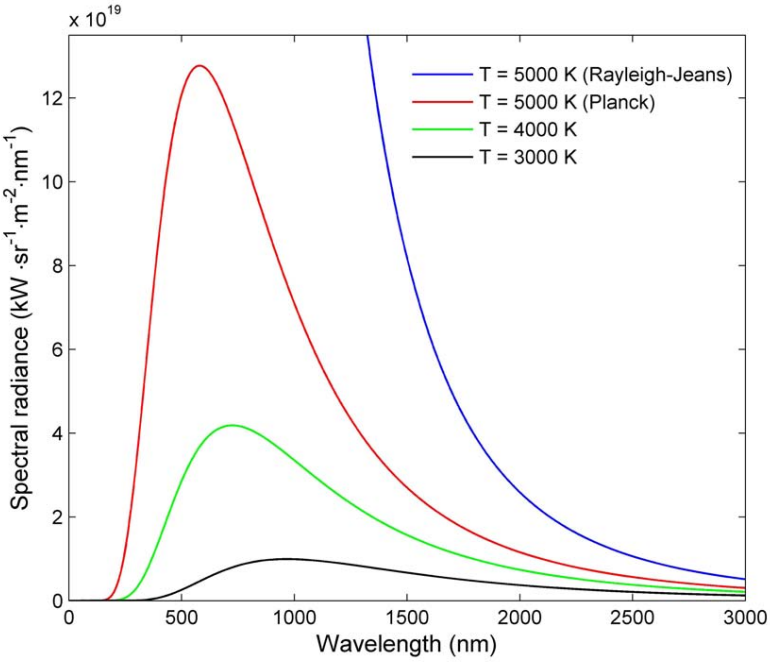

Figure 1.1: Spectral radiance distribution of the black body radiation as a function of wavelength calculated using a classical formula of the Rayleigh-Jeans law (blue curve) and the Planck's law (red, green and black curves) for different temperatures. As the black body temperature increases the intensity maximum shifts to shorter wavelengths.

diation goes to infinity leading to the so-called "ultraviolet catastrophe" (see blue curve in Fig.1.1). However, experiments showed that black body radiation has a continuous frequency spectrum with a characteristic frequency peak, which shifts with the black body's temperature (red, green and black curves in Fig.1.1). In 1900 Planck succeeded in calculating the radiation curve by postulating that the energy exchange between matter and radiation takes place by discrete and indivisible portions of energies - *quanta* [5, 6]. Planck postulated that the quantum of energy must be proportional to the frequency ν of the radiation via:

$$E = h\nu, \tag{1.1}$$

where h is the proportionality factor known as the Planck's constant. The hypothesis of quanta seemed unacceptable to most of the contemporary physicists and the Planck's success was perceived as a lucky mathematical trick. However, Planck's theory was to be confirmed by numerous experiments investigating matter and radiation on the microscopic scale.

With the discovery of radioactivity in 1896 [7] first properties of atomic nuclei

were investigated. One year later Thomson while working with cathode rays discovered the electron [8] and in 1904 proposed the "plum pudding model" of the atom [9]. According to this model the atom is composed of electrons surrounded by a soup of positive charge that balances negative charge of electrons. In 1911 Rutherford directed a beam of alpha particles on a thin gold foil and by studying the scattered particles proposed a first planetary model of the atom [10]. The Rutherford atom comprises a positively charged, tiny and heavy nucleus and surrounding electrons. However, this model did not explain the atom's stability and predicted a continuous emission/absorption spectrum of light by the atom. The latter was contradictory with experiments showing that emission and absorption spectra are composed of narrow spectral lines. In 1913 Bohr [11] succeeded in explaining the atomic spectra by postulating that the energy levels of an atom are quantized. Bohr introduced the idea that electrons do not travel freely around the nucleus but move along a certain number of orbits (stationary states) with a well-defined energy. Within the framework of Bohr's theory an electron can drop from a high-energy state E_i to a lower state E_k by emitting a photon $h\nu$, which frequency satisfies the relation:

$$h\nu = E_i - E_k. \tag{1.2}$$

Similarly, in the presence of light the atom in a low-energy state E_k may absorb a photon $h\nu$ and undergo a transition to a higher energy state E_j provided that the total energy is conserved:

$$h\nu = E_j - E_k. \tag{1.3}$$

In 1914 the experiment by Franck and Hertz [12] on inelastic collisions between electrons and atoms brought another confirmation of the quantization of atomic energy levels. Two years later Sommerfeld [13] extended the Bohr's theory by introducing elliptical orbits, the orientation of the orbital plane (spatial quantization) and a relativistic correction for the mass of the electron giving birth to what is now known as the *Old Quantum Mechanics*. The Bohr-Sommerfeld theory provided an explanation of the Stark effect [14, 15], the ordinary Zeeman effect [16] and the fine structure of the hydrogen spectrum. Nevertheless, this theory contained errors, ambiguities, contradictions and failed with aperiodic systems [17]. Furthermore, the quantization rules were determined in an empirical manner.

1.2 The Schrödinger equation

In 1923 de Broglie [18] stated the hypothesis that the wave-corpuscle duality is a general property of microscopic objects. Hence, as light waves are known to have corpuscular properties, shown by Einstein in the photoelectric effect [19], moving particles should as well have wave properties given by de Broglie's equation:

$$\lambda = \frac{h}{p}, \tag{1.4}$$

where λ is the wavelength of the particle and p is its momentum. At about the same time Heisenberg [20] introduced a new representation of quantum mechanics – *Matrix Mechanics*. In this new theory only physically observable quantities are represented by matrices which, in contrast to the classical mechanics, obey a non-commutative algebra. In the meantime, Schrödinger [21], while working on de Broglie's theory of *Wave Mechanics*, obtained the equation of propagation of a wave function ψ representing a quantum system:

$$i\hbar\frac{\partial}{\partial t}\psi = \widehat{H}\psi, \tag{1.5}$$

where i is the imaginary unit, $\hbar$ is the reduced Planck constant and $\widehat{H}$ is the Hamiltonian operator. The undeniable power of the Schrödinger equation lies in the fact that by knowing the wave function ψ one could predict and describe all dynamical properties of the quantum system at a given instant of time t. Moreover, Schrödinger has shown that both matrix mechanics and wave mechanics, although mathematically different, lead to the same result and are equivalent.

Soon after Schrödinger's publication, Born interpreted the wave function ψ in the wave equation by stating that since ψ has a certain spatial extension one cannot attribute to a quantum particle a precise position (or momentum) but can only define a probability of finding the particle in a given region of space (or momentum space) [22]. The probability density $P(r)$, describing a probability of finding the particle in the volume element $(r, r + dr)$, is related to the wave function $\psi(r)$ via:

$$P(r) = \psi^*(r)\psi(r) = |\psi(r)|^2, \tag{1.6}$$

where $\psi^*(r)$ denotes the complex conjugate of $\psi(r)$. In other words, relation (1.6) says that the larger the probability of the presence of the particle the more intense the wave at that point is.

Few months later Heisenberg formulated a general consequence of the statistical interpretation of the wave-corpuscle nature of quantum objects – the uncertainty principle – which says that it is impossible, under any circumstances, to attribute simultaneously to the quantum particle a precise position and a precise momentum [23]. Finally Bohr completed the theory of Quantum Mechanics with the complementarity principle, which indicates that it is not possible to observe both the wave and corpuscle aspects of quantum objects simultaneously, but together they present a full description of the microscopic objects [24].

Consequently, a new theoretical model of the hydrogen atom was presented, where the probability of finding the electron in an element volume dV is calculated by means of the Schrödinger equation (1.5). With boundary conditions imposed upon the wave function ψ, the allowed solutions of the wave equation create a discrete set of solutions, so-called eigenfunctions, where each of them represents an energy state of the atom. There exists an analytical solution of the Schrödinger equation for the hydrogen atom if the electron position is given in spherical coordinates r, φ

and θ. Consequently, the wave function ψ might be replaced by a product of three functions along each coordinate, i.e. by:

$$\psi(r, \varphi, \theta) = R(r) \cdot \Phi(\varphi) \cdot \Theta(\theta), \tag{1.7}$$

leading to separation of the wave equation into three total differential equations. As a result, three separation constants are introduced, which are linked to three quantum numbers n, m and l. These numbers can be associated with quantum numbers introduced by the Bohr-Sommerfeld model, i.e. n is the total quantum number that characterizes the basic energy level for the electron and describes the size of the orbital, l - the azimuthal quantum number characterizes the electron's angular momentum and indicates the shape of the orbital, m - the magnetic quantum number specifies the orientation in space of the orbital. In Quantum Mechanics these numbers have values:

$$\begin{aligned} &n = 1, 2, 3, \ldots, \infty, \\ &l = 0, 1, 2, \ldots, n-1, \\ &m = 0, \pm 1, \pm 2, \ldots, \pm l. \end{aligned} \tag{1.8}$$

For a given set of the quantum numbers n, l and m the complete eigenfunction ψ_{nlm}, which satisfies the wave equation, is of the form [25]:

$$\psi_{nlm} = \frac{e^{im\varphi}}{\sqrt{2\pi}} \sqrt{\frac{(2l+1)(l-|m|)!}{2(l+|m|)!}} (sin^{|m|}\theta) P_l^{|m|}(cos\theta) \cdot \\ \cdot \sqrt{\frac{4(n-l-1)!Z^3}{[(n+l)!]^3 n^4 a_0^3}} \left(\frac{2Zr}{na_0}\right)^l e^{\frac{-Zr}{na_0}} L_{n+a}^{2l+1}\left(\frac{2Zr}{na_0}\right), \tag{1.9}$$

where Z is the atomic number, a_0 is the Bohr radius, $P_l^{|m|}(cos\theta)$ is the associated Legendre polynomial and $L_{n+a}^{2l+1}\left(\frac{2Zr}{na_0}\right)$ is the associated Laguerre polynomial.

Fig.1.2 shows the probability density, calculated using Eq. (1.9), for the hydrogen atom in the states: $n = 6$, $l = 0 \rightarrow 5$ and $m = 0$. One can see that for different values of the azimuthal quantum number l orbitals have different shapes, which are best described as spherical ($l = 0$), polar ($l = 1$), or cloverleaf ($l = 2$). As the value of the angular quantum number becomes larger more complex shapes are observed. Moreover, the azimuthal quantum number gives the number of planar nodes going through the nucleus placed at the center of the coordinate system. Closer inspection of plotted charge distributions reveals that the nodal lines of the eigenfunctions are seen to be concentric circles and radii.

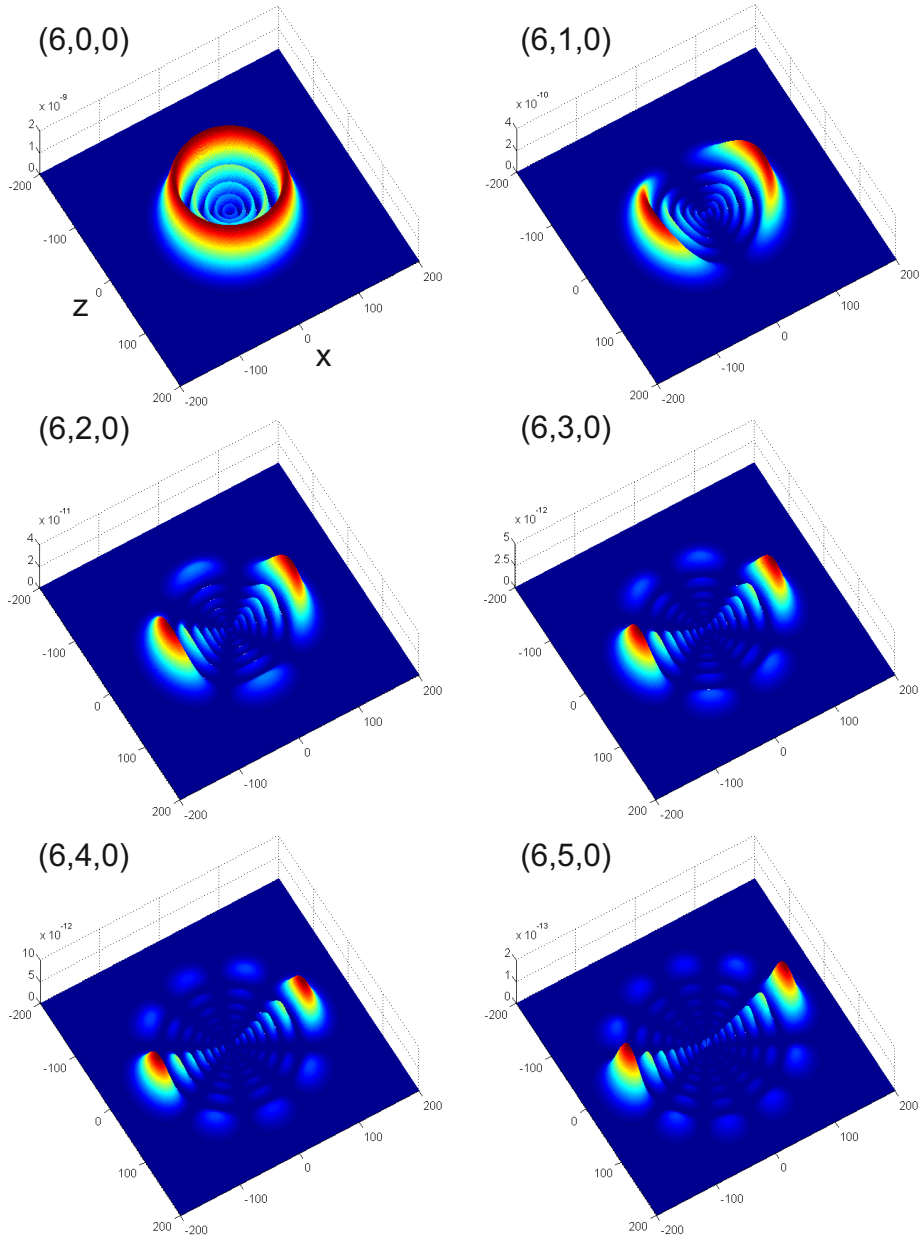

Figure 1.2: Charge distributions for the hydrogen atom in the spherical states (n,l,m) = (6,0,0), (6,1,0), (6,2,0), (6,3,0), (6,4,0) and (6,5,0). Note that the probability-density distribution has been multiplied by r for a better visibility.

1.3 Attempts towards measuring ψ

Although the wave function ψ, also known as a "quantum state", is a central concept of Quantum Mechanics its observation remains elusive. By using the wave function to calculate the expectation value of experimental observables, one can obtain properties like the position of an atom or the momentum of the electron. However, according to the Heisenberg uncertainty principle these projections only reveal a fraction of the information encoded in the wave function and destroy other intriguing features as superposition or entanglement. It has been shown [26] that it is impossible to determine a completely unknown wave function of a single state. Nevertheless, in the last decades different direct and indirect experimental methods for imaging the wave function of photons, nuclei, atoms and molecules have been developed.

The oldest method of mapping wave functions of atoms, molecules and nuclei employs collision experiments. A possible experimental setup requires a beam of fast particles (electrons or protons) and a target material M. When the impact particle has high kinetic energy it can kick out a particle from the target at large polar angles ensuring that the momentum transfer in the inelastic collision is maximized and very large. The recoil momentum of the ion M^+ is equal and opposite in sign to the momentum of the target particle immediately prior to the "knock-out". By varying the azimuthal angle between the two outgoing particles for each characteristic binding energy a measurement of the cross-section directly gives the momentum distribution of the target particle $|\psi(p)|^2$ prior to knock-out. This technique of electron momentum spectroscopy (EMS) (i.e., binary (e, 2e) spectroscopy) allowed measurement of the momentum distribution of electrons in the ground state of atomic hydrogen [27] as well as in helium and other many-electron atoms [28], and small molecules [29]. More recently a spherically averaged Dyson orbital electron momentum density distribution of the highest occupied molecular orbital (HOMO) has been observed for different molecules [30]. Similarly to the (e, 2e) reaction (p, 2p), (p, pn), (e, e'p), (γ, p) and (p, pα) reactions have been used to map wave functions of nuclei [31, 32].

Photons are of particular interest to quantum information processing (QIP) as owing to their mobility they are irreplaceable carriers of information in quantum communication networks [33]. A successfully implementation of photons in QIP requires inter alia a detail characterization of a quantum state. This can be accomplished by means of tomographic methods, where the wave function of a quantum system is estimated by employing reconstruction techniques. Quantum-state tomography (QST) by taking *many* sets of measurements allows obtaining a *quorum* - a set of observables providing tomographically complete information about a quantum state. The first experimental demonstration of optical QST in 1993 [34] allowed the reconstruction of the Wigner function and the density matrix of a squeezed state of light. Consecutive tomographic experiments provided complete information of different quantum states e.g. the single-photon Fock states [35] or the squeezed "Schrödinger cats" [36]. Alternatively, one can measure the wave function ψ of a single photon by means of so-called weak-measurements [37]. In this method photons with the same initial wave function $\psi(x)$ first undergo a weak measurement of

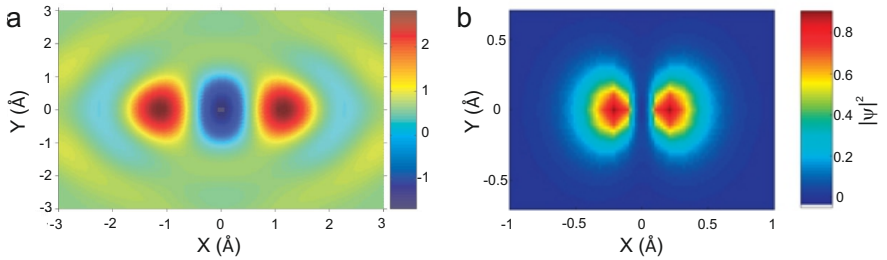

Figure 1.3: Examples of a molecular and an atomic orbital measured by means of orbital tomography. (a) Reconstructed wave function of the HOMO of N_2 obtained from a tomographic inversion of the high-harmonic spectra [38]. Note that this wave function has both positive and negative values meaning that this image shows $\psi(x)$ up to an arbitrary phase. (b) Retrieved square of the wave function $|\psi(r)|^2$ of the 2p orbital in Ne reconstructed from the high-harmonic spectrum [39].

a transverse position, which does not disturb the state, and then their momenta are measured normally (a strong measurement). Although this method is called by the authors as "direct", it only means that this method is free from complicated sets of measurements and computations.

Tomographic methods found also applications in mapping the highest-lying orbitals of molecules, which are of particular interest as they are responsible for chemical properties. For example the HOMO and LUMO (lowest unoccupied molecular orbital) can be reconstructed for molecules, placed on a thin film, by means of the ultraviolet angle-resolved photoelectron spectroscopy (ARPES) [40]. The advantage of ARPES is that it works for low photon energies, minimizing damage to the sample, and that it does not require a tunable photon source. Another approach has been shown by the group of Corkum *et al.* [38] who used high-harmonics, generated from intense femtosecond laser pulses focused on aligned N_2 molecules, to obtain the full three-dimensional shape of the HOMO. A crucial element of this tomographic technique is that it makes use of the high-harmonic emission process from aligned molecules, which is known to be sensitive to the spatial structure of the electronic wave function [41]. In brief, an intense low-frequency laser ionizes an aligned molecule and consequently a fraction of electron wave function tunnels from the HOMO. When the laser field direction reverses this electron wave packet ψ_c is driven back to the molecule where it overlaps with the remaining portion of the initial wave function ψ_g. By coherent addition of ψ_c and ψ_g a dipole is induced, seen as the asymmetric electron density distribution, which oscillations result in emission of high harmonic radiation. The high harmonic spectra, measured for different angles between the molecular axis and the re-colliding electron, are tomographically inverted and the initial wave function ψ_g is reconstructed (see Fig. 1.3a). However, there are two main limitations of this method: (1) the orbital must be fixed in the laboratory frame and (2) the coupling between ionization in the field and the recollision process must be disentangled. Therefore, the orbital tomography in this form is only applicable for

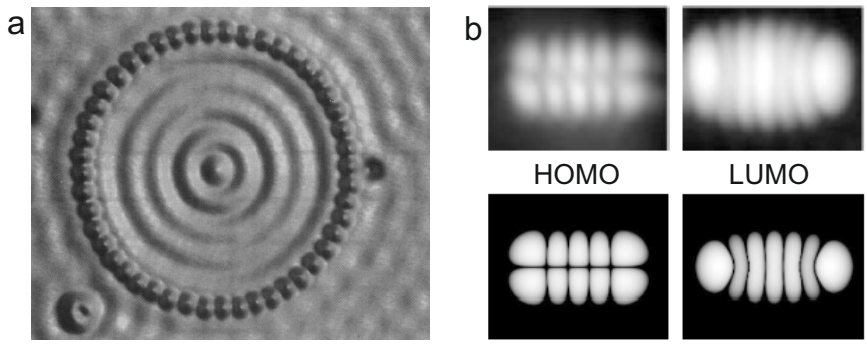

Figure 1.4: (a) Spatial image of a quantum corral, built by placing 48 Fe atoms into a ring on a metal surface, with visible eigenstates obtained by means of STM [45]. (b) Direct comparison between the experimental STM images of the highest-lying orbitals of a molecule placed on an insulating layer (top panel) with the calculated electron densities $|\psi(r)|^2$ for a free molecule (bottom panel) [46].

systems that can be naturally aligned and only for the simplest molecular orbitals as the HOMO and HOMO-1[42]. Recently, these limitations have been overcome by adding a second-harmonic field polarized orthogonally to the fundamental field [39]. By varying the time delay between the two harmonic fields the angle between ionization and recollision is controlled and resolved. This extended version of the orbital tomography allowed reconstruction of the 2p orbital for neon (see Fig. 1.3b). It is also possible to expand this method to unaligned molecules if there exists a characteristic angular distribution of the tunneling ionization probability, which can be related to a specific orbital, such as in CO_2 [43] or in C_2H_6 [44].

Wave functions might also be observed in a more direct way in a sense that already raw images, without any reconstruction procedures, reveal elements of the quantum state under examination. One of such a direct method is scanning - tunneling microscopy (STM), which have allowed the observation of eigenstates of the so-called "quantum corral", created by placing 48 Fe atoms into a ring on a Cu surface [45] (see Fig. 1.4a). STM imaging techniques rely on the nonzero conductance of its tunneling junction meaning that atoms/molecules must be positioned on metals or semiconductors. As the experiment on the quantum corral showed, the electronic structure of a single atom is strongly perturbed by the surface electrons. However, this limitation might be overcome by using insulating films of a thickness of few atomic layers, what ensures a sufficient electronic decoupling and consequently observation of the HOMO and LUMO of an individual molecule [46] (see Fig. 1.4b). Alternatively, one can use the molecular-frame photoelectron angular distribution (MFPAD) method to observe nodal planes of the HOMO and HOMO-1 in polar molecules [47]. In this technique molecules with a permanent dipole moment are three-dimensionally oriented by combined laser and electrostatic field and subsequently ionized with intense, circularly polarized laser pulses, which prevents recollision of the free electron with its parent ion. The presence of the nodal plane

in the HOMO leads to a left-right splitting of the momentum distribution along the x-axis (e.g. parallel to the detector plane), what can be directly observed in photoelectron images. Very recently it was shown that in experiments on aligned molecules, which are photoionized by extreme ultraviolet (XUV) laser light polarized perpendicularly to the internuclear axis, the recorded MFPADs directly reveal the nodal structure of molecular wave functions [48].

1.4 Scope of this thesis

Additional possibilities for imaging the nodal planes of atomic orbitals can be created by placing atoms into a DC electric field, which introduces a quantization axis and aligns the orbitals prior to being measured. When atoms are photoexcited into quasi-bound Stark states with narrowband laser pulses, projection of the launched photoelectrons on a position-sensitive detector, placed perpendicularly to the electric field direction directly reveals the nodal structure of the atomic orbitals prepared in Stark states prior to ionization. This is the principle of an imaging technique called photoionization microscopy (PM), proposed more than 30 years ago [49–51]. A hundred years after Bohr introduced the model of quantized energy levels in hydrogen atoms it was possible, for the first time, to directly measure atomic orbitals of hydrogen by means of photoionization microscopy [52], as presented in Chapter 5.

This thesis deals with experiments employing the photoionization microscopy technique and making use of the simplest atoms in nature: hydrogen and helium. It may convey the impression that the helium atom is slightly more complex than hydrogen since it only has one additional electron and its ionic core contains one extra proton and two neutrons. However, from the point of view of quantum mechanics these two atoms are fundamentally different and represent two separate groups of atoms. Namely, for hydrogenic atoms the quantum mechanical calculations can be performed exactly and with high accuracy while for nonhydrogenic atoms various approximation methods need to be used to carry out calculations to a high degree of accuracy. In Chapter 2 it is shown that for the hydrogen atom the Schrödinger equation (1.5) in parabolic coordinates has exact analytical solutions and in the presence of an external electric field it remains separable. On the contrary, the finite size of the ionic core in helium leads to the situation when the wave equation becomes nonseparable. Consequently, both atoms behave differently while exposed to an external electric field, a key element of photoionization microscopy, and ionize in a distinct manner. Chapters 5 and 6 illustrate that due to these dissimilarities the nodal structure of the electronic wave function is always observable in the experiments on hydrogen atoms (Chapter 5), whereas in the case of helium the observation is possible owing to the interference narrowing effect (Chapter 6).

This thesis is organized as follows. Chapter 2 contains a detailed theory of the Stark effect in the hydrogen atom and demonstrates distinct properties of hydrogenic and nonhydrogenic atoms exposed to external electric fields. Particularly, atomic energy levels, with a special interest on crossings between states, and field ionization

mechanisms are considered. Moreover, in the last part of Chapter 2 different theoretical approaches to the Stark problem, which are used in calculations presented in this thesis, are discussed. Chapter 3 provides a detailed description of the experiments on hydrogen and helium atoms, with the emphasis on crucial elements in the experimental setups, the efficiency of the overall processes and the data acquisition procedure. Prior to the discussion of the experimental results, a theory of photoionization microscopy, within the framework of semiclassical and quantum mechanical theory, is presented in Chapter 4. The same chapter introduces experimental results on interference effects in hydrogen, which provide a deeper insight into the interactions between the core and the photoelectron since they are reflected in various classical trajectories by which the photoelectron moves en route the detector. Moreover, the interference images reveal, for the first time, beating patterns between so-called direct and indirect photoelectron trajectories. Resonant phenomena in hydrogen are treated extensively in Chapter 5 and the presented experimental results show in a convincing way that the nodal structure of electronic wave functions is directly observable in these experiments. Finally, Chapter 6 demonstrates the importance of the interference narrowing effect in the visualization of nodes of wave functions in helium atoms and by that very fact indicates the fundamental differences between hydrogenic and nonhydrogenic atoms.

2 Stark effect

2.1 History of the discovery

In 1896 the Dutch experimental physicist Zeeman [53] discovered that a magnetic field splits spectral lines of atoms into doublets or triplets. Motivated by this discovery many attempts were made to find an analogous effect caused by an electric field. In 1901 Voigt [54] analyzed this problem within the framework of classical electrodynamics and calculated that two sodium D lines in an electric field of 300 V/cm should be split by about $3\times10^{-4}\mathring{A}$, which suggested that such an effect could not be observed experimentally. Regardless of Voigt's negative result Stark, who was one of the earliest supporters of the quantum theory, decided to experimentally study the effect of an electric field on spectral lines. By using hydrogen and a transverse electric field of the order of 10^4 V/cm he observed in 1913 a splitting of the hydrogen H_β and H_γ lines into several components [55]. Simultaneously and independently the Italian physicists Lo Surdo observed splitting of the same hydrogen lines while studying the spectra emitted by so-called "retrograde rays" [56, 57]. The advantage of Lo Surdo's experiment was that the gradient of the electric field present in a discharge tube, directly revealed the relationship between the strength of the electric field and the splitting (see Fig. 2.1a-b).

The first satisfactory theoretical interpretation of the Stark effect was already obtained in 1916 independently by Epstein [14] and Schwarzschild [15] within the framework of the Old Quantum Mechanics. To examine the influence of an external electric field on an electron they used a system of parabolic coordinates, which is defined as follows:

$$\begin{aligned} \xi &= r + z, \\ \eta &= r - z, \\ \varphi &= tan^{-1}\frac{y}{x}. \end{aligned} \tag{2.1}$$

and

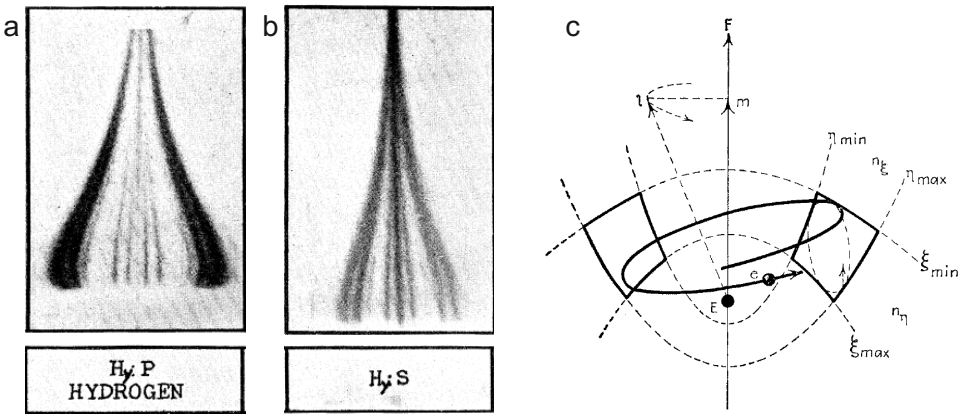

Figure 2.1: Longitudinal (a) and transverse (b) Stark effects observed for the hydrogen H_γ line in the experiment by J.S. Foster [58]. (c) A schematic representation of the electron motion (black thick curve) in parabolic coordinates according to the old quantum mechanics interpretation. Confined to this region the electron has three periodic motions, i.e. around the electric field direction given by m, along the ξ and η coordinates given by n_ξ and n_η, respectively [25]

$$
\begin{aligned}
x &= \sqrt{\xi\eta}cos\varphi, \\
y &= \sqrt{\xi\eta}sin\varphi, \\
z &= \frac{1}{2}(\xi - \eta), \\
r &= \frac{1}{2}(\xi + \eta),
\end{aligned}
\tag{2.2}
$$

and it is drawn schematically in Fig. 2.1c. The surfaces with constant ξ or η are paraboloids obtained by revolving about the electric field axis. In this coordinate system the nucleus is placed at the focus ($x = y = z = 0$). Note that atomic units are used, unless specified otherwise.

According to their interpretation the electron follows an elliptical orbit confined to the space between the parabolas (ξ_{min}, ξ_{max}) and (η_{min}, η_{max}) while the plane of the orbit processes about the azimuthal angle φ (see Fig .2.1c). The total energy of the electron is given by [59]:

$$E = E_0 + \Delta E, \tag{2.3}$$

where E_0 is the field-free energy of the electron expressed by $E_0 = 1/2n^2$ and ΔE represents the shift in the energy levels due to the presence of the external electric

field and can be expanded as a power series in the electric field strength F as:

$$\Delta E = AF + BF^2 + CF^3 + \cdots . \tag{2.4}$$

In parabolic coordinates the total principal quantum number is given by $n = n_\xi + n_\eta + n_\varphi$, where n_ξ and n_η are the so-called parabolic quantum numbers and n_φ is the azimuthal quantum number. By analogy to the azimuthal quantum number l in the Kepler problem n_φ can be expressed as $n_\varphi = m + 1$, where $m = 0,\ 1,\ 2,\ \ldots$ [59]. The linear term AF and the quadratic term BF^2 represent the first– and the second–order Stark effect, respectively, with A and B given by:

$$A = \frac{3}{2} n (n_\xi - n_\eta), \tag{2.5}$$

$$B = -\frac{1}{16} n^4 \{17n^2 - 3(n_\xi - n_\eta)^2 - 9m^2 + 19\}. \tag{2.6}$$

The quadratic Stark effect was experimentally observed in 1918 by Takamine and Kokubu [60]. One year latter Kramers [61] estimated the relative intensities of spectral lines and determined the polarizations of the hydrogen-line components, ipso facto obtaining an excellent agreement with Stark's measurements.

2.2 The Stark effect in the point of view of the Quantum Mechanics

The Old Quantum Mechanics, despite being successful in giving a quantitative explanation of the Stark effect, was actually full of ambiguities, as has been emphasized at the end of Section 1.1. Only a few months after Schrödinger's breakthrough publication Epstein approached the Stark effect problem again, this time from Schrödinger's quantum theory point of view [62]. Once more an excellent agreement between the calculated positions of lines with the experimental observation was obtained and the new expressions for the linear and quadratic Stark effect were identical with the ones attained by means of the Old Quantum Mechanics. Furthermore, within the framework of the new theory of Quantum Mechanics the restriction for the azimuthal quantum number $n_\varphi > 0$ appeared automatically. That was a clear advantage over the Bohr-Sommerfeld theory, where this restriction was artificially introduced to eliminate plane orbits in which the electron would sooner or later undergo a collision with the nucleus.

2.2.1 The Schrödinger equation in parabolic coordinates

A single positively charged proton, which constitutes a hydrogen nucleus, produces a Coulomb potential, i.e. a potential depending only on the distance r of the particle from the center of force, ensuring that the Hamiltonian operator has spherical symmetry and the wave equation (1.5) is separable in spherical coordinates, as shown in Section 1.2. While dealing with perturbation problems, where an external force distinguishes a particular direction in space (e.g. Stark effect, photoelectron effect, etc.), one can use parabolic coordinates ξ, η, and φ to separate the Schrödinger equation [63–65].

The Hamiltonian operator for the hydrogen atom is given by:

$$\widehat{H} = -\frac{\nabla^2}{2} + V(r), \tag{2.7}$$

where ∇^2 is the Laplacian operator and $V(r) = -1/r$ represents the Coulomb potential. Thus, the time independent Schrödinger equation in parabolic coordinates may be written as:

$$\left[-\frac{\nabla^2}{2} - \frac{2}{\xi + \eta} \right] \psi = E\psi, \tag{2.8}$$

with the Laplacian operator in parabolic coordinates expressed by:

$$\nabla^2 = \frac{4}{\xi + \eta} \frac{\partial}{\partial \xi} \left(\xi \frac{\partial}{\partial \xi} \right) + \frac{4}{\xi + \eta} \frac{\partial}{\partial \eta} \left(\eta \frac{\partial}{\partial \eta} \right) + \frac{1}{\xi \eta} \frac{\partial^2}{\partial \varphi^2}. \tag{2.9}$$

To find solutions of the wave equation (2.8) one can assume that the wave function is of the form:

$$\psi(\xi, \eta, \varphi) = u_1(\xi) u_2(\eta) e^{im\varphi}, \tag{2.10}$$

where m is the magnetic quantum number. Substituting Eq. (2.9) and (2.10) into Eq. (2.8) and separating it with constants Z_1 and Z_2 related by $Z_1 + Z_2 = 1$, one obtains two independent equations for functions $u_1(\xi)$ and $u_2(\eta)$:

$$\frac{d}{d\xi} \left(\xi \frac{du_1}{d\xi} \right) + \left(\frac{1}{2} E\xi + Z_1 - \frac{m^2}{4\xi} \right) u_1 = 0, \tag{2.11a}$$

$$\frac{d}{d\eta} \left(\eta \frac{du_2}{d\eta} \right) + \left(\frac{1}{2} E\eta + Z_2 - \frac{m^2}{4\eta} \right) u_2 = 0. \tag{2.11b}$$

The solutions of these equations can be found by assuming that $u_1(\xi)$ behaves as $exp(-\frac{1}{2}\varepsilon\xi)$ for large ξ, where $\varepsilon = \sqrt{-2E}$, and as $\xi^{\frac{1}{2}|m|}$ for small ξ. Accordingly, the same assumptions should be made for $u_2(\eta)$. As a result the normalized eigenfunction for the hydrogen atom is given in terms of associated Laguerre polynomials [63]:

$$\psi_{nn_1n_2m} = \frac{e^{im\varphi}}{\sqrt{\pi n}} \cdot \frac{n_1!^{\frac{1}{2}} n_2!^{\frac{1}{2}} \varepsilon^{|m|+\frac{3}{2}}}{(n_1+|m|)!^{\frac{3}{2}}(n_2+|m|)!^{\frac{3}{2}}} \cdot \\ \cdot e^{-\frac{1}{2}\varepsilon(\xi+\eta)}(\xi\eta)^{\frac{1}{2}|m|} L^{|m|}_{n_1+|m|}(\varepsilon\xi) L^{|m|}_{n_2+|m|}(\varepsilon\eta), \quad (2.12)$$

where, n is the principal quantum number, n_1 and n_2 are nonnegative integers called parabolic quantum numbers. Additionally, n_1 and n_2 are the numbers of nodes in the $u_1(\xi)$ and $u_2(\eta)$ wave functions and relate to n via:

$$n = n_1 + n_2 + |m| + 1, \quad (2.13)$$

and

$$n_1 = \frac{Z_1}{\varepsilon} - \frac{1}{2}(|m|+1), \quad (2.14a)$$

$$n_2 = \frac{Z_2}{\varepsilon} - \frac{1}{2}(|m|+1). \quad (2.14b)$$

By solving equations (2.14a) or (2.14b) for ε one obtains the energy for the hydrogen atom:

$$E = -\frac{1}{2n^2}. \quad (2.15)$$

The above expression is identical with the one obtained by means of the old quantum mechanics, as shown in Section 2.1.

The electron probability distribution in parabolic coordinates can be calculated by taking the squared absolute value of Eq. (2.12). Fig. 2.2 shows eigenstates calculated for $n = 6$ and $m = 0$, which are described by a set of quantum numbers $(n,\ n_1,\ n_2,\ m)$. Closer examination reveals that the nodes lie on parabolas and one can observe a visible asymmetry with respect to the plane $z = 0$. For $n_1 > n_2$ the charge distribution of the electron is localized along the $+z$ axis whereas for $n_1 < n_2$ it is localized on the negative side of z. Therefore, the displacement of the center of mass of the charge distribution results in a permanent electric dipole moment, which is conspicuous for all states.

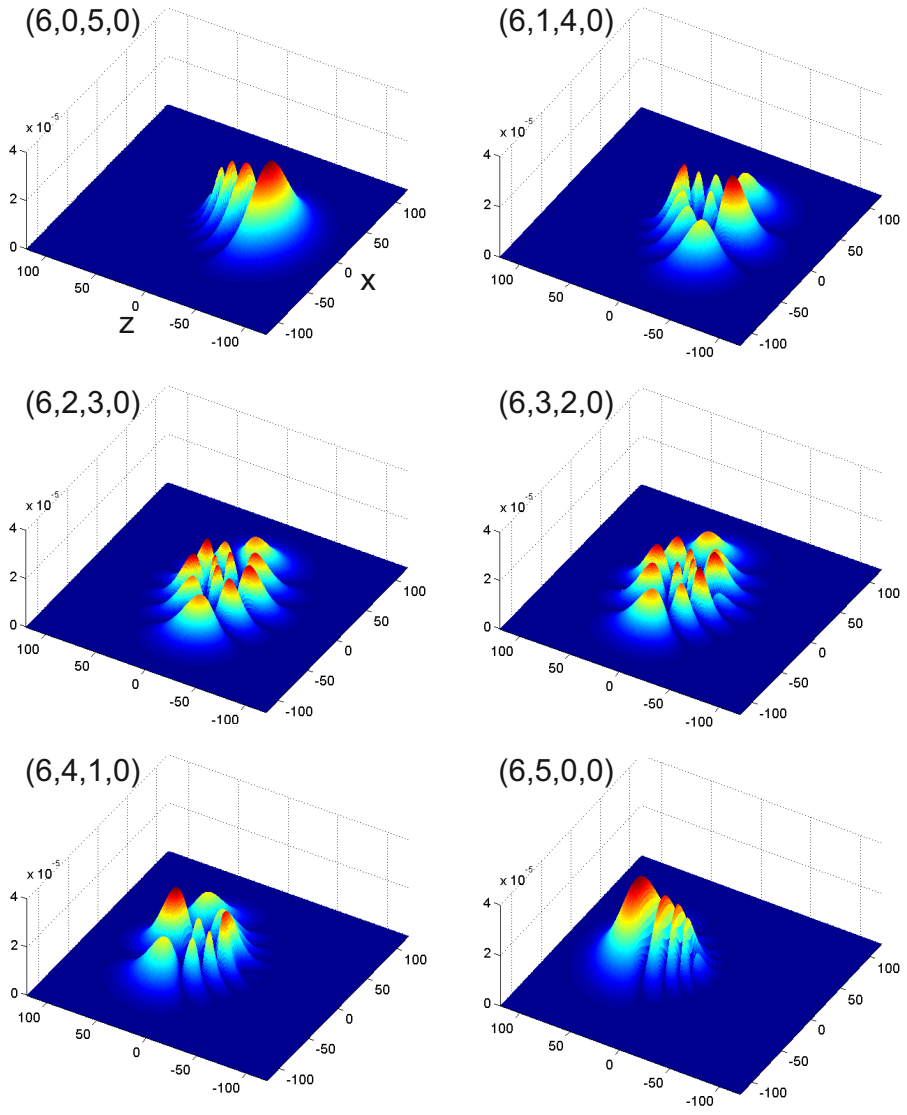

Figure 2.2: Charge distribution of the electron for parabolic eigenstates: $(n,\ n_1,\ n_2,\ m)$ *=(6, 0, 5, 0), (6, 1, 4, 0), (6, 2, 3, 0), (6, 3, 2, 0), (6, 4, 1, 0), and (6, 5, 0, 0). The dipole moments, which give rise to the first order Stark effect, are conspicuous. Note that the nucleus is at the center of the coordinate system.*

The hydrogenic parabolic nn_1n_2m states and the spherical nlm states can be related to each other via a unitary transformation [66]:

$$\psi_{nn_1n_2m} = \sum_{l=|m|}^{n-1} \left(\frac{n-1}{2}, \frac{n-1}{2}, \frac{m+n_1-n_2}{2}, \frac{m-n_1+n_2}{2} \middle| \frac{n-1}{2}, \frac{n-1}{2}, l, m \right) \psi_{nlm} \tag{2.16}$$

where $(\ldots|\ldots)$ is the Clebsh-Gordan coefficient. For example, the $(n,\ n_1,\ n_2,\ m)$ $= (6,\ 0,\ 5,\ 0)$ parabolic state shown in the top-left corner of the Fig .2.2 is a linear combination of spherical states with weights given by the Clebsh-Gordan coefficients, i.e.:

$$\psi_{6050} = -\frac{1}{\sqrt{6}}\psi_{600} + \sqrt{\frac{5}{14}}\psi_{610} - \frac{5}{2\sqrt{21}}\psi_{620} + \frac{\sqrt{5}}{6}\psi_{630} - \frac{1}{2\sqrt{7}}\psi_{640} + \frac{1}{6\sqrt{7}}\psi_{650}. \tag{2.17}$$

2.2.2 Linear and quadratic Stark effect by means of perturbation theory

A homogenous electric field of strength F in the z direction introduces a perturbation potential that can be expressed in parabolic coordinates as:

$$Fz = \frac{1}{2}F(\xi - \eta). \tag{2.18}$$

Consequently the Schrödinger equation for the hydrogen atom in a uniform electric field is given by [63–65]:

$$\left[-\frac{\nabla^2}{2} - \frac{2}{\xi+\eta} + \frac{F(\xi-\eta)}{2} \right] \psi = E\psi. \tag{2.19}$$

The above equation can again be separated by introducing three functions, each along one parabolic coordinate, as in Eq. (2.10). The one-dimensional equations for ξ and η are in analogy to equations (2.11a) and (2.11b):

$$\frac{d}{d\xi}\left(\xi\frac{du_1}{d\xi}\right) + \left(\frac{1}{2}E\xi + Z_1 - \frac{m^2}{4\xi} - \frac{1}{4}F\xi^2\right)u_1 = 0 \tag{2.20a}$$

$$\frac{d}{d\eta}\left(\eta\frac{du_2}{d\eta}\right) + \left(\frac{1}{2}E\eta + Z_2 - \frac{m^2}{4\eta} + \frac{1}{4}F\eta^2\right)u_2 = 0 \tag{2.20b}$$

with the so-called "effective" charges subject to the condition $Z_1 + Z_2 = 1$. The above differential equations are too complex to be solved exactly. The simplest way

to calculate approximate energy levels for the hydrogen atom in an electric field is to use perturbation theory. Namely, first solve the zero field problem and then calculate the electric field effect by means of a perturbation series.

In the absence of the electric field the effective charge $Z_1^{(0)}$ is given by Eq. (2.14a). The first order correction of this quantity is calculated as the integral of the perturbation potential evaluated over the unperturbed eigenfuction $u_1(\xi)$ given by Eq. (2.12) [63]:

$$Z_1^{(1)} = \frac{1}{4}F\int_0^\infty \xi^2 u_1^2(\xi)d\xi = \frac{1}{4}F\varepsilon^{-2}(6n_1^2+6n_1|m|+m^2+6n_1+3|m|+2). \quad (2.21)$$

Altogether the effective charge Z_1 is given by:

$$Z_1 = Z_1^{(0)}+Z_1^{(1)} = \varepsilon\left(n_1+\frac{|m|+1}{2}\right)+\frac{1}{4}F\varepsilon^{-2}(6n_1^2+6n_1|m|+m^2+6n_1+3|m|+2). \quad (2.22)$$

The expression for Z_2 is obtained by replacing n_1 with n_2. By substituting the expressions of the effective charges in the relation $Z_1 + Z_2 = 1$ and solving it with respect to ε one obtains the energy of hydrogen levels to the first approximation:

$$E = -\frac{1}{2}\varepsilon^2 = -\frac{1}{2n^2}+\frac{3}{2}Fn(n_1-n_2). \quad (2.23)$$

The second term on the right side is the linear Stark effect, which is identical with the expression calculated by Schwarzschild and Epstein given by Eq. (2.5). The first order Stark effect results in a symmetrical splitting of the energy levels about their field-free positions. The energetically highest Stark component corresponds to $n_1 = n - 1$, $n_2 = 0$ and refers to the situation when the electron is predominately located on the positive side of the z-axis, i.e. located uphill with respect to the Coulomb potential (e.g. the (6, 5, 0, 0) state shown in Fig. 2.2). This state is a so-called blue state as the transition energy is shifted towards shorter wavelengths while compared to the field-free case. By analogy the lowest Stark level, a so called red state, corresponds to $n_1 = 0$, $n_2 = n - 1$ and has the electron located downhill with respect to the Coulomb potential, i.e. on the negative side of the z-axis as shown for the (6, 0, 5, 0) state in Fig. 2.2. The energy separation between the two extreme components of a Stark manifold is given by:

$$\Delta E = 3Fn(n-1). \quad (2.24)$$

To obtain the energy expression including the quadratic Stark effect one needs to calculate the second order perturbations for Z_1 and Z_2 using the general formulae of perturbation theory [64]:

$$Z_1^{(2)} = \frac{F^2}{16} \sum_{n_1' \neq n_1} \frac{|(\xi^2)_{n_1 n_1'}|^2}{Z_1^{(0)}(n_1) - Z_1^{(0)}(n_1')}$$
$$= -\frac{1}{16} F^2 \varepsilon^{-5} (|m| + 2n_1 + 1)[4m^2 + 17(2|m|n_1 + 2n_1^2 + |m| + 2n_1) + 18]. \tag{2.25}$$

As a result, the energy is given to second order by:

$$E = -\frac{1}{2}\varepsilon^2 = -\frac{1}{2n^2} + \frac{3}{2} F n(n_1 - n_2) - \frac{1}{16} F^2 n^4 [17n^2 - 3(n_1 - n_2)^2 - 9m^2 + 19]. \tag{2.26}$$

The third term on the right side is the quadratic Stark effect and is identical with the Old Quantum Mechanical expression in Eq. (2.6). In contrast to the linear Stark effect it depends also on the magnetic quantum number m. By having a closer look at Eq. (2.26) one can realize that the quadratic Stark effect always results in a lowering of the levels.

2.3 Energy levels in a presence of electric fields – Stark maps

2.3.1 Hydrogen atom

The uniqueness of the hydrogen atom comes from the fact that it has only one electron moving in the Coulomb central potential and consequently its energy depends only on the principal quantum number n, as shown in Eq. (2.15). This implies that in the absence of external perturbations energy levels are degenerate with respect to the azimuthal and magnetic quantum numbers l and m. When the hydrogen atom is placed in an external electric field the degeneracy of the lm states of a particular n is lifted. Nevertheless, states that differ only in the sign of the magnetic quantum number remain degenerate. Thus the energy level specified by the principal quantum number n is split into $n(n+1)/2$ sublevels, which can be characterized by parabolic quantum numbers n_1,n_2 and m.

A peculiar consequence of the symmetrical Coulomb potential is that the hydrogen atom has a permanent electric dipole moment, except for the ground state ($n = 1$), which is clearly visible in Fig. 2.2. Therefore, while being placed in an external electric field hydrogen exhibits a linear Stark effect. The second-order Stark effect is always present as the electric dipole moment is modified by the electric field. Fig. 2.3a shows a Stark map calculated for the hydrogen atom in the vicinity of the $n = 15$ manifold. This figure points out that the linear Stark effect is the dominant feature, whereas curvature of the levels due to the second– and higher– order effects is hardly visible for the given energy and field range. However, the quadratic Stark effect becomes conspicuous for higher electric fields and higher states.

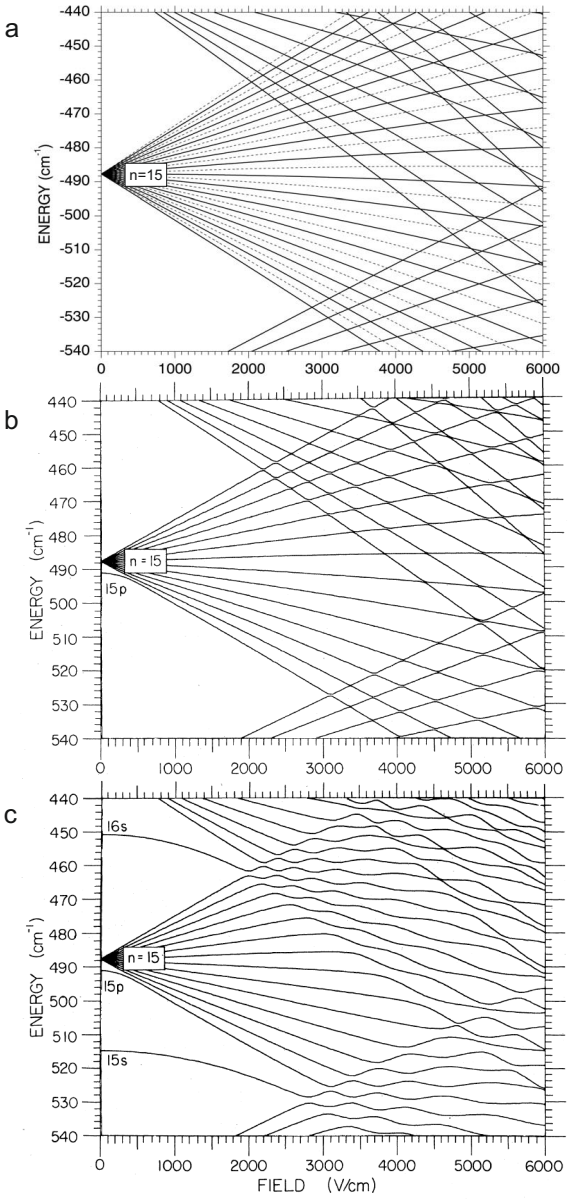

Figure 2.3: Calculated Stark maps for (a) hydrogen atom m = 0 states (solid lines) and m = 1 (dashed lines) states in the vicinity of the n = 15 manifold, obtained by means of seventeenth order perturbation theory [67]. Stark structures of the lithium atom for (b) m = 1 and (c) m = 0 states (reproduced from Ref. [68]).

Another peculiarity observed in the hydrogen Stark map is that states of different principal quantum number n actually cross, in spite of the fact that they have the same m [69]. However, relativistic effects can produce small coupling between these states, that otherwise would cross, leading to occurrence of so-called anticrossings [70]. Nevertheless, this effect is beyond the experimental resolution of experiments presented in this thesis and therefore will not be further discussed. In hydrogen the even and the odd m levels are interleaved, as can be seen in Fig. 2.3a by comparing the positions of energy levels for $m = 0$ (solid lines) and for $m = 1$ (dashed lines).

2.3.2 Nonhydrogenic atoms

Atoms other than hydrogen have a complex nucleus, comprising protons and neutrons, and more than one electron, resulting in a finite size of the ionic core. Consequently, the core potential experienced by a valence electron is no longer purely Coulombic, hence the Hamiltonian is no longer separable and there is no analytical solution to the wave equation (Eq. (1.5)). To calculate the wave function of a "one-electron" atom, i.e. an atom with one electron excited into a state with high principal quantum number n, one can use the methods of Quantum Defect theory (QD) [[71] and references therein]. In QD the energy of atoms is given by:

$$E = \frac{Z^2}{2(n - \delta_l)^2}, \tag{2.27}$$

where δ_l is an empirically observed quantum defect for a series with orbital angular momentum l and provides a measure of the difference between the ionic core potential and the pure Coulomb potential. In Rydberg atoms, a highly excited electron spends most of its time at large distance ($r \sim n^2$), where its wave function can be accurately represented by Coulomb functions. However, there is a significant difference between states with high and low orbital angular momentum, as an electron in a high l state never comes close to the ionic core, preventing mutual interaction – its quantum defect is small and the atom behaves hydrogenically. By contrast, a Rydberg electron in a low l state comes close to the core and it can both polarize and penetrate it. This leads to significant changes of the wave function and of the atomic energy level with respect to its hydrogenic counterpart – for such states quantum defects are large.

In zero electric field the non-Coulombic potential acting upon the electron already removes the n^2 degeneracy of the n shell and thus the energy levels, especially for states with low l, are depressed. Since the energy levels are not degenerate with respect to the orbital quantum number l, in the presence of an electric field the first order perturbation to the energy vanishes. Therefore, nonhydrogenic atoms exhibit a quadratic Stark effect for low values of the electric field and when the Stark interaction becomes comparable to the core interactions responsible for the quantum defect, the Stark shift becomes linear – similar to the hydrogen case.

Fig. 2.3 shows calculated Stark maps for lithium in (b) $m = 1$ and (c) $m = 0$ states, which at low field strength are quasidegenerate and therefore not interleaved

like hydrogen [72]. When the quantum defect is small, as for $l = 1$ states ($\delta_p \approx 0.05$ [68]), the system shows largely hydrogenic behavior, similar to the H Stark map shown in Fig. 2.3a. The only noticeable deviation is near zero field, where the $15p$ state is significantly depressed, experiencing initially a quadratic Stark effect in contrast to the linear behavior of the remaining levels. For large quantum defects, like in the case of $l = 0$ states ($\delta_s \approx 0.4$ [68]) that contribute to the Stark maps calculated for $m = 0$, the structure differs dramatically from the hydrogenic one. A conspicuous result is that the $15s$ and $16s$ levels never display a linear Stark effect and are repelled by levels above and below them. When they are squeezed between the adjacent manifolds the entire Stark structure is altered and the resemblance to the hydrogenic structure is lost, in contrast to the $m = 1$ case.

Another consequence of the non-Coulombic potential is that red and blue states are coupled by their slight overlap at the core what results in avoided crossings. A break of a dynamical symmetry of the Coulomb potential leads to a situation when states with the same m cannot cross. The first anticrossing between red and blue states of adjacent n manifolds occurs for fields:

$$F > \frac{1}{3(n-\delta_l)^5}. \tag{2.28}$$

Most of the avoided crossings are too small to be observed in Fig. 2.3b, although this effect has its significance as will be explained in the next section. The $m = 0$ states exhibit larger anticrossings. The maximum possible repulsion between levels is half of the energy separation, thus $\sim 1/(n-\delta_l)^3$. Therefore, larger quantum defects produce larger repulsions between levels, but the repulsion can suddenly diminish creating an unexpected pseudocrossing as shown in Fig. 2.3c at F = 4.8 kV/cm and E = 507 cm^{-1}. In this particular case, this is caused by the fact that the interacting levels from the $n = 16$ and $n = 14$ manifolds have the largest and the smallest quantum detects, respectively.

2.4 Field ionization

2.4.1 Hydrogen atom

When a hydrogen atom is placed in an electric field it experiences the combined Coulomb-Stark potential $V(r) = -\frac{1}{r} + Fz$. This potential lowers the ionization threshold (from $E = 0$, which is the field-free ionization limit) to a saddle point on the z–axis where the potential energy has the value $E_{sp} = -2\sqrt{F}$ (see Fig. 2.4a). If one ignores all quantum effects and the Stark shift of energy levels, an electron bound by energy E can be ionized by a field with strength:

$$F = \frac{1}{16n^4}. \tag{2.29}$$

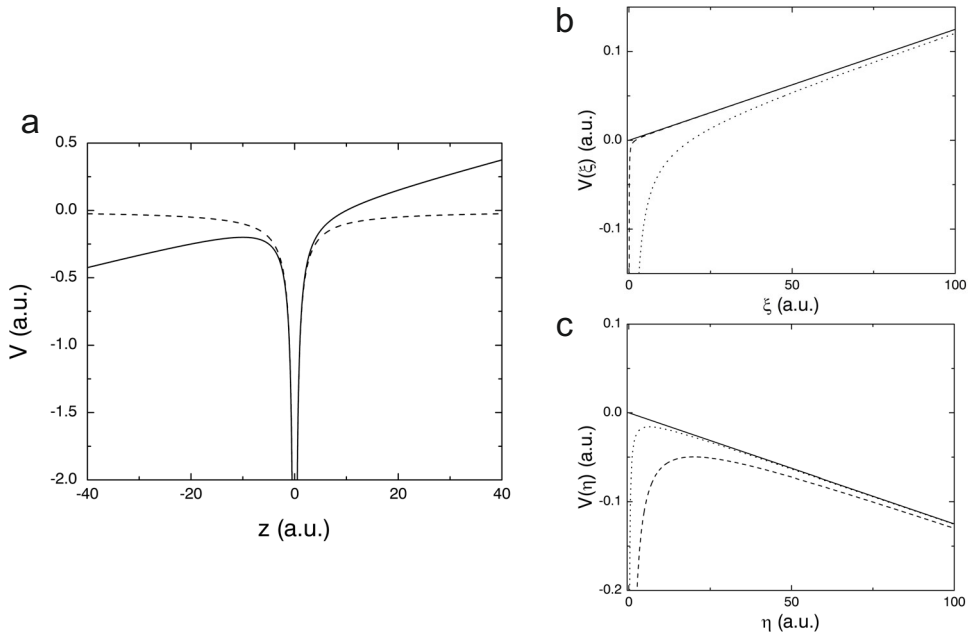

Figure 2.4: (a) Comparison between a pure Coulombic potential (dashed lines) and the combined Coulomb-Stark potential (solid lines) along the z–axis for a field of $F = 0.01$ (a.u.) in the z direction. Plots of the potentials (b) $V(\xi)$ and (c) $V(\eta)$ for a red state with $Z_2 = 0.99$ (dashed lines) and a blue state with $Z_2 = 0.10$ (dotted lines) in an electric field of $F = 0.01$ (a.u.) for $m = 1$. The solid line is a pure Stark potential with values (b)$+\frac{1}{4}F\xi$ and (c) $-\frac{1}{4}F\eta$.

However, in 1930 Gebauer and Rausch van Traubenberg [73], while studying the ionization thresholds of Stark states, observed that red states, which are located at lower energies are less stable with respect to ionization compared to blue states. This counter-intuitive phenomenon was explained by Lanczos [74] owing to later developments in quantum mechanics.

To qualitatively explain the field ionization process for the hydrogen atom one can replace functions $u_1(\xi)$ and $u_2(\eta)$ in Eqs. (2.20a) and (2.20b) with [64]:

$$u_1(\xi) = \frac{\chi_1(\xi)}{\sqrt{\xi}}, \tag{2.30a}$$

$$u_1(\eta) = \frac{\chi_2(\eta)}{\sqrt{\eta}}. \tag{2.30b}$$

By introducing a normalization factor of $\sqrt{2\pi}$ the wave function is given by:

$$\psi(\xi, \eta, \varphi) = \frac{1}{\sqrt{2\pi\xi\eta}}\chi_1(\xi)\chi_2(\eta)e^{im\varphi}. \tag{2.31}$$

Functions $\chi_1(\xi)$ and $\chi_2(\eta)$ describe the electron motion along the ξ and η coordinates, respectively. For each coordinate there exists a certain effective potential acting on the electron, which is given by:

$$V(\xi) = -\frac{Z_1}{2\xi} + \frac{m^2-1}{8\xi^2} + \frac{F\xi}{8}, \tag{2.32a}$$

$$V(\eta) = -\frac{Z_2}{2\eta} + \frac{m^2-1}{8\eta^2} - \frac{F\eta}{8}. \tag{2.32b}$$

Both effective potentials are plotted in Fig. 2.4 for a red ($Z_2 = 0.99$) and a blue ($Z_2 = 0.10$) state in the Stark manifold. The different shape of the $V(\xi)$ and $V(\eta)$ potentials leads to qualitatively different wave functions. For vanishing electric fields and $E < 0$ both $\chi_1(\xi)$ and $\chi_2(\eta)$ have a discrete eigenvalue spectrum shape characterized by a set of quantum numbers $(n,\ n_1,\ n_2,\ m)$. When the electric field does not vanish the spectrum of the ξ equation remains discrete, while the spectrum of the η equation becomes continuous. Closer examination of Eq. (2.32a) and Fig. 2.4b shows that the motion in the ξ direction is always bound since $V(\xi) \to F\xi$ as $\xi \to \infty$. Therefore, the $\chi_1(\xi)$ function has a well-defined number of nodes which is equal to the parabolic quantum number n_1. Thus, for ionization to occur the electron must escape to $n = \infty$. For states with energy bigger than the peak in the potential $V(\eta)$ the entire region is classically accessible for $n > 0$ and ionization occurs for fields:

$$F > \frac{E^2}{4Z_2}. \tag{2.33}$$

The effective charge Z_2 for a blue state $n_1 - n_2 \approx n$ has a value $Z_2 \approx 1/n$ and for the red state $Z_2 \approx 1$, thus if blue and red states have the same energy the red one will be the most ionized (see Fig. 2.4c). It has been shown [75] that for $m = 0$ states belonging to the same Stark manifold the ionization threshold electric field for the bluest state is by a factor of three larger than the threshold electric field of the reddest state.

If the energy is less than the peak of the $V(\eta)$ potential, the electron can tunnel through the barrier. For energies far below the top of the potential the transmission through the barrier is vanishingly small and the resonances are so sharp as to be bound states. With increase of the energy the transmission through the barrier increases, hence the width of resonances increases and the amplitude of $\chi_2(\eta)$ in the inner well decreases. Nevertheless, at resonance, when n_2 is a good quantum number fitting the number of nodes of the $\chi_2(\eta)$ wave function, the amplitude of the $\chi_2(\eta)$ function in the inner potential well of $V(\eta)$ becomes much larger than for any energy away from a resonance and below the peak of the potential $V(\eta)$. Finally, for energies above the barrier, the wave function has an amplitude which hardly depends on the energy and smoothly varies.

In a moderate electric field each energy level of the hydrogen atom ionizes at some uniform rate Γ, which is a rapidly increasing function of the field. In this regime each

state undergoes a simple exponential decay with a lifetime $\tau = 1/\Gamma$. For energies below the top of the $V(\eta)$ potential barrier a tunneling process occurs and accurate calculations of ionization rates have been made [64, 76–78]. Numerical solutions of the Stark problem for the hydrogen atom are very efficient, but for many practical purposes it is more convenient to have analytical formulae. Damburg and Kolosov obtained a formula for the level width Γ, associated with the tunneling effect, by employing an asymptotic method, which gives reliable results for a wide range of electric fields for an arbitrary n [79, 80]:

$$\Gamma = \frac{(4R)^{2n_2+|m|+1}}{n^3 n_2!(n_2+|m|)!} exp\left[-\frac{2}{3}R - \frac{1}{4}n^3 F\left(34n_2^2+34n_2|m|+46n_2+7m^2+23|m|+\frac{53}{3}\right)\right], \tag{2.34}$$

where $R = (-2E)^{3/2}/F$ and E is the Stark energy. The validity of this asymptotic formula has been experimentally confirmed by Koch and Mariani, who made the first precise measurement of absolute ionization rates for individual sublevels of hydrogen [75]. With an increase of the field strength Stark states start to broaden and create a "sea" of continuous Stark levels superimposed on other higher-lying discrete states. As the energy levels do not mix for hydrogen, the degenerate "sea" of levels has no effect on the dynamics of the hydrogen ionization process. Indeed, photoionization spectra obtained by Rottke and Welge [81] showed sharp line structures of quasistable field-ionizing states superimposed on continua for energies below the field-free ionization limit $E = 0$ and above the classical saddle point energy E_{sp}.

2.4.2 Nonhydrogenic atoms

As has been pointed out in Section 2.3.2 the finite size of the ionic core significantly alters Stark maps for nonhydrogenic atoms. Additionally it influences the process by which multi-electron atoms ionize in the presence of a static electric field. Actually there are two different forms of field ionization observed for nonhydrogenic atoms for energies below the top of the $V(\eta)$ potential. The first type of field ionization is a pure tunneling effect occurring exactly the same way as in the hydrogen atom – a state with an approximate quantum number n_1 ionizes itself and keeps the same value of n_1 if its energy is enough to penetrate the potential barrier in $V(\eta)$. Ionization rates for this form of field ionization increase rapidly in the vicinity of the classical ionization threshold meaning that states broaden until they disappear to form a continuum at the top of the $V(\eta)$ potential. The second type of field ionization is due to coupling of slowly ionizing states to rapidly ionizing states and is similar to the autoionization process in multi-electron atoms or to predissociation in molecules [84]. A simple classical picture explaining this process comprises an electron in a blue orbit, which once per revolution comes close the core and has a non-zero probability of being scattered from the stable blue orbit into the degenerate red continuum. Thus this process takes place for all nonhydrogenic Stark states except the reddest state with $n_1 = 0$, which ionizes like hydrogen at the classical

ionization limit given by Eq. (2.33) [83]. The ionization rate for the autoionization process is not exponentially dependent on the field, as for the hydrogenic ionization process, but is rather a highly nonmonotonic function of the field strength [83, 85]. As a consequence, levels retain their character for a considerable range of fields. Due to the coupling between states, there are no stable states (i.e. long-lived blue states) above the classical ionization limit and they decay more rapidly by ionization than by radiative decay, as shown experimentally by Littman [84].

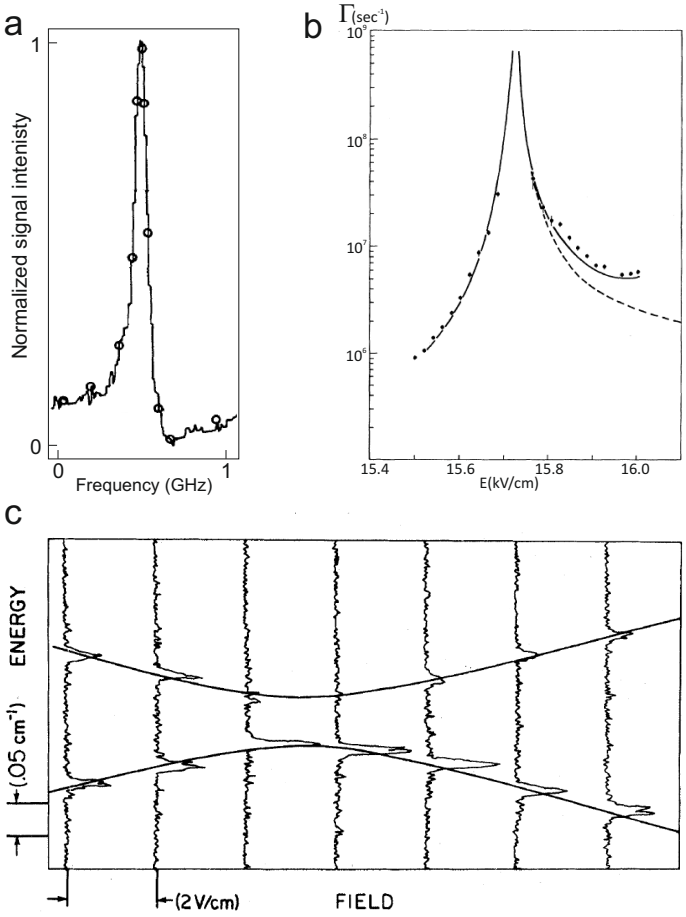

Figure 2.5: (a) Example of a characteristically asymmetric line shape observed in the photoionization spectrum of Rb in a F = 158 V/cm static electric field for an excitation energy located between the 40p and 41p levels. Dots represent the best fit to a Fano profile [82]. (b) Ionization rates for the (n, n_1, n_2, m) = (12, 6, 3, 2) state of Na in the vicinity of an avoided crossing with the rapidly ionizing (14, 0, 11, 2) state [83]. (c) Photoionization spectra of lithium measured in the region of an avoided crossing between the (18, 16, 0, 1) and (19, 1, 16, 1) states [68].

The coupling between the blue states and the red continua leads to interferences in the excitation amplitudes and gives rise to asymmetric line shapes resembling Fano profiles, which are commonly observed in the excitation spectra of autionizating states [86]. The transition strength to the mixed discrete-continuum eigenfunction exhibits constructive interference on one side of the peak and destructive interference on the other side leading to the asymmetric profile. Broadening and asymmetry introduced by core effects are greatest for $m = 0$ resonances as they penetrate the core the most. The first observation of Fano profiles in the photoionization spectrum of rubidium by Feneuille [82] (see Fig. 2.5a) confirmed that the field ionization of nonhydrogenic atoms can have the form of an autoionization process.

Field ionization process in the vicinity of an avoided-crossing

In multi-electron atoms the non-Coulombic core potential acting on the outer electron mixes states with the same m value but different n_1 or n_2 quantum numbers, causing anticrossings between levels. In the vicinity of an avoided crossing the state follows an adiabatic path when the field increases slowly meaning that none of the levels crosses. If the field increases rapidly, an atom traverses the avoided crossing diabatically – it "jumps" across the anticrossing. Zimmerman *et al.* [68] investigated the level anticrossing in lithium for interacting $(n,\ n_1,\ n_2,\ m)$= (18, 16, 0, 1) and (19, 1, 16, 1) states (see Fig. 2.5c). They observed a disappearance of the oscillator strength in the upper level and an increase in the intensity of the other level. The eigenstates at the anticrossing are symmetric and asymmetric combination of the interacting states A and B, i.e. $(1/\sqrt{2})(\psi_A \pm \psi_B)$. Thus when two Stark states have approximately equal oscillator strengths away from the crossing, the oscillator strength will vanish in one of the eigenstates and double in the other one at the avoided crossing.

Not only the oscillator strengths are altered in the vicinity of an anticrossing, but also the ionization rates are strongly perturbed. In 1976 Littman [83] observed for sodium atoms a strong increase of the ionization rate for the (12, 6, 3, 2) state while mixing with the rapidly ionizing (14, 0, 11, 2) state (see Fig. 2.5b). They found good agreement with a simple model based on a two-level system stating that at the avoided crossing the eigenstates are linear combinations of the two Stark states.

In reality the situation is more complicated as there is a simultaneous interaction between the crossing levels and the continua to which there are coupled. Therefore, near the avoided crossing the ionization rate may be estimated from the properly weighted sum of the couplings between the components of the mixture and each of the accessible continuum states [87]. If one considers unperturbed discrete states $|\phi_i\rangle$ coupled by the core interaction (V_c) to continua $|\psi_{jE}\rangle$ indicated by matrix elements V_i^{jE} then each state has a core-induced ionization rate given by:

$$\Gamma_i = 2\pi \sum_j |\langle \phi_i | V_c | \psi_{jE} \rangle|^2 = 2\pi \sum_j |V_i^{jE}|^2. \tag{2.35}$$

These states are also mixed with each other by the core interaction and near a

crossing of two states A and B the normalized eigenstates are given by:

$$|\phi_+\rangle = cos\theta\,|\phi_A\rangle + sin\theta\,|\phi_B\rangle\,, \tag{2.36a}$$
$$|\phi_-\rangle = -sin\theta\,|\phi_A\rangle + cos\theta\,|\phi_B\rangle\,. \tag{2.36b}$$

The angle θ has values from 0 to 2π, with $\theta = \pi/4$ at the center of the avoided crossing. Finally, the ionization rate of the mixed states are given by:

$$\Gamma_\pm = 2\pi \sum_j |\,\langle\phi_\pm|\,V_c\,|\psi_{jE}\rangle\,|^2 = \frac{\Gamma_A + \Gamma_B}{2} \pm \left[\frac{\Gamma_A - \Gamma_B}{2} cos2\theta + \sqrt{\Gamma_A\Gamma_B}cos\gamma\cdot sin2\theta\right], \tag{2.37}$$

where γ is an angle representing the decay-channel overlap and it is defined by:

$$cos\gamma = \frac{\sum\limits_j V_A^{jE} V_B^{jE}}{\sqrt{\sum\limits_j (V_A^{jE})^2}\sqrt{\sum\limits_j (V_B^{jE})^2}}. \tag{2.38}$$

It is interesting to calculate the minimum width of the mixed states if $\Gamma_A \neq \Gamma_B$:

$$\Gamma_{min} = \frac{\Gamma_A + \Gamma_B}{2} - \sqrt{\left(\frac{\Gamma_A + \Gamma_B}{2}\right)^2 - \Gamma_A\Gamma_B sin^2\gamma}. \tag{2.39}$$

For $\gamma = 0$ a maximum overlap between the decay channels is achieved, hence, there is only one continuum and consequently one of the mixed states is completely decoupled from the continuum leading to a decrease of its ionization rate and corresponding spectral width. Stated in other words: there are circumstances when terms in Eq. (2.37) have opposite signs and will interfere, leading to a reduction of the ionization rate. In some cases the core-induced width is canceled to such a degree that the dominant decay mechanism is ionization via hydrogenic tunneling. However, the tunneling rate exceeds the core-induced ionization rate only in a very limited field-energy region, when the resonance is located very near the top of the $V(\eta)$ potential barrier.

Such a line-narrowing or interference narrowing effect has been first observed by Feneuille [88] for rubidium atoms in a narrow energy and field range (ΔE = 0.03 cm^{-1} and ΔV = 2 V/cm), for the ionization of the (23, 0, 21, 0) state in the electric field of 2150 V/cm. The authors interpreted the observed decrease in the ionization rate as a strong perturbation introduced by the spin-orbit interaction, which coupled states with different values of m. The incorrectness of this interpretation had been pointed out by Liu [87], who observed the same effect for sodium atoms in the vicinity of an avoided crossing between two energy levels: (20, 19, 0, 0) and (21, 17, 3, 0).

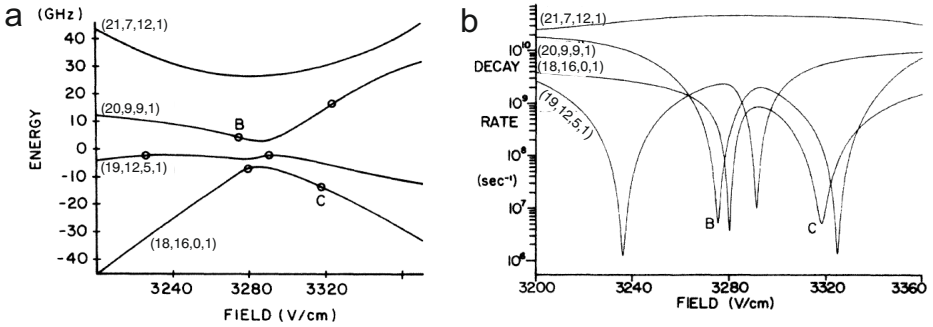

Figure 2.6: (a) Sodium Stark map in the vicinity of a four-level crossing with minima in the ionization rate indicated by circles. (b) Calculated decay rates of the four states plotted in (a) showing six regions of line-narrowing [92].

As confirmed by calculations based on the Wentzel-Kramers-Brillouin – Quantum Defect theory (WKB-QD) [89–91], the observed phenomenon was due to interference between discrete and continuum coupling amplitudes of both states. Consequently, the (20, 19, 0, 0) state was partially decoupled from the continua resulting in a decrease of its ionization width by two orders of magnitude. Further study by McNicholl [92] brought more details about the interference-narrowed Stark resonances in sodium. Fig. 2.6 shows the examined case of a four-level crossing indicating six regions of line-narrowing, the number of distinct pairs of levels, each positioned slightly outside the center of the anticrossing. For each line-narrowing region the calculated ionization rates show a decrease by circa three orders of magnitude. In the vicinity of another avoided crossing the authors observed a reversal of the asymmetry of the Fano profile caused by the sign change of transition amplitude. It has been pointed out by Yang [93] that there are much more interference-narrowing regions to be found in sodium than in rubidium. In the former case the ion-core potential is smaller, hence, Stark levels preserve the hydrogenic structure to a much greater degree and there are many regions where 2, 3 or 4 hydrogenic levels cross. Thus, it is a bit ironic that the effect was first observed for rubidium atoms. The line-narrowing phenomenon has also been observed for helium [94], lithium [95] and barium [96].

2.5 Theoretical calculations of the Stark problem

As has been pointed out in Section 2.2.2 differential equations (2.20a) and (2.20b) cannot be exactly solved with the help of elementary functions. However, different theoretical approaches allow the calculation of the approximate energies of Stark states by means of: perturbation theory [97], the Wentzel - Kramers - Brillouin (WKB) approximation [76, 78], WKB - Quantum Defect theory (WKB-QD) [89–91, 98] or numerical methods [99–101]. All these procedures are suitable for distinct field intensities, energies, state characters (red or blue) and types of atoms under

investigation. In this thesis three different methods are employed for calculations of the Stark effect in hydrogen and helium and only these approaches will be elaborated in more detail below.

2.5.1 Perturbation theory

The first quantum-mechanical problem treated by Rayleigh-Schrödinger perturbation theory was the Stark effect in the hydrogen atom [21], for which the first two orders of perturbed energies were immediately obtained. A formula for the third order, which required some effort, was delivered a few years later [102]. However, the next order was so tedious that it took almost 50 years to obtain the correct formula [103]. In 1978 Silverstone proposed a solution of the Stark effect in hydrogen to arbitrarily high orders [67]. In this approach the derived formula for the N^{th} order energy $E^{(N)}$ is a polynomial in the parabolic and magnetic quantum numbers:

$$E^{(N)} = 4^{-N} n^{3N-2} \sum_{r \geqslant 0} \sum_{i \geqslant 0} \sum_{j \geqslant 0} E^{(N)}_{rij} M^r k_1^i k_2^j, \tag{2.40}$$

where $k_i = n_i + \frac{1}{2}|m| + \frac{1}{2}, M = \frac{1}{4}(m^2 - 1)$ and $E^{(N)}_{rij}$ are polynomial coefficients computed to seventeenth order and available from the Physics Auxiliary Publication Service (PAPS). To calculate the perturbed energy of a specific state $(n,\ n_1,\ n_2,\ m)$ one can use the N^{th} order energy obtained with Eq. (2.40) and insert it in the power-series expansions in the field:

$$E = E^{(0)} + E^{(1)} F + E^{(2)} F^2 + \cdots . \tag{2.41}$$

Despite the fact that for the Stark effect perturbation theory yields a nonconvergent, asymptotic expansion of the energy [97, 104], it can still be used as a good estimation for low fields if the expansion is not carried too far [105]. For a given maximum error ϵ one can calculate the value of the field strength $F_N(\epsilon)$, for which the N^{th} term has a magnitude ϵ:

$$F_N(\epsilon) = \left| \frac{\epsilon}{E^{(N)}} \right|^{1/N} . \tag{2.42}$$

Perturbation theory is more accurate for the $n_1 - n_2 \ll 0$ resonances (red states) than for the $n_1 - n_2 \gg 0$ (blue states), as has been shown experimentally by Koch [105], who got an accurate value of the energy for the reddest state (30, 0, 29, 0). The discrepancy between the theory and the experiment was less than the experimental uncertainty. In contrast, the energy of the blue state (25, 21, 2, 1) could not be given with the same high accuracy due to the oscillatory behavior of the perturbation series about the experimental result. Moreover, this theory is poorly suited for describing anticrossings in multi-electron atoms [94]. Nevertheless, when used in a pure Coulomb potential, where levels actually cross, it works rather well [75].

2.5.2 Wentzel-Kramers-Brillouin – Quantum Defect theory (WKB-QD)

For the hydrogen atom in a very strong electric field it is more convenient to solve the differential equations (2.20a) and (2.20b) by means of an approximation method than by using perturbation theory [63]. The WKB method is especially suitable for states with a high principal quantum number n and can be used for arbitrary field strength F practically over the entire energy domain. The first successful implementation of this method was made by Lanczos already in 1930 [106]. Using the expressions for wave functions $\chi_1(\xi)$ and $\chi_2(\eta)$ from Eq. (2.30a) and (2.30b) the differential equations can be re-written as:

$$\frac{d^2\chi_1}{d\chi_1^2} + \phi_1(\xi)\chi_1 = 0, \tag{2.43a}$$

$$\frac{d^2\chi_2}{d\chi_2^2} + \phi_2(\eta)\chi_2 = 0, \tag{2.43b}$$

where the functions $\phi_1(\xi)$ and $\phi_2(\eta)$ are essentially the "local kinetic energies" of the electron at the position ξ and η, respectively. The energy function $\phi_1(\xi) = \frac{1}{2}E + \frac{Z_1}{\xi} - \frac{m^2-1}{4\xi^2} - \frac{1}{4}F\xi$ has two classical turning points ξ_1 and ξ_2 defining a region where it has positive values. The wave function $\chi_1(\xi)$ has the unnormalized approximate form [63, 89, 101]:

$$\chi_1(\xi) = a\phi_1^{-1/4}(\xi)cos\left(\int_{\xi_1}^{\xi_2}\sqrt{\phi_1(\xi)}dx - \frac{\pi}{4}\right), \tag{2.44}$$

where a is the normalization constant. This function must be bound and decrease exponentially on both sides of the turning points, thus the following quantization condition can be written:

$$\int_{\xi_1}^{\xi_2}\sqrt{\phi_1(\xi)}dx = \left(n_1 + \frac{1}{2}\right)\pi. \tag{2.45}$$

The approximation 2.45 is very accurate for large n_1, fairly accurate for small values of n_1 and in the region $\xi \sim 0$ it breaks down. However, this limitation can be bypassed through the Langer correction by replacing the centrifugal term $\left(\frac{m^2-1}{4\xi^2}\right)$ with $\left(\frac{m^2}{4\xi^2}\right)$, as shown in Ref. [89]. For fixed values of E, m and F there exists many solutions to Eq. (2.45), which correspond to different values of Z_1 and n_1. Consequently, allowed values of Z_2 are obtained from the condition $Z_1 + Z_2 = 1$ and serve as an input to the characterization of the $\chi_2(\eta)$ wave function.

To determine the asymptotic form of $\chi_2(\eta \to \infty)$ in the Coulomb + Stark potential Harmin proposed a theory based on a separation of physical space into an

inner and outer region. In the former region the interaction of the electron with the electric field is negligible compare to that with the core, hence the potential is purely Coulombic + centrifugal, i.e. $V_1(\eta) = \frac{m^2}{4\eta^2} - \frac{Z_2}{\eta}$. In the latter region the Coulomb field is negligible and the potential reduces to $V_2(\eta) = -\frac{1}{4}F\eta$ [89]. For all values of η, except $\eta \sim 0$, the $\chi_2(\eta)$ wave function is approximated by the WKB solution. By matching forms of $\chi_2(\eta)$ from the inner and outer regions the asymptotic phase and amplitude of $\chi_2(\eta)$ is obtained for fixed $n_1,\ m,\ E,\ F$ and Z_2. An extension of this approach to nonhydrogenic atoms allowed obtaining an excellent agreement with an experimental photoionization spectrum of Na [90, 107] as well as with Li photoionization spectra [91].

2.5.3 Wave packet calculations

During a photoionization process in a DC electric field time-dependent electron wave packets are created, which rapidly evolve in the combined Coulomb + Stark potential. The dynamics of such wave packets is determined by the static electric field, the laser polarization, the wavelength of the laser light and the pulse duration. It has been shown that precisely calculated wave packets allow for a deeper insight into dynamical processes of photoionization in Rydberg atoms [108, 109]. In this thesis a vast amount of calculations are based on a wave packet propagation approach in which the time dependent Schrödinger equation is solved by using a split-operator technique. The principle of this method is to separate the time evolution operator $U(t, t_0)$ (see Eq. (2.48)) into parts, which are easy to calculate for each calculation step. Presented below, a theoretical description of this method is given based on the PhD thesis of Antoine M. Ollagnier [110].

The wave function $\psi(\vec{r}, t)$ at a given time delay t and at the position $\vec{r}$ obeys the time dependent Schrödinger equation:

$$i\frac{\partial}{\partial t}\psi(\vec{r}, t) = H\psi(\vec{r}, t), \tag{2.46}$$

which can be re-written in terms of the time evolution operator $U(t, t_0)$ as:

$$\psi(\vec{r}, t) = U(t, t_0)\psi(\vec{r}, t_0), \tag{2.47}$$

where $\psi(\vec{r}, t_0)$ is the initial wave function at t_0, and $U(t, t_0)$ is defined by:

$$U(t, t_0) = 1 - i\int_{t_0}^{t} HU(t', t_0)dt'. \tag{2.48}$$

For a time-independent Hamiltonian, $U(t, t_0)$ is simply:

$$U(t, t_0) = e^{-iH(t-t_0)}. \tag{2.49}$$

The following Hamiltonian is considered:

$$H = H_{at} + H_F + H_{int}, \tag{2.50}$$

where H_{at} is the atomic part corresponding to:

$$H_{at} = -\frac{1}{2}\frac{\partial^2}{\partial r^2} + \frac{L^2}{2r^2} + V(r), \tag{2.51}$$

where L is the angular momentum operator and $V(r)$ is the atomic potential describing the interaction between the valence electron and the ionic core.

The second term on the right-hand side of Eq. (2.50), i.e. H_F corresponds to the Stark Hamiltonian associated with the static electric field F. It is given by:

$$H_F = Fz = Frcos\theta, \tag{2.52}$$

where F is the strength of the electric field, and θ the polar angle between the position vector $\vec{r}$ and the axis of the electric field.

Finally, the last term on the RHS of Eq. (2.50) H_{int} defines the interaction between the atom and the laser field.

Using first order perturbation theory, the wave function $\psi(\vec{r}, t)$ describing excitation from the initial state at energy E_0 to the final state of E is given by:

$$\psi(\vec{r}, t) = \Phi(\vec{r})e^{-iE_0 t} + \Psi(\vec{r}, t)e^{-iEt}, \tag{2.53}$$

where Φ is the initial wave function of the bound electron at time t_0 at the energy E_0 which satisfies the equation:

$$H_{at}\Phi = E_0\Phi. \tag{2.54}$$

Combining equations (2.46), (2.50) and (2.53) leads to:

$$i\frac{\partial\Psi}{\partial t} - (H_{at} - E + Fz)\Psi = S(\vec{r}, t). \tag{2.55}$$

The excitation process is taken into account via the source term $S(\vec{r}, t)$ defined as:

$$S(\vec{r}, t) = exp\left(\frac{t^2}{\Delta t_{pulse}^2}\right) S(r)Y_l^m \tag{2.56}$$

where Y_l^m is the spherical harmonic describing the initial state characterized by quantum numbers l and m, and $S(r)$ describes the radial dependence of the initial wave function. In practice, this term is defined by:

$$S(r) = r^2 e^{-2r}. \tag{2.57}$$

The width of the laser pulse Δt_{pulse} is taken into account in the source term by a Gaussian dependence.

Integration of equation (2.55) leads to the following propagator:

$$\Psi(t+\Delta t) = \frac{\left[1 + i\frac{\Delta t}{2}(H_{at} + Fz - E)\right]}{\left[1 - i\frac{\Delta t}{2}(H_{at} + Fz - E)\right]}\Psi(t) + \\ + \left[-i\Delta t + \frac{\Delta t^2}{2}(H_{at} + Fz - E)\right] S(\vec{r}, t + \frac{\Delta t}{2}). \tag{2.58}$$

The first term corresponds to the first order Padé approximation of the operator $exp(-i(H_{at} + Fz - E)\Delta t)$. It can be split as follows:

$$\frac{\left[1 + i\frac{\Delta t}{2}(H_{at} + Fz - E)\right]}{\left[1 - i\frac{\Delta t}{2}(H_{at} + Fz - E)\right]}\Psi(t) = e^{-i(H_{at}+Fz-E)\Delta t}\Psi(t) = \\ = e^{-iFz\frac{\Delta t}{2}} e^{-i(H_{at}-E)\Delta t} e^{-iFz\frac{\Delta t}{2}}\Psi(t). \tag{2.59}$$

The first part only acts on the angular part of the wave function, while the second part only acts on the radial part. In order to be able to apply the exponential terms, these operators have to be linearized. For the angular part, a [2,2] order Padé approximant is used and a canonical linearization leads to:

$$e^{-iFz\frac{\Delta t}{2}}_{[2,2]} = \left[\frac{1 - iFza\frac{\Delta t}{2}}{1 + iFza\frac{\Delta t}{2}}\right]\left[\frac{1 - iFzb\frac{\Delta t}{2}}{1 + iFzb\frac{\Delta t}{2}}\right] + o(\Delta t^4) \tag{2.60}$$

with $a = (1/2 + i\sqrt{3}/6)$ and $b = (1/2 - i\sqrt{3}/6)$.

For the radial part, a [1,1] order Padé approximant is used:

$$e^{-i(H-E)\Delta t}_{[1,1]} = \left[\frac{1 - i(H_{at} - E)\frac{\Delta t}{2}}{1 + i(H_{at} - E)\frac{\Delta t}{2}}\right] + o(\Delta t^2). \tag{2.61}$$

Finally, equation (2.58) can be re-written as follows:

$$\Psi(t+\Delta t) = \left[\frac{1-iFza\frac{\Delta t}{2}}{1+iFza\frac{\Delta t}{2}}\right]\left[\frac{1-iFzb\frac{\Delta t}{2}}{1+iFzb\frac{\Delta t}{2}}\right]\cdot$$
$$\cdot\left[\frac{1-i(H_{at}-E)\frac{\Delta t}{2}}{1+i(H_{at}-E)\frac{\Delta t}{2}}\right]\left[\frac{1-iFza\frac{\Delta t}{2}}{1+iFza\frac{\Delta t}{2}}\right]\left[\frac{1-iFzb\frac{\Delta t}{2}}{1+iFzb\frac{\Delta t}{2}}\right]\Psi(t)+$$
$$+\left[-i\Delta t+\frac{\Delta t^2}{2}(H_{at}+Fz-E)\right]S\left(\vec{r},t+\frac{\Delta t}{2}\right) \quad (2.62)$$

Because of the cylindrical symmetry of the Hamiltonian the dependence on the azimuthal angle φ is not included. As a consequence, the propagation occurs in 2 dimensions using a (k,l) grid, where k is the radial coordinate and l is orbital angular momentum.

The Stark operator $Fz = Frcos(\theta)$ operates on the angular part of Ψ according to:

$$cos(\theta)Y_l^m = \sqrt{\frac{(l+m+1)(l-m+1)}{(2l+3)(2l+1)}}Y_{l+1}^m + \sqrt{\frac{(l+m)(l-m)}{(2l+1)(2l-1)}}Y_{l-1}^m. \quad (2.63)$$

The radial part of the atomic Hamiltonian is given by (63):

$$-\frac{d^2}{dr^2}+\frac{l(l+1)}{2r^2}+\left[-\frac{Z_l}{r}-\frac{\alpha_d}{2r^4}\left(1-e^{-(r/r_c)^3}\right)^2\right], \quad (2.64)$$

where α_d is the dipole polarizability of the ionic core and r_c is its radius. In the region $r \leqslant r_c$ the potential experienced by the valence electron is no longer $-1/r$. The effective charge $Z_l(r)$ is given by:

$$Z_l = 1+(Z-1)e^{-\alpha_l^{(1)}r}+\alpha_l^{(2)}re^{-\alpha_l^{(3)}r}. \quad (2.65)$$

The values of the coefficients α_l can be found in e.g.[98, 111–113].

At a fixed time delay t, the wave packet is written as:

$$\psi(\rho,z) = \sum_{l=0}^{l_{max}}\Psi(k,l)Y_l^m(cos\theta). \quad (2.66)$$

In calculations, the total wave function is integrated over time and the quantity $\rho|\psi(\vec{r},t))|^2$ is computed, which describes the probability of finding an electron, where $\rho = \sqrt{r^2-z^2}$. Also the time-dependent flux of ejected electrons is calculated providing an insight into the dynamics of the photoionization process.

3 Experimental facilities

This chapter deals with all technical aspects of photoionization microscopy experiments, on hydrogen and helium atoms, whose results are presented and discussed in Chapters 4, 5 and 6. The chapter is divided into two parts, each dedicated to one experimental setup. At the beginning of each part the general idea of the experiment is described and the following sections present crucial steps of the experiment in greater detail. This includes the design of an atomic or metastable source, description of lasers systems, of an imaging spectrometer and of the data acquisition procedure. In these sections also efficiency calculations of the overall processes are provided.

3.1 Photoionization microscopy of hydrogen atoms

The experiment on hydrogen atoms was performed making use of an experimental setup shown in Fig. 3.1, which comprised two differentially pumped vacuum chambers. Atomic hydrogen was produced by photodissociating H_2S gas, introduced into a first vacuum chamber by a pulsed valve (a) that was facing upwards (along the x-axis), using 213 nm light from a Nd:YAG laser (Quanta-Ray, Spectra Physics). The polarization of the 213 nm laser was vertical (along the x-axis), maximizing production of H-atoms with a recoil velocity in the yz-plane. The atomic hydrogen beam was formed by a 3 mm aperture (b) separating the first vacuum chamber from the second vacuum chamber, which contained a velocity map imaging (VMI) spectrometer [114]. The hydrogen atoms entered the VMI through a 1.5 mm hole in the repeller electrode (c). In the VMI, a static electric field in the range from 200 to 850 V/cm was created by applying a voltage difference across the repeller and extractor (d) electrodes. A third electrode (e) in the VMI contained deflection plates and was kept at ground potential.

The field-free ionization potential of the hydrogen atom is 13.6 eV [115], meaning that to photoionize it from the $^2S_{1/2}$ ground state one can choose a one-photon absorption scheme employing light at 91.2 nm. Alternatively, hydrogen can be firstly excited to an $n = 2$ state by means of the Lyman-alpha line and secondly photoionized at 364.7 nm. In our experiments the hydrogen atoms were excited to a mixture of $n = 2$ s– and p–states by means of a two-photon transition, making use of 3 mJ, 243 nm, 8 ns pulses from a tunable dye laser (PDL-3, Spectra Physics). From there,

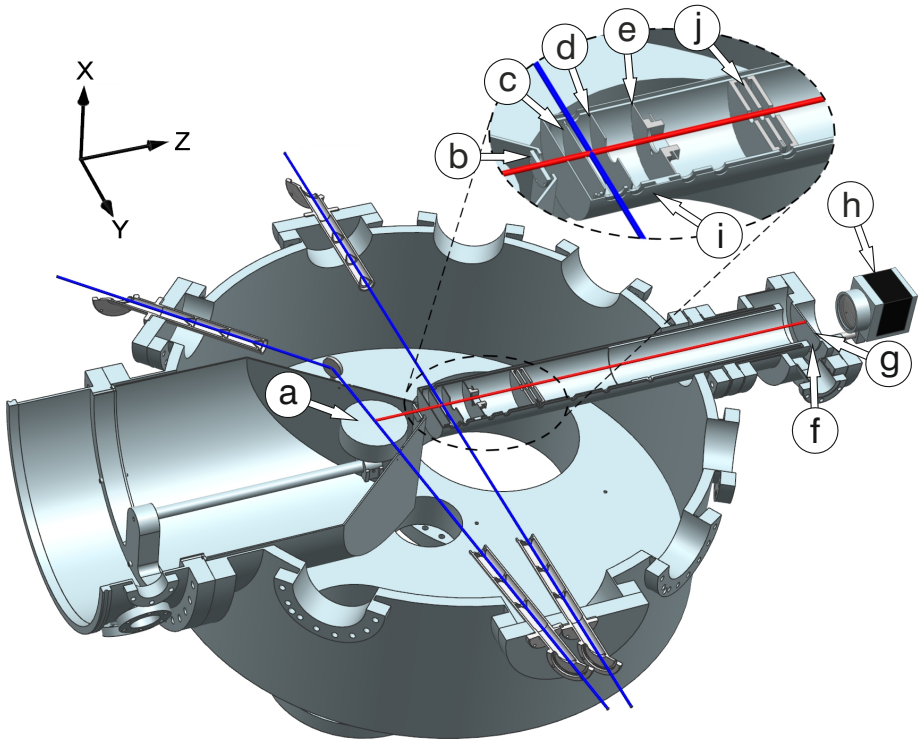

Figure 3.1: Schematic overview of the hydrogen experiments. H_2S gas was introduced into a first vacuum chamber by a pulsed valve (a) and subsequently it was photodissociated with laser light at 213 nm. A 3 mm aperture (b) placed between the first and second vacuum chambers served as a skimmer forming the atomic hydrogen beam. Hydrogen atoms passing the velocity map imagining spectrometer were ionized by means of a two-color process. By applying a voltage difference across the repeller (c) and extractor (d) electrodes and keeping the third electrode (e) at ground potential the photoelectrons were accelerated in a DC electric field towards a position-sensitive detector comprising micro-channel plates (f), a phosphor screen (g) and a CCD camera (h). The whole spectrometer was surrounded by a μ-metal shield (i), which suppressed the earth magnetic field. One-third of the way toward the detector the photoelectrons passed an Einzel lens (j), which enabled magnification of photoelectron images by up to one order of magnitude.

they were ionized using 600 μJ, 8 ns, narrow-band, tunable laser pulses with wavelengths between 365 and 367 nm, obtained by frequency doubling the output of a Fourier-limited, home-built three-stage, four-pass pulsed dye amplifier, using a cw (continuous wave) ring-dye laser as its seed (899-29 Autoscan II, Coherent) and a Nd:YAG laser (GCR-290, Spectra Physics) as its pump. By doing so, the emphasis was on ionization processes resulting from the excitation of high-lying, auto-ionizing Stark states. The polarization of the 243 nm laser was perpendicular to the static electric field axis (i.e. parallel to the two-dimensional detector), whereas the polar-

ization of the 365-367 nm laser was either parallel or perpendicular to the static electric field axis. The resulting photoelectrons were projected onto a micro channel plate (MCP) detector (f) followed by a phosphor screen (g), and recorded with a CCD (charged coupled device) camera (h). The magnetic field inside the VMI was suppressed by a μ-metal shield (i). An electrostatic zoom lens (j) was used [116] to magnify the images by about one order of magnitude without deteriorating the image quality. Images were typically acquired for 5000 and 10000 laser shots for non-resonant and resonant excitation of a Stark state, respectively.

3.1.1 Characteristics of the atomic hydrogen source

To produce atomic hydrogen H_2S gas has been chosen due to its continuous absorption spectrum in the region of 160-270 nm with a maximum at about 195 nm [117]. Hydrogen sulfide is a toxic, flammable, colorless, liquefied gas, which inhaled at high concentrations can result in unconsciousness, coma, and death. Therefore extra safety precautions were taken during the experiments, e.g. all gas connections were contained within housings connected to an external gas exhaust and personal safety was guarded by H_2S detectors. The hydrogen sulfide gas was injected into the first vacuum chamber by a pulsed valve mounted perpendicularly to the VMI (along the x-axis shown in Fig. 3.1). The gas flow was controlled by changing the distance between a sealing viton disc ($\phi = 1$ mm) and a 1 mm nozzle, making use of a piezo element [118]. The sealing disc was mounted on a stainless steel pillar (10 mm long), which was connected to a piezo disc ($\phi = 50$ mm) as shown in Fig. 3.2b. It turned out that the piezo discs (P-286.23, PI) break down rather quickly while being exposed to a highly corrosive gas, as shown in Fig. 3.2 where a picture of a brand new piezo disc (a) is compared with one taken after 10 hours exposure to H_2S gas (b). To overcome this limitation a vacuum grease (Fomblin Grease VAC3) was used, which was smeared on the piezo element creating a 1 mm thick protective

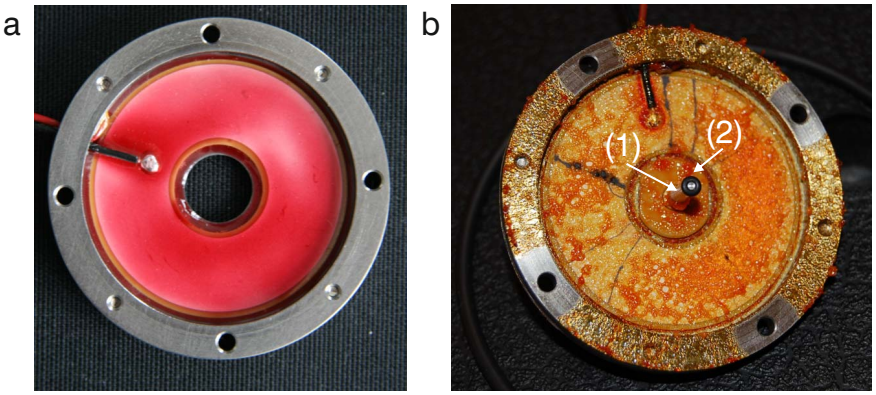

Figure 3.2: Comparison between a brand new piezo disc (a) and one exposed for 10 hours to H_2S gas with noticeable cracks on the disc surface (b). In the latter image the stainless steel pillar (1) with a viton disk (2) mounted on the piezo disc are visible.

layer and providing a trouble-free operation for a period of 6 months. In experiments the pulsed valve was operated at 10 Hz by a home-build piezo valve voltage driver.

As photolysis light source, a Nd:YAG laser (Quanta-Ray, Spectra Physics) was used, which delivered 7 ns light pulses at 213 nm by means of frequency mixing 1064 and 266 nm pulses in a 12×12×2 mm BBO (barium borate) crystal. An average output energy of 1.5 mJ per pulse was achieved at 10 Hz. Within one laser pulse the number of H_2S molecules undergoing dissociation can be calculated as:

$$N_{diss} = N\Big[1 - exp\Big(- 5.03 \times 10^{15} \frac{\sigma_{abs} \cdot E \cdot \lambda}{l_0^2}\Big)\Big], \tag{3.1}$$

where N is the number of H_2S molecules, σ_{abs} is the absorption cross section at the photolysis wavelength λ[nm] ($\sigma_{abs} = 2{\times}10^{-18}$ cm^{-2} at 213 nm [117]), E is the energy of the laser pulse [J/pulse] and l_0 is the photolysis width [cm]. The number of molecules N can be expressed as:

$$N = n_0 \cdot l_0^3, \tag{3.2}$$

where n_0 is the density of molecules in the photolysis volume of l_0^3. A reasonable H atom beam quality, i.e. where inelastic collisions with residual H_2S or HS fragments do not significantly change the H atom velocity, is obtained as long as $n_0 \cdot l_0 \leqslant 5{\times}10^{15}$ cm^{-2}. Hence, equation 3.1 can be re-written as:

$$N_{diss} = 5 \times 10^{15} \cdot l_0^2\Big[1 - exp\Big(- 5.03 \times 10^{15} \frac{\sigma_{abs} \cdot E \cdot \lambda}{l_0^2}\Big)\Big]. \tag{3.3}$$

Fig. 3.3a shows the calculated number of H atoms arising from photodissociation of H_2S gas by making use of 1.5 mJ at 213 nm as a function of the photolysis width l_0. One can see that this process is highly inefficient for tightly focused laser beams, whereas the focal spot of 0.1 cm ensures 90% production of H atoms. The process starts to saturate around $l_0 = 0.2$ cm thus the beam size should not be bigger than this value. In the experiment this requirement was fulfilled by placing a $f = 1$ m lens 80 cm in front of the pulsed valve ensuring a 213 nm beam size of 0.1×0.2 cm in the photodissociation region. The efficiency of the atomic hydrogen source was further optimized by setting the time of the H_2S gas injection to 40 μs prior the laser pulse and keeping the pressure in the source chamber with the loaded gas at $3.8{\times}10^{-4}$ Torr. At higher pressures the condition $n_0 \cdot l_0 \leqslant 5 \times 10^{15}$ cm^{-2} was not optimum and the quenching of hydrogen atoms, due to collisions with other atoms and molecules, was significant.

To ensure the highest density of H_2S molecules in the photolysis region the 213 nm laser beam was positioned approximately 1 mm above the pulsed valve. During experiments H_2S gas was injected through the 1 mm nozzle with a speed of 460 m/s providing a gas pressure of 0.6 Torr at the exit of the nozzle. By making a crude approximation that the pressure in the photolysis region was the same as at

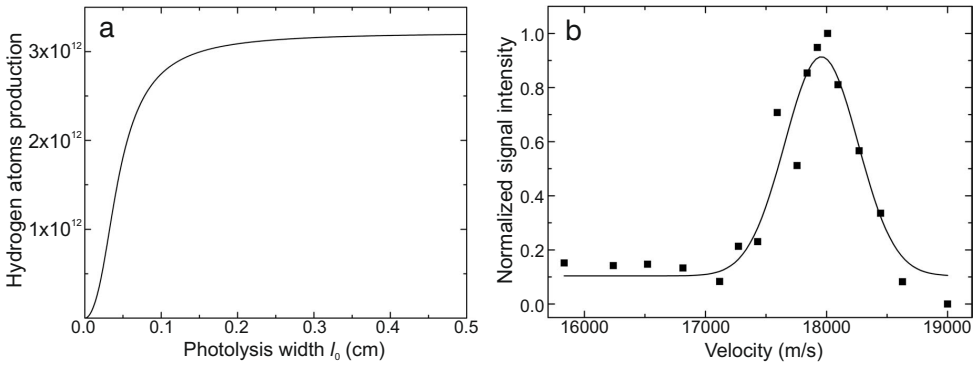

Figure 3.3: (a) Dependence of the number of hydrogen atoms produced as a function of the photolysis width calculated for an average energy of 1.5 mJ/pulse at 213 nm, subject to the conditions that the product of n_0 and l_0 was $5{\times}10^{15}$ cm^{-2}. (b) Measured velocity profile of the hydrogen atomic beam (squares) fitted with a Gaussian profile (solid line) indicating that the mean velocity of the H fragments was 18000 m/s and the FWHM (hull width at half maximum) was 700 m/s.

the nozzle exit the average density of H_2S molecules had a value of $2{\times}10^{16}$ H_2S/cm^3 and the amount of produced hydrogen atoms by making use of 1.5 mJ at 213 nm was $5.5{\times}10^{12}$ H atoms per pulse.

3.1.2 Transport and density of H atoms in the interaction region

After photodissociation the atomic hydrogen beam was formed by a 3 mm hole separating the two vacuum chambers (approximately 6.5 cm away from the pulsed valve) followed by a 1.5 mm hole in the repeller plate, providing a well-collimated beam. The number of hydrogen atoms transported into the interaction region inside the VMI can be calculated as:

$$N_{trans} = N_{diss} \cdot I(\theta) \cdot \Delta\Omega, \tag{3.4}$$

where $I(\theta)$ is the angular distribution of H fragments and $\Delta\Omega$ is the solid angle.

When a molecule is directly dissociated using linearly polarized light the angular distribution of fragments is given by [119]:

$$I(\theta) = \frac{1}{4\pi}\left[1 + 2\beta P_2(cos\theta)\right], \tag{3.5}$$

with $P_2(cos\theta)$ being the second-order Legendre polynomial, θ the angle between the polarization vector and the detection direction and β the anisotropy parameter.

At 222 nm the β parameter for H_2S has a value of -0.42±0.01 [119] meaning that most of the H atoms have their velocity vector in a plane perpendicular to the laser polarization. Therefore, in the experiment the laser polarization was chosen to be vertical, i.e. along the x-axis, to maximize the production of H atoms in the direction of the VMI.

The solid angle of a cone with an apex angle 2φ can be calculated as $\Delta\Omega = 2\pi(1 - cos\varphi)$. Considering the experimental geometry $\varphi = arctg\left(\frac{r}{d}\right)$, where r is the radius of the hole in the repeller plate and d is the distance between the interaction region inside the VMI and the photolysis region (d = 9.5 cm), hence $\Delta\Omega = 1.96 \times 10^{-4}$. Taking this into account the percentage of hydrogen atoms resulting from the photodissociation of H_2S molecules and being transported into the interaction region is 0.002% and corresponds to a value of $N_{trans} = 1.2 \times 10^8$ H atoms/pulse.

In the interaction region H atoms may be photoionized by absorbing three photons at 243 nm if the laser pulse energy is high enough. By detecting the created H^+ ions and changing the time delay between the photolysis and photoionization laser pulses the velocity spread of the atomic hydrogen beam was measured. Fig. 3.2b shows experimentally measured velocities (black squares) with a fitted Gaussian profile (solid line) indicating the mean velocity of H fragments to be $\vartheta = (1.800 \pm 0.035) \times 10^4$ m/s. Due to the velocity spread the hydrogen atomic beam occupied a certain volume that can be calculated as $\vartheta_{beam} = \pi r^2 l_z$, where l_z is the longitudinal spread in the z-axis given as: $l_z = (\vartheta_{max} - \vartheta_{min}) \cdot d/\vartheta = 0.37$ cm. Thus the beam volume is $V_{beam} = 0.0065$ cm^3 and therefore, the density of H atoms in the interaction region is:

$$n = \frac{N_{trans}}{V_{beam}} = 1.9 \times 10^{10} \frac{Hatoms}{pulse}. \tag{3.6}$$

3.1.3 Two-photon excitation into the mixture of 2 $s-$ and $p-$ states

As has been mentioned at the beginning of Section 3.1 atomic hydrogen has a field-free ionization potential of 13.6 eV and therefore, in our experiments H atoms were photoionized with three photons including a two-photon resonant transition at 243.06 nm to a mixture of $n = 2$ $s-$ and $p-$states. The photoexcitation step was accomplished by making use of UV light obtained by frequency doubling the output of a tunable pulsed dye laser comprising an external amplification stage. In this section first the laser setup is described followed by calculations of the efficiency of two-photon excitation into the $n = 2$ state.

Source of 243 nm laser beam

The pulsed dye laser (PDL-3, Spectra Physics) delivered tunable light in the visible range with an average bandwidth of 0.1 cm^{-1}. It was pumped with 110 mJ at 355 nm provided by a Nd:YAG laser (GCR-290, Spectra Physics). By using

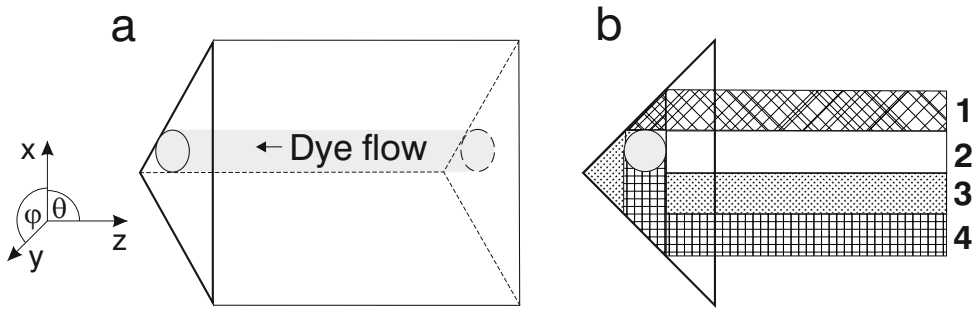

Figure 3.4: (a) Side view of a Bethune cell with a circular capillary tube through which the dye flows. (b) End view of the cell with a pump beam divided into four equal segments (1-4) that uniformly excite the dye from the top, front, back and the bottom.

Coumarin 480 dye the laser delivered 8 ns pulses with average energy of 2 mJ at 486 nm. The pulses were further amplified in an external dye cell filled with the same dye at a concentration of 2.5×10^{-4} mol/l. The cell was pumped with 220 mJ at 355 nm from the Nd:YAG laser ensuring further amplification of the pulse energies by approximately 10 times. After the amplification stage the second harmonic was generated with a BBO crystal (6×6×5 mm), which led to the production of 8 ns pulses with an average energy of 3 mJ at 243 nm. Prior to being sent into the interaction region the beam size was shaped to 2.5 mm in diameter by passing a 3:2 telescope.

The external dye cell was of the Bethune type [120], i.e. a standard 45 deg right angle prism with a drilled hole for dye solution as shown in Fig. 3.4a. In this geometry the pump beam must have a vertical width four times bigger than the bore diameter to ensure homogenous pumping of the dye. As shown in Fig. 3.4b when pump light enters the cell though an input window it undergoes internal reflections and four equal segments (1-4) homogeneously pump the top, front, back and the bottom of the dye, respectively. The advantage of using a large pumping area is that it prevents damaging of the input window. Even though the amplified beam spatial profile is decoupled from that of the pump beam the temporal profile is affected as a dye amplifier mimics the intensity fluctuations of the pump pulses. Also it is important that the seed beam must have a size slightly bigger than the bore as a complete filling ensures more efficient energy extraction, reduces saturation in the dye cell and helps to deplete amplified spontaneous emission (ASE). In the experiments, the Bethune cell had a bore diameter of 4 mm and a length of 35 mm. It was mounted on translation stages enabling its precise positioning in the xy direction and rotation along φ and θ angles (see Fig. 3.4). To shape the Nd:YAG beam to the size of 16×35 mm a $f = -100$ mm plano-concave lens was used.

Efficiency of the photoexcitation step

For a two-photon excitation process with a single light beam the population in the excited state can be written as [121]:

$$N_{excited} = N_{ground}\Big(1 - exp\Big(\frac{\sigma_{2\gamma} I^2 \Delta T}{h\nu}\Big)\Big). \tag{3.7}$$

with N_{ground} being the population in the ground states, $\sigma_{2\gamma}$ the two-photon absorption cross-section, I the intensity of the light beam, ΔT the pulse duration and $h\nu$ the photon energy. The amount of hydrogen atoms in the $^2S_{1/2}$ ground state can be expressed as:

$$N_{ground} = n \cdot V_{inter}, \tag{3.8}$$

where n is the density of H atoms per cm^3 and V_{inter} the volume of interaction between the atomic hydrogen beam ($\phi_H = 0.15$ cm) and the 243 nm laser beam ($\phi_{243} = 0.25$ cm), i.e. $V_{inter} = \pi r_H^2 l_{243} = 0.0044$ cm^3.

The 1s-2s two-photon cross-section for the hydrogen atom is given by the expression [122]:

$$\sigma_{2\gamma} = 2.75 \times 10^{-17}\Big[\frac{cm^4 s}{W}\Big] g(\Delta\Omega) G^{(2)}, \tag{3.9}$$

where $G^{(2)}$ is the two-photon statistic factor, which for dye and excimer lasers has a value of 2 [121], and $g(\Delta\Omega)$ is the spectral linewidth function given by [122]:

$$g(\Delta\Omega) = \frac{\Big(\frac{4ln(2)}{\pi}\Big)^{1/2}}{(\Delta\omega_D^2 + 2\Delta\omega_L^2)^{1/2}}, \tag{3.10}$$

with $\Delta\omega_D$ and $\Delta\omega_L$ being the Doppler and the laser linewidth, respectively. For the experimental conditions $\Delta\omega_D = 9.6 \times 10^{10}$ s^{-1} and $\Delta\omega_L = 1.9 \times 10^{10}$ s^{-1}, hence $g(\Delta\Omega) = 9.4 \times 10^{12}$ s^{-1} and the two-photon cross-section for hydrogen is:

$$\sigma_{2\gamma} = 5.18 \times 10^{-28}\Big[\frac{cm^4}{W}\Big]. \tag{3.11}$$

During the experiments the average energy at 243 nm was 3 mJ/pulse, and the pulse duration was 8 ns giving the light beam intensity of $I = 6$ MW/cm^2. Hence, the population of H atoms in the mixture of $n = 2$ s– and p–states was:

$$N_{excited} = n \cdot N_{inter}\Big(1 - exp\Big(-\frac{\sigma_{2\gamma} I^2 \Delta T}{h\nu}\Big)\Big) = 1.5 \times 10^4 \frac{H^*_{atoms}}{pulse}. \qquad (3.12)$$

3.1.4 Photoionization of excited hydrogen atoms – Pulsed Dye Amplifier

The final and the most crucial step in the experiments on hydrogen atoms was photoexcitation into Stark states, whose energy levels were located above the saddle point energy and below the field-free ionization potential. This step required a narrow-band, tunable in the rage of 365-367 nm and a pulsed laser system operated at the same frequency as the pulsed valve and the PDL-3.

Pulse amplification of a continuous single mode dye laser has found wide application in experiments where tunable, high power and near Fourier-limited pulses are required [123–126]. This technique was first demonstrated by Salour [127], who amplified the output of a cw dye laser in a chain of three dye cells pumped by a N_2 laser. By pumping an organic dye in a cell, molecules are populated into the first excited (electronic) singlet manifold. In a very short time they decay into low-lying substates of the manifold through non-radiative transitions. Subsequently, molecules can radiate their energies and drop to one of substates in the lowest singlet vibration-rotation manifold (spontaneous emission). If light is present during that process molecules can be stimulated to emit coherent photons with the same frequency as the input photons (stimulated emission). In this way a pulsed dye amplifier (PDA) generates coherent light pulses at a wavelength that is controlled by a seed laser. The design of Salour resulted in pulses with a peak power of 100 kW and a linewidth of 60 MHz in the visible. Since then many variations have been introduced leading to a higher peak power [123], greater gain [128] and significant reduction of ASE [129]. The laser system used in the hydrogen experiments was a three-stage, four-pass pulsed dye amplifier based on a design by Cromwell [130]. It is schematically shown in Fig. 3.5 with a general description of its operation given in the figure caption. In the text below all elements of the PDA are explained in detail.

Lasers

A ring dye laser (899-29 Autoscan II, Coherent) [131] pumped by a cw Nd:YVO4 (Verdi V-12, Coherent) laser was exploited as the seed beam for the PDA. This dye laser delivered a continuous, well-characterized and tunable output over the whole visible spectrum with a typical bandwidth of 500 kHz. An external wavelength meter combined with a software package ensured automatic selection of wavelengths with an absolute accuracy of ±200 MHz and a reproducibility of ±50 MHz over the 450 to 900 nm operating range. In experiments on hydrogen atoms Pyridine 2 dye ensured operation in the range of 725-745 nm providing an average output power of 190 mW at 725 nm. As the pump beam for the PDL, a Q-switch Nd:YAG laser (Quanta-Ray GCR-3, Spectra Physics) was used. This laser was chosen due to its high peak power at 532 nm – a wavelength readily absorbed by many dyes. At 10 Hz it delivered 8 ns

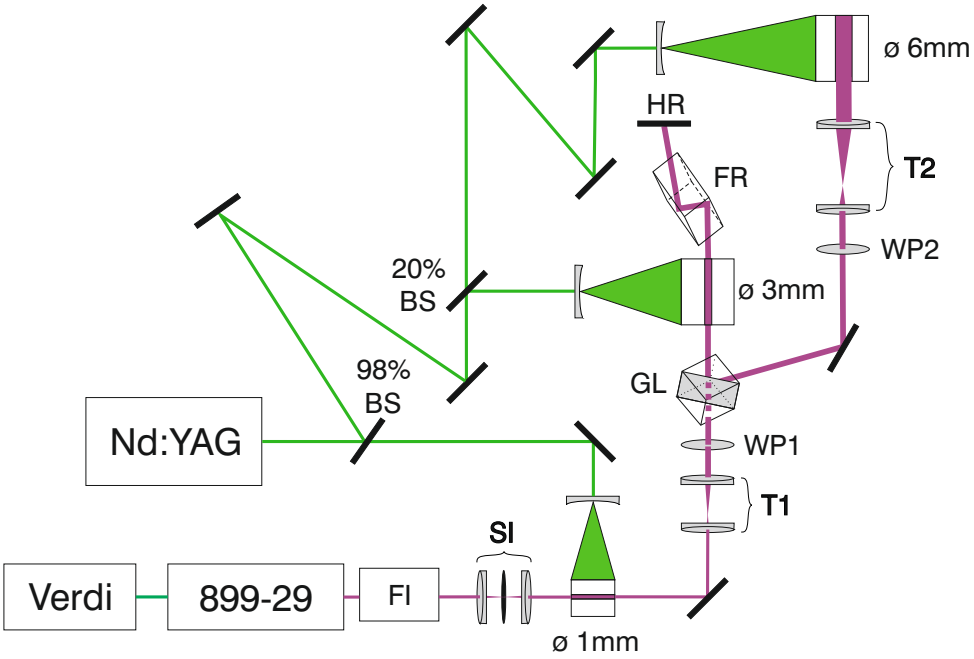

Figure 3.5: Schematic representation of a home-built pulsed dye amplifier (PDA) laser system, which comprised a ring-dye laser (899-29, Coherent), pumped by a Nd:YVO4 laser (Verdi, Coherent). The vertically polarized output beam passed first through a Faraday isolator (FI) and then through a spatial isolator (SI) composed of two achromatic doubles and a pin-hole. The latter shaped the beam before entering a ϕ = 1 mm dye cell, pumped with 2% of the output energy of a Nd:YAG (GCR-3, Spectra Physics) laser, provided by a 98% beam splitter (BS). After amplification in the first dye cell the beam passed through a 1:3 telescope (T1), a half wave plate (WP1), which rotated the polarization by 45 deg, and a Glan-Laser (GL) polarizer. In the second ϕ = 3 mm dye cell the beam was amplified twice. The dye cell was pumped with 20% of the output power delivered by the Nd:YAG laser beam. After the first amplification the beam was reflected back to the cell by using a high reflecting mirror (HR). The beam polarization was rotated by 90 deg due to a double pass through a Fresnel rhomb (FR) ensuring its reflection by the GL polarizer. After passing a wave plate (WP2) the polarization was rotated back to 0 deg and the beam diameter was doubled by a 1:2 telescope (T2) before it entered the last dye cell ϕ = 6 mm, where the final amplification took place.

pulses with the average energy of 400 mJ per pulse. By making use of beam splitters the pump energy was distributed in the ratio of 2:20:78 over the three dye cells, as shown in Fig. 3.5.

Optical and spatial isolators

Before entering a chain of amplifiers the seed beam passed through two isolators. The first one, a Faraday isolator, prevented amplified spontaneous emission from

the amplifier chain to go back to the 899-29 and cause mode-hopping. This optical isolator consisted of two Glan-Laser calcite polarizers, a Faraday rotator and a half-wave plate as shown in Fig. 3.6. The transmission through the Faraday isolator was independent of wavelength, due to broadband antireflection coatings, and had a maximum value of 70%. The Faraday isolator worked as follows: the laser beam passed through the first polarizer (GL1), which was set to pass vertically polarized light – the polarization of the seed beam. Subsequently, the beam passed through a Faraday rotator which rotated the polarization of light by +45 deg due to the Faraday effect. Then the beam was filtered by the second polarizer (GL2), which was set for this polarization. At the end light traveled through a half-wave plate (WP) which rotated the polarization plain back to a vertical direction. If unpolarized light (e.g. ASE) was coming in the opposite direction, namely from the amplifier chain to the 899-29 laser, it was first filtered by the +45 deg polarizer (GL2) and then the Faraday rotator flipped polarization to 90 deg (horizontally polarized). Consequently, the light was completely blocked by the GL1 polarizer.

The second isolator consisted of two achromatic doublet lenses and a pinhole. This spatial filter played a twofold role: it controlled the growth of ASE and shaped the seed beam profile for the first dye cell. The ASE reduction was possible as the spot size of the laser beam was much bigger than the pinhole diameter. Under these conditions only a well-collimated beam, i.e. the beam from the 899-29 laser, passed through the pinhole whereas an uncollimated beam (e.g. ASE) was efficiently suppressed. For a lens of focal length f and a beam radius w, the pinhole diameter d can be determined as:

$$d < 2w_0 = \frac{2f\lambda}{\pi w} \tag{3.13}$$

where w_0 is the focal radius of the beam and λ is its wavelength. The seed beam had $w = 0.5$ mm at $\lambda = 730$ nm meaning that for a $f = 100$ mm lens the focal spot radius was 46 μm. Therefore, the pinhole diameter was chosen to be $d = 75$ μm. For such a combination of lens and pinhole the measured transmission was 97%.
When light is diffracting on a circular aperture, like a pinhole, it creates an Airy pattern with a bright spot in the center known as the Airy disk. This fact was used to calculate the focal length of the second lens, which re-collimated the beam. The radius of the Airy disk is given by [132]:

$$r = 1.22\frac{f\lambda}{d}. \tag{3.14}$$

For the beam expanding from the 75 μm pinhole the radius of the first minimum is 1 mm at a distance of 84 mm. Therefore, by using a $f = 75$ mm lens the seed beam had a FWHM approximately equal to the first dye cell diameter, i.e. 1 mm.

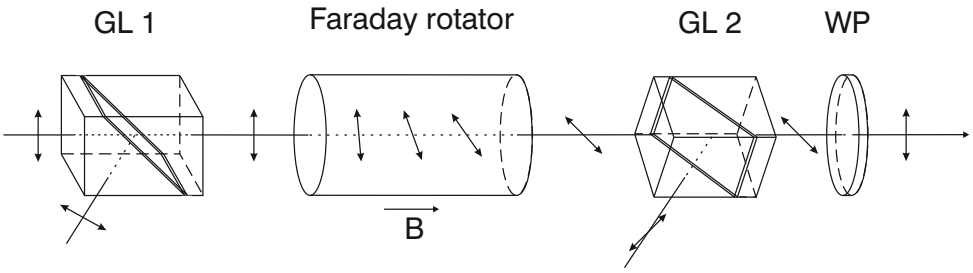

Figure 3.6: Faraday optical isolator comprising two Glan-Laser calcite polarizers (GL1 and GL2), a Faraday rotator and a half-wave plate (WP). The double arrows represent the light polarization and B is the magnetic field direction inside the Faraday rotator.

Amplification stages

For the amplification stages, dye cells of the Bethune type were used, which are described in Section 3.1.3 and shown in Fig. 3.4. The cells had sizes of 1 mm ϕ $\times$20 mm long, 3 mm ϕ $\times$35 mm long and 6 mm ϕ $\times$35 mm long for the first, second and third dye cell, respectively. The cells were mounted on translation stages which allowed their positioning with respect to the seed beam. Before each cell a pair of two achromatic lenses served as telescopes with magnifying powers of $\times$1, $\times$3, and $\times$2 to shape the beam profile for the first, second and third dye cell, respectively. The size of the pump beam was four times wider than the bores owing to plano-concave lenses placed in the front of the Bethune cells.

A polarization rotation technique was used to accomplish a double pass, double amplification through the second dye cell (see Fig. 3.5). Firstly, a half-wave plate (WP1) rotated the beam polarization by 45 deg. Secondly, the beam was filtered through a polarizer (GL) and entered the second dye cell. After passing the cell the polarization was rotated by 45 deg in a $\lambda/4$ Fresnel rhomb (FR) and the beam was reflected back by a high reflecting mirror (HR) and made a second pass through the rhomb which rotated its polarization by another 45 deg. Finally, the beam passed through the cell the second time and was completely reflected by the polarizer (GL) in the direction of the third Bethune cell. A second half-wave plate (WP2) rotated the polarization plane back to the vertical direction.

Characteristics of PDA

The pulsed dye amplifier system was operated in two different wavelength ranges. In the first one Kiton Red dye was used for the 899-29 laser and Sulforhodamine 640 (SR640) dye for the Bethune cells. The ring dye laser provided tunable light in the range of 580-650 nm with an average output power of 300 mW at 640 nm. SR640 used in the amplifier chain allowed pulse generation in the range from 605 to 628 nm. The dye concentration was 2.1×10^{-4}, 9.2×10^{-5} and 7.9×10^{-5} moles/liter for the first, second and third dye cell, respectively. The energy output curve measured for these conditions is shown in Fig. 3.7a. The maximum output energy of 29.5 mJ was

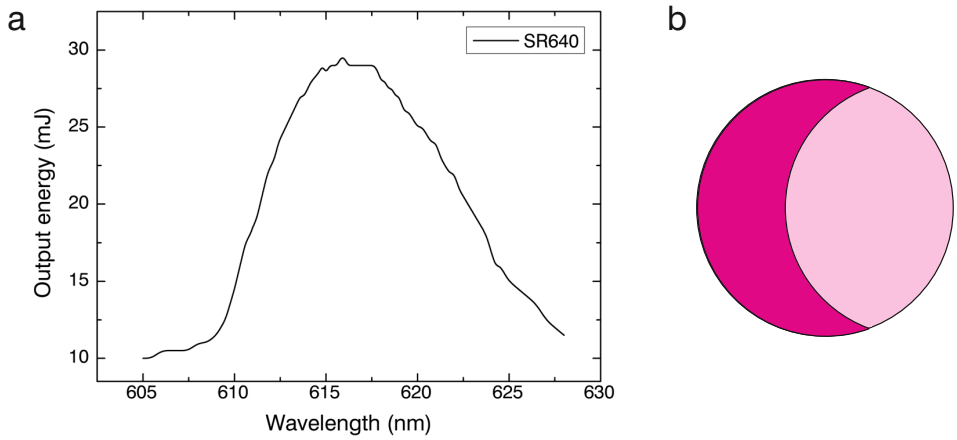

Figure 3.7: (a) Energy output curve of the PDA for Sulforhodamine 640. (b) Schematic view of the PDA output beam profile, where light pink indicates the seed beam profile and dark pink a fraction of the beam, which was pulsed dye amplified.

achieved at 616 nm. The measured portion of the ASE was 33% over the whole tunable range.

In the second tunable wavelength range, suitable for experiments on hydrogen atoms, Pyridine 2 dye was used for the 899-29 laser, providing an average output power of 190 mW at 725 nm. Bethune cells contained Styryl 7 dye at concentrations of 3.8×10^{-4}, 1.3×10^{-4} and 5.6×10^{-5} moles/liter for the first, second and third dye cell, respectively. Due to instability of the 899-29 laser in the case of wavelengths shorter than 725 nm it was impossible to measure the energy output curve as was done for SR640. The maximum output energy of 3.5 mJ was obtained at 729.4 nm. This low output energy could be explained by the moon-like beam profile of the amplified beam (see Fig. 3.7b). This uneven beam profile showed that only approximately 30% of the seed beam was successfully amplified. This may have been caused by micro-damages of the second dye cell that prevented efficient pumping the dye from the top, back and the bottom. The other cause may be reflected fluorescence from the Fresnel rhomb into the dye cell, which led to gain competition between the amplified and the reflected light. Nevertheless, the amplified output beam after being frequency doubled in a KDP (potassium dihydrogen phosphate) crystal ($10\times10\times30$ mm) provided 650 μJ/pulse at 365 nm, which was sufficient to photoionize hydrogen atoms from the $n = 2$ states into quasi-bound Stark states.

3.1.5 Detection of photoelectrons – velocity map imagining (VMI) spectrometer

Proposed more than a decade ago, the velocity map imaging technique, combining a three-plate electrostatic lens with a position-sensitive detector, revolutionized the imaging of ions and electrons resulting from photoionization and photodissociation experiments [114]. By changing the commonly electrode configuration used in imaging techniques, i.e. a positive plate (repeller) and a negative grid, to three plane electrodes, a better image resolution was achieved. Even more importantly all charged particles with the same initial velocity vector, regardless of their original position, were mapped onto the same point in the focal plane. In recent years VMI was successfully implemented in experiments exploring atomic and molecular dynamics on femtosecond [133, 134] and attosecond [135, 136] time-scales, in mass spectroscopy [137, 138], slow photoelectron spectroscopy [139] and for the first time in the observation of holographic structures in atoms [140].

The velocity map imaging spectrometer used in the hydrogen experiments comprised three plates (repeller, extractor and ground) mounted inside a 50 cm flight tube. Each electrode had a diameter of 70 mm and a thickness of 1.25 mm. The spacing between the repeller and extractor was 17 mm, whereas the spacing between the extractor and ground was 30 mm. The repeller plate had a hole of 1.5 mm in diameter, through which hydrogen atoms entered the VMI. The holes in the extractor and ground electrodes had a 20 mm diameter. The advantage of using open electrodes is that the equipotential surfaces are bent and can be adjusted simply by changing the voltage. Thus such an electrode configuration acts as an electrostatic lens enabling to focus the image sharply on the detector. In our VMI the ratio between the repeller and extractor voltages was always 5/4 ensuring that all photoelectrons with the same velocities perpendicular to the flight tube ended up at the same position on the detector. It should be pointed out that the VMI worked perfectly only when the interaction region between the hydrogen atoms and laser lights was exactly in the middle of the repeller and extractor electrodes.

At the other end of the flight tube a position-sensitive detector was mounted, which comprised a set of two MCPs (4 cm in diameter), a phosphor screen (4 cm in diameter) and a CCD camera (F-100 B/C, Pike). When photoelectrons hit the MCPs they ejected electrons, which were subsequently multiplied through the channels of the MCPs. The created shower of electrons reached the phosphor screen causing fluorescence and the produced image was recorded by the CCD camera. Knowing the photoelectron time-of-flight, the camera was triggered allowing efficiently suppression of background signals.

The size of the photoelectron images obtained with the VMI is proportional to the square root of the initial kinetic energy. For example photoelectron images recorded slightly above the saddle point energy for an electric field of 800 V/cm would have a maximum radius of $\sim$100 μm, meaning that it would be impossible to distinguish individual interference rings. Therefore, we used an electrostatic Einzel lens [116], composed of three stainless steel plates with a hole size of 10 mm and spaced by 5 mm plastic separators, which was mounted inside the flight tube approximately

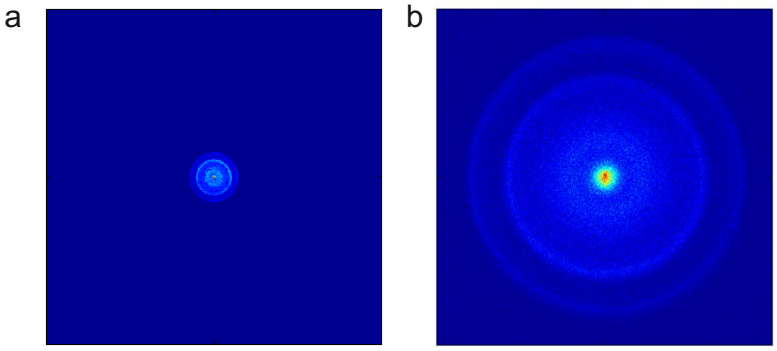

Figure 3.8: Experimental images recorded for photoelectrons with the kinetic energy of 10 meV at an electric field of 170 V/cm (a) without the zoom lens on (voltages at the electrodes: repeller -1.44 kV, extractor -1.16 kV), and (b) with the Einzel lens on (repeller at -1.96 kV, extractor at -1.68 kV and lens at -1.68 kV), allowing magnification of image (a) by a factor of 5. Note that in both images the signal intensities have been normalized: red corresponds to 1 whereas dark blue to 0.

one-third of the way toward the detector (see Fig. 3.1). To ensure that the zoom lens would not change the energy of the photoelectrons the potential before and after the lens had to be the same. This was realized by setting the two outer electrodes at the ground potential. By applying a negative voltage to the central plate photoelectron images were magnified up to 1 order of magnitude without deteriorating the image quality. Fig. 3.8 shows two photoelectron images acquired for the same electric field of 170 V/cm in the interaction region and for photoelectrons with the same initial energy of 10 meV, with the zoom lens off (a) and on (b). By applying -1.68 kV to the lens and adjusting the voltage at the repeller plate for an optimum focusing, the initial image (without the lens) was enlarged by a factor of 5.

In the experiments, photoionization spectra of the hydrogen atom were measured for different electric fields. This was accomplished by scanning the 899-29 laser continuously over a range of 10 GHz (with a speed of 100 MHz/s) with synchronized acquisition of photoelectron images over a small region on the detector (100×100 pixels), where the photoelectrons resulting from the experimental events were expected. Each image was recorded for approximately 20 laser shots. By using an external program the total signal intensity per image was calculated and plotted as a function of the photoionization laser wavelength (e.g. see Fig. 5.4).

3.2 Photoionization microscopy of helium atoms

The field-free ionization potential of helium is almost twice as large as that of hydrogen, i.e. 24.59 eV [141], but unlike the latter it has metastable states, which remain stable in the presence of an external DC electric field. This fact has been used in designing the photoionization microscopy experiments on helium atoms. Namely, an ionization scheme was chosen, where helium atoms are first excited into

the 2^1S metastable state (20.62 eV) by means of a DC electric discharge and then photoionized by absorbing one photon of UV light.

To produce (2^1S) metastable helium atoms a discharge source was designed, which is shown in greater detail in the inset of Fig. 3.9. In the experiments, helium gas was injected via a gas inlet (a) into a quartz tube (b), which surrounded a tantalum needle (c). A negative voltage applied to the needle caused a DC electric discharge between the needle tip and a grounded skimmer (d). Resulting metastable helium atoms were formed in a beam by the skimmer. The He* beam intensity was constantly measured by a Faraday cup (e). A 1 mm $\times$ 300 μm slit in a copper plate (f), which was placed 20 cm after the source chamber, shaped the beam before it entered a velocity map imaging spectrometer (g). Inside the VMI a DC electric field was produced by applying a voltage difference across the electrodes and He* atoms were excited into quasi-bound Stark states by making use of a tunable UV laser with a wavelength in the range of 312–314 nm. UV light was obtained by means of frequency doubling the output of a ring dye laser (899-29, Coherent) with a commercial frequency doubler (WaveTrain, Spectra Physics) providing an average output power of 40 mW. The polarization of the UV light was chosen to be parallel to the electric field enabling the population of $m = 0$ Stark states. The launched photoelectrons were imaged on a position-sensitive detector comprising two MCPs (h), a phosphor screen (i) and a CCD camera (j). Due to low kinetic energies of the photoelectrons it was necessary to magnify the photoelectron images making use of an Einzel lens (k). In order to suppress contributions resulting from Penning ionization of background gas, the velocity map imaging spectrometer was surrounded by a liquid nitrogen cold trap (l). Photoelectron images were obtained by measuring the difference between acquisitions with and without the UV laser.

3.2.1 Metastable helium source

The first metastable helium source combining a corona discharge with a sonic nozzle was proposed by Searcy in 1974 [142]. This device was remarkable for its simple construction as it consisted of a nozzle made of a dielectric material and an ordinary steel sewing needle, which served as the anode. By applying a positive voltage to the anode the corona discharge between the needle and a skimmer was ignited. The discharge was maintained across a pressure gradient and provided a beam flux of 10^{10} metastable helium atoms per second per steradian. The beam was dominated by triplet metastables, as 2^1S metastables rapidly converted to 2^3S by collisions with thermal electrons [143]. One year later Leasure [144] presented a modified source, which increased the beam flux by two orders of magnitude. This was achieved by improving the source geometry, i.e. introducing a glass tube and a floating bias supply. Further modification of the source, made by Fahey [145], resulting in an enhancement of the beam flux to 3.5×10^{14} He* atoms s^{-1} sr^{-1}. In this type of metastable helium source the needle served as the cathode of a low voltage discharge, which was maintained at a negative potential with respect to a grounded skimmer. A slight variation of this device was introduced by Rooijakkers et al. [146], who added liquid nitrogen cooling to reduce the longitudinal velocity of

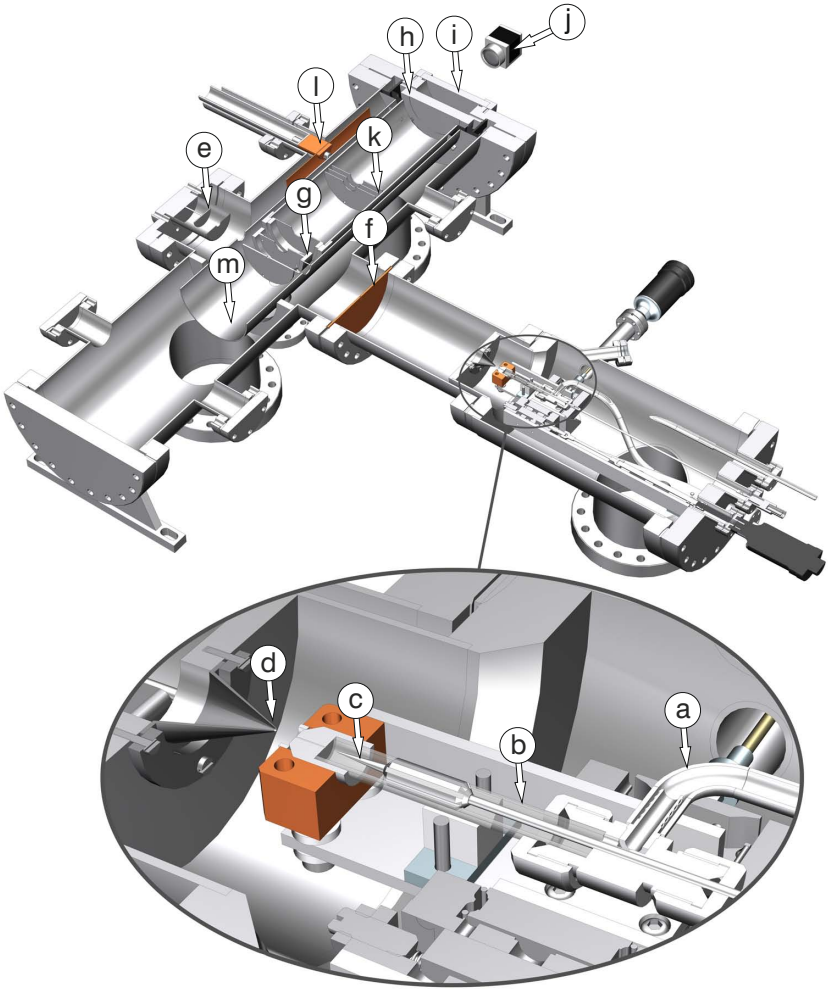

Figure 3.9: Schematics of the experimental setup used in the photoionization microscopy experiments on helium atoms. The inset shows a metastable helium source, where He gas was loaded via an inlet (a) into a quartz tube (b). By applying a negative voltage to the tantalum needle (c) a discharge took place between the needle tip and the grounded skimmer (d) resulting in the production of (2^1S) metastable helium atoms. A He^* beam was shaped by the skimmer and its intensity was monitored by a Faraday cup (e). The beam was further shaped by a slit in a copper plate (f) before it entered a main chamber containing a velocity map imaging spectrometer (g). Inside the VMI He^* atoms were photoionized with UV light and the photoelectrons were projected on a detector comprising two MCPs (h), a phosphor screen (i) and a CCD camera (j). Halfway in the detector flight tube an Einzel lens (k) was mounted. To reduce the effects of Penning ionization, a cold trap (l) was employed and to suppress the Earth magnetic field the spectrometer was surrounded by a μ-metal shield (m).

helium atoms, which was essential in their experiments.

The metastable helium source, used for experiments presented in this thesis, was based on the latter design and its detail scheme is shown in Fig. 3.10 a. A tantalum needle (1) served as the cathode and was located inside a 6 mm diameter quartz tube (2), which was filled with helium gas introduced by a gas inlet (3). Tantalum was chosen due to its high melting point and good thermal conductivity. As a nozzle (4) a piece of boron-nitride (BN) was used because of its softness, workability and poor electrical conductivity. A boron-nitride cup had a 0.25 mm diameter hole, was attached to the quartz tube by using a GE varnish and pressed into a copper block (5), which was cooled with water supplied by bellows. To avoid arcing between the needle and the block (which was grounded) a 2 mm thick ceramic ring (6) was placed on top of the cup. The skimmer (7) was a cone-shape piece made of stainless steel with a 1 mm hole at the apex and kept at a ground potential. The apparatus comprising elements (1)-(6) was mounted on a xyz translation stage, which enabled its precise positioning with respect to the skimmer. Owing to that it was possible to optimize the beam flux, which is dependent on the nozzle - skimmer position. The source was mounted inside a vacuum chamber (shown in Fig. 3.9) that was pumped by a 540 l/s turbo pump, assuring a base pressure of 2.3×10^{-8} Torr (without gas). Helium gas was supplied into the source chamber by a needle valve, which allowed precise adjustment of the gas pressure. Typically, the discharge started for a pressure of 1.5×10^{-4} Torr in the source chamber and after the ignition the pressure was reduced to 6×10^{-5} Torr. The source chamber had two windows through which it was possible to observe the discharge glow by a naked eye (see Fig. 3.10c).

The needle in the source was the cold-cathode type, meaning it was not independently heated and its operation was as follows. By applying a sufficiently high negative voltage to the cathode electrons were emitted by means of field electron emission. These electrons ionized the gas creating ions, which, due to the presence of a negative potential, were accelerated toward the needle. By gaining sufficient energy as a result of the acceleration the ions kicked out electrons from the cathode surface. These secondary electrons sustained the discharge and consequently the voltage could be lowered. Therefore, to ignite and sustain the DC electric discharge in the source two power supplies were used, which were connected in a simple electrical network as shown Fig. 3.10b. When helium gas was loaded a negative voltage of -3 kV was applied to the needle by a high-voltage power supply (0-10 kV, 0-3 mA, Wallis Hivolt). The ignited discharge resulted in a current increase and the current flow across the high-voltage power supply was blocked by a 1 kΩ resistor while a 6 kV diode allowed for it to pass through a high-current power supply (0-1.5 kV, 0-100 mA, Heinzinger), which was set to 700 V. The latter power supply maintained the discharge whereas the former was switched off. The current through the discharge was limited to 20 mA.

The intensity of the metastable helium beam was measured with a Faraday cup. In this simple detector He^* atoms struck a stainless steel target and were de-excited. As the atoms had an internal energy higher than the work function of the stainless steel, secondary electrons were emitted, which induced a current measured with a picoammeter (6487, Keithley). The relation between the current I_- and the beam

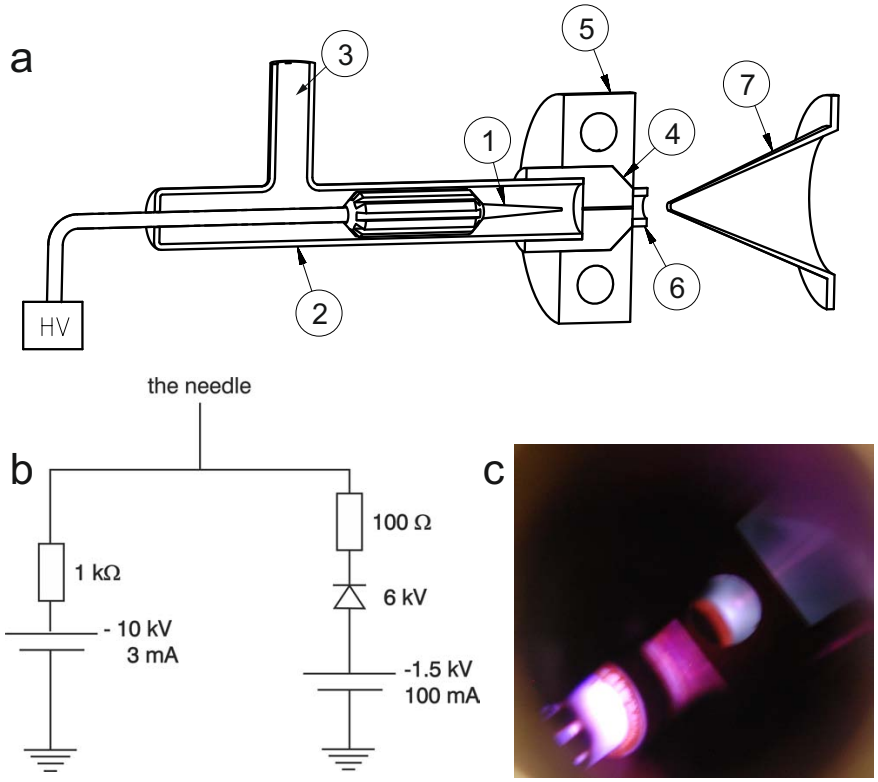

Figure 3.10: (a) Metastable helium source comprising a tantalum needle (1), quartz tube (2), gas inlet (3), boron-nitride nozzle (4), cooling block (5), ceramic ring (6) and skimmer (7). The needle is connected to high-voltage (HV) power supplies. (b) Electrical circuit connecting two power supplies, which deliver high-voltage to initiate and sustain the discharge. (c) View through a window showing the discharge glow between the nozzle and the skimmer.

flux F is given by [147]:

$$I_{-} = e\gamma F \Delta\Omega \tag{3.15}$$

where e is the elementary charge, γ the secondary electron emission coefficient and $\Delta\Omega$ the solid angle (for the experimental geometry $\Delta\Omega = 7.5{\times}10^{-6}$). During the discharge helium atoms were promoted into 2^3S and 2^1S metastable states. However, in the used source design the atomic beam is dominated up to 97% by triplet metastables [146] since singlet metastables rapidly convert to 2^3S due to collisions with thermal electrons. Therefore, we assume that the measured current comes from the impact of triplet metastables. For 2^3S He atoms hitting a stainless steel target γ has a value of 0.69 [148]. Thus the flux was determined to be $2.5{\times}10^{14}$ He (2^3S) atoms per second per steradian at the discharge current of 20 mA. Hence, the intensity of singlet metastables was $7.5{\times}10^{12}$ He (2^1S) atoms s^{-1} sr^{-1}. The

beam intensity increased linearly with the discharge current and slowly decreased with the gas pressure. It was strongly depended on the nozzle-skimmer position in the xy-plane and hardly on the z direction. The source ran stably for many hours of operation without any adjustments.

The design of the metastable source allows operation for gasses different than helium. The source was tested for argon gas, where the discharge was ignited at -1.7 kV and at 2.4 $\times 10^{-3}$ Torr in the source chamber. At a discharge current of 22 mA the beam intensity was 2.8×10^{14} metastable argon atoms s^{-1} sr^{-1}. For neon the discharge started at -2 kV and a dark red discharge glow was observed. However, after few moments the discharge quenched and the beam flux could not been measured.

3.2.2 Photoionization of He (2^1S) atoms with UV light

Inside the VMI metastable helium atoms interacted with tunable UV light, which was obtained by means of frequency doubling cw light provided by the ring dye laser. Kiton Red dye used in the ring dye laser ensured its tunable operation in the range of 610-630 nm with an average output power of 400 mW at 625 nm. Prior being sent into the VMI the laser beam passed through an external ring cavity frequency doubler (WaveTrain, Spectra Physics). This commercial device, designed for single frequency cw pump lasers, guaranteed 10% efficiency for second harmonic generation (SHG).

Frequency doubling of continuous wave laser light

The technology for SHG of cw lasers is substantially different compared to arrangements used for pulsed laser systems. The reason is that the power of the second harmonic is proportional to the square of the fundamental wave power, i.e. in the first approximation:

$$P_2 = cP_1^2, \tag{3.16}$$

where c is the so-called conversion coefficient dependent on e.g. the refractive index, the fundamental light wavelength, phase matching, etc. Usually the output power for cw lasers is about 1 W, which makes it challenging to efficiently generate the second harmonic in a single pass through a nonlinear crystal. Therefore, light should be locked in an external resonator containing a nonlinear crystal. In such a cavity the energy of many round-trips is stored and by constructive superposition the initial light power is increased [149]. The total beam path in the cavity is a multiple of the beam's wavelength to ensure its enhancement. As vibrations are always present the resonator length is actively stabilized by a piezo element driven in a servo loop.

The WaveTrain consisted of a resonator based on the DeltaConcept^{TM}, i.e. comprising a prism mounted on a piezo element, a nonlinear crystal (BBO) and two mirrors. As the main limiting factors for efficient SHG are the losses in the resonator, both the prism and the crystal were cut at Brewster's angle. To fulfill the

phase matching condition, for a maximum conversion efficiency, critical phase matching was used. This method takes advantage of the angle dependence of the refractive index and by tilting the crystal phase matching was achieved. A corrective signal needed for the servo loop was generated exploiting the Pound-Drever method [150]. Namely, the incoming beam first passes through an electro-optic phase modulator, which adds sidebands to the spectrum of the laser line, and then it interferes with the unchanged beam reflected from the cavity. The superposition of both beams provides a radio-frequency modulation signal, which is monitored with a photo-diode. Due to active stabilization the 899-29 laser could be continuously scanned as fast as 10 GHz/s, although in experiments the scanning speed was chosen to be 100 MHz/s.

Photoabsorption cross-sections for resonant and non-resonant transitions

The efficiency of a non-resonant transition from the metastable 2^1S state to the field-free ionization potential $E = 0$ can be calculated by means of the Lambert-Beer law, i.e. $p = n\sigma l$ with p being the photoabsorption probability, n the density of He (2^1S) atoms in the interaction region, σ the absorption cross-section, which for 312.18 nm has a value of 9.7 $\times 10^{18}$ cm^{-2} [151], and l the length of the interaction region. The density of 2^1S metastables can be calculated as:

$$n = \frac{F\Delta\Omega}{A\vartheta}, \tag{3.17}$$

where A is the area of the beam shaped/defined by the slit in the copper ring, i.e. $A = 300$ μm $\times 1$ mm and ϑ is the velocity of the beam, which had an approximate value of 1500 m/s. The density of metastables was 1.3×10^5 He (2^1S) atoms/cm^3. The He beam had a diameter of 1 mm, hence the photoabsorption probability was $p = 1.2\times10^{-13}$. As the average output power of UV light was 40 mW the number of photons per second was 6.3×10^{16}. Thus the expected number of events per second for this non-resonant transition was 7.6×10^3.

A photoabsorption cross-section for a resonant excitation into a Stark state is at least one order of magnitude higher compared to the non-resonant transition. This is clearly demonstrated in Fig. 6.2b, where the calculated photoabsorption spectrum of helium atoms in the electric field of 468 V/cm is shown. Unfortunately, the calculation did not provided exact values of photoabsorption cross-sections, however, based on the signal to noise ratio it is expected that the most intense resonances in the experimental spectrum (Fig. 6.2a) correspond to the situation when almost all hydrogen atoms are ionized giving approximately 10^5 events per second.

3.2.3 Detection of photoelectrons – Penning ionization problem

In the experiments 2^1S metastable helium atoms were photoionized in a DC electric field of 468 V/cm. The laser polarization was chosen to be parallel to the electric field, which resulted in the population of $m = 0$ Stark states. To detect photoelectrons resulting from resonant photoexcitation of Stark states, located at energies between the saddle point energy (E_{sp} = -132.4 cm^{-1}) and the field free ionization potential ($E = 0$), the velocity map spectrometer was used. The VMI comprised three electrodes with dimensions and spacing as given in Section 4.1.5. The flight tube had a length of 33 cm and included an Einzel lens mounted 18 cm from the repeller plate. The lens magnified the photoelectron images by one order of magnitude. A position-sensitive detector comprised MCPs, a phosphor screen and a CCD camera.

The MCPs can be operated at pressures as high as 10^{-5} Torr. Thus, in the original setup design, the He* source was directly connected to the main chamber. Under typical operation conditions, when helium gas was loaded into the source chamber, the pressure in the main chamber was $7{\times}10^{-7}$ Torr. However, the background signal was so high that it was impossible to operate the MCPs. This signal was caused by Penning ionization, i.e. due to collisions of metastable He atoms with residual gas atoms or with themselves resulting in the production of ions and electrons [152]:

$$He^* + A \rightarrow He + A^+ + e^-, \tag{3.18a}$$

$$He^* + He^* \rightarrow He + He^+ + e^- (or\ He_2^+ + e^-). \tag{3.18b}$$

As the process given by Eq. (3.18a) is linearly dependent on the residual gas pressure a liquid nitrogen cold trap was installed in the main chamber. It provided a decrease of the pressure by one order of magnitude. Moreover, a 20 cm buffer chamber was introduced between the source and the main chamber to reduce the number of ions and electrons resulted from the reaction given by Eq. (3.18b). At the connection with the main chamber a copper ring with a 300 μm $\times$ 1 mm hole was used, which also played the role of a gasket. These two elements decreased the base pressure in the interaction region to $4{\times}10^{-9}$ Torr and significant suppression of the background signal was achieved.

Nevertheless, images observed on the detector were not free from background signals. As the metastable helium beam and UV light were continuous it was impossible to trigger the camera. To suppress the background signals the photoelectron images were recorded with and without UV light and the final images were obtained by subtracting both images. Typical acquisition times were 20 minutes per image.

4 Semiclassical interpretation of the interference patterns in the photoionization microscopy experiments of hydrogen atoms

4.1 Introduction

The hydrogen atom is the most abundant chemical element in the universe, which due to its simplicity is the most studied and best known particle, yet still attracting attention of theoretical and experimental scientists [153, 154]. The effect of an electric field on this atom, discovered a hundred years ago, was the first problem successfully treated within the framework of quantum mechanics [62]. Implementation of laser spectroscopy to study hydrogen atoms in DC electric fields brought more information concerning properties of quasi-bound Stark states [70, 75, 81, 155, 156] and boosted theoretical treatments of this subject [89, 157].

The problem of electron motion in a combined Stark + Coulomb potential can also be treated by means of classical mechanics. In a series of famous papers, Kondratovich and Ostrovsky developed a semiclassical theory describing photoionization of the hydrogen atom in a uniform electric field [50, 51, 158, 159]. The advantage of the semiclassical approach is that the Stark effect solved in parabolic coordinates has, in contrast to the quantum mechanical approach, exact analytical solutions, whose interpretation is much more intuitive. For example, the photoionization cross section, calculated in the dipole approximation, is known to be caused by resonance and interference effects. Relative contributions of these phenomena depend on the photoelectron energy E and therefore, the energy range can be divided into characteristic regions. Additionally, in the presence of a uniform electric field far from the atomic core, the photoelectrons move asymptotically and parallel to the field axis. Hence, one can measure the spatial distribution of the photoelectron's density on a plane placed perpendicularly to the field axis. The recorded photocurrent should show interference patterns resulting from the interference among an infinite number of classical trajectories along which the photoelectrons move towards the screen. Furthermore, if the photoionization proceeds from a particular Stark state the measured photocurrent represents the squared wave function describing the electron motion along the ξ coordinate.

Following suggestions of Kondratovich and Ostrovsky [51] an apparatus allowing observation and measurement of photoionization interferences of electrons is drawn schematically in Fig. 4.1. It comprises two plane plates procuring a uniform electric field of strength F, laser light focused halfway between the plates, a beam of neutral

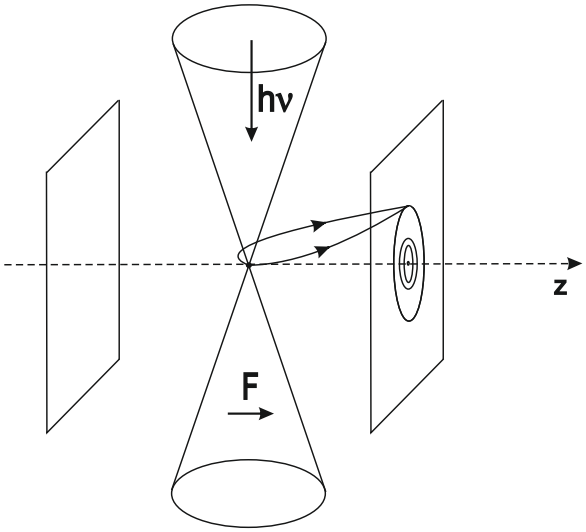

Figure 4.1: Schematic representation of a "photoionization microscope", i.e. an apparatus where atoms are ionized by focused laser light in a presence of a DC electric field, created by two plane plates, and the resulting photoelectrons are projected on a position-sensitive detector, which in this configuration is one of the electrodes. The created interference patters are strongly correlated to the processes occurring in the vicinity of the atom and in special case, when the photoionization proceeds from a Stark state, the observed dark fringes reflect the nodal structure of an electronic wave function.

atoms passing through the focus of the laser and a position-sensitive detector positioned perpendicular to the field axis. The apparatus is called a "photoionization microscope" [49] as electronic wave functions and interference fringes are visible on a microscopic scale.

4.2 Classical theory of the interference phenomenon

The aforementioned interference effect can be exclusively explained by studying the peculiarities of the classical motion of the photoelectrons in the presence of a combined Stark + Coulomb potential. Mathematically this problem becomes equivalent to the description of an artificial satellite motion in a planet's gravitational field with a constant acceleration [160]. Here the gravitational field is an analogy to the Coulomb potential and the acceleration is an analogy to the homogeneous electric field. By introducing a reduced time variable τ, according to the relation $d\tau = dt/r$, the equations of the classical motion for an electron with the total energy E in a DC electric field are given by [158]:

$$\frac{d\xi}{d\tau} = 2\xi\left(\frac{1}{2}E + \frac{Z_1}{\xi} + \frac{p_\phi^2}{4\xi^2} - \frac{1}{4}F\xi\right), \tag{4.1a}$$

$$\frac{d\eta}{d\tau} = 2\eta\left(\frac{1}{2}E + \frac{Z_2}{\eta} + \frac{p_\phi^2}{4\eta^2} + \frac{1}{4}F\eta\right). \tag{4.1b}$$

In these equations p_ϕ is the orbital angular momentum and, as before (see Section 2.2), the separation constants Z_1 and Z_2 are related in the following way: $Z_1+Z_2 = 1$. These equations can be simplified by assuming a plane motion, i.e. ($p_\phi = 0$) as the Coulomb field is the dominant force affecting the photoelectron trajectories at macroscopic distances. The separation constants Z_1 and Z_2 can be associated with an ejection angle β between the initial velocity direction of the photoelectron and the field axis as follows:

$$Z_1 = cos^2(\beta/2), \tag{4.2a}$$

$$Z_2 = sin^2(\beta/2). \tag{4.2b}$$

Integration over the equations of motion gives the parabolic coordinates ξ and η as Jacobi elliptic functions of the reduced time variable τ. General solutions can be found in Ref. [158]. Here only the energy region between the saddle point energy and the field free ionization potential i.e. $E_{sp} \leqslant E \leqslant 0$ is elaborated further as the experimental results presented in this thesis were measured solely in this energy range.

4.2.1 Motion along the ξ coordinate

As previously discussed in Section 2.4 (see Fig. 2.4), the electron motion along the ξ coordinate is periodic in τ and confined in the region of $0 \leqslant \xi \leqslant \xi_{max}$, where

$$\xi_{max} = \frac{|E|}{F}\left[\left(1 + \frac{Z_1}{Z_c}\right)^{1/2} + 1\right], \tag{4.3}$$

with Z_c being the so-called critical separation constant $Z_c = E^2/4F$. The expression for the ξ coordinate of the launched electron in the photoionization process is given by Jacobi elliptic functions:

$$\xi(\tau) = \xi_{max}\left(\frac{sn^2(\varphi|m_\xi)}{m_\xi^{-1} - sn^2(\varphi|m_\xi)}\right), \tag{4.4}$$

with the elliptic modulus and the Jacobi amplitude given by:

$$m_\xi = \frac{1}{2}\left(1 - \frac{1}{\sqrt{1 + Z_1/Z_c}}\right), \tag{4.5a}$$

$$\varphi = \frac{1}{\sqrt{2}}\left(1 + \frac{Z_1}{Z_c}\sqrt{-E}\tau\right). \tag{4.5b}$$

The period of the photoelectron motion along the ξ coordinate is equal to

$$T_\xi = 2\sqrt{2}\mathbb{K}(m_\xi)\left(1 + \frac{Z_1}{Z_c}\right)^{-1/4}(-E)^{-1/2}, \tag{4.6}$$

where $\mathbb{K}(m_\xi)$ is the complete elliptic integral of the first kind.

4.2.2 Motion along the η coordinate

The motion along the η coordinate depends on the angle β with respect to the electric field at which the photoelectron is launched. If β is smaller than the critical angle, i.e.:

$$\beta < \beta_c = 2arcsin\left(\frac{-E}{2\sqrt{F}}\right), \tag{4.7}$$

the electron's motion is bound, even though its energy lies above the saddle point (i.e. $E_{sp} < E < -2\sqrt{Z_2 F}$). This situation corresponds to the case described in Section 2.4 where the electron's energy lies below the top of the potential barrier $V(\eta)$. However, in the latter case the photoelectron also has a nonzero probability to tunnel through the barrier, whereas the classical description does not include any quantum effects.

For $\beta \geqslant \beta_c$ (i.e. $-2\sqrt{Z_2 F} \leqslant E \leqslant 0$) the expression for the time-dependence of the η-coordinate has the form:

$$\eta(\tau) = \eta_+\left(\frac{1 - cn(\Theta|m_\eta)}{sn(\Theta|m_\eta)}\right)^2, \tag{4.8a}$$

$$\eta_+ = \frac{|E|}{F}\left(\frac{Z_2}{Z_c}\right)^{1/2}. \tag{4.8b}$$

Elliptic functions in Eq. (4.8a) contain parameter m_η and argument Θ given as:

$$m_\eta = \frac{1}{2}\left[1 + \left(\frac{Z_c}{Z_2}\right)^{1/2}\right], \tag{4.9a}$$

$$\Theta = \left(1 + \frac{Z_2}{Z_c}\right)^{1/4} \sqrt{-E}\tau. \tag{4.9b}$$

Examination of Eq. (4.8) shows that the photoelectron escapes from the atom to infinity when $sn(\Theta|m_\eta)$ vanishes, i.e. $\Theta = 2\mathbb{K}(m_\eta)$, which corresponds to time:

$$T_\eta = 2\mathbb{K}(m_\eta)\left(1 + \frac{Z_1}{Z_c}\right)^{-1/4} (-E)^{-1/2}. \tag{4.10}$$

4.2.3 Direct and indirect photoelectron trajectories

By placing a position-sensitive detector perpendicular to the electric field one can measure electrons launched during photoionization processes. At any point on the detector, in the classically accessible region, there exist an infinite number of classical trajectories that connect this point with the photoionization region (see Fig. 4.2a). These trajectories can be labeled using the number N of oscillations in the ξ coordinate, i.e. the number of turning points that occur in the trajectory between the atom and the detector. For a given N there exist two trajectories labeled "+"or "-" depending on whether the number of minima along $\xi(\tau)$ is equal to N or $N-1$.

Photoelectron trajectories can be further classified into two categories representing different types of ionization processes. In the so-called "direct" ionization process the photoelectron is ejected downfield towards the hole in the Coulomb + Stark potential. In this situation the photoelectron is launched approximately in the direction of the detector, hence it does not interact with the parent ion and only follows simple trajectories without crossing the z-axis (direct trajectories). During ionization the photoelectron may be ejected up field, i.e. away from the hole in the potential, and it ionizes due to further interactions with the core. In this so-called "indirect" ionization process the photoelectron after being scattered by the core follows more complex trajectories along which it crosses the z-axis at least once (indirect trajectories). Both processes depend on the electric field strength and the energy of photoelectrons. The indirect process dominates for energies close to the saddle point, where direct trajectories are forbidden for any ejection angle β. The onset of direct trajectories corresponds to the situation when $T_\xi = T_\eta$, and it is given by a threshold energy [161]:

$$E_{dir} \approx 0.775 E_{sp}. \tag{4.11}$$

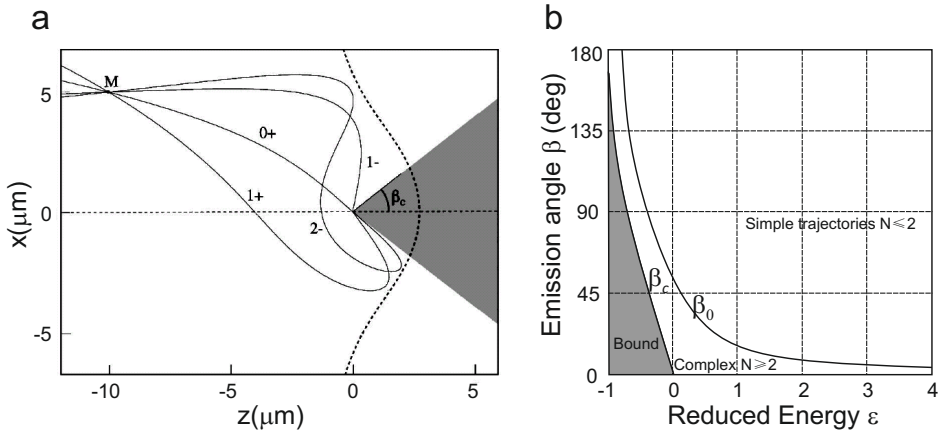

Figure 4.2: (a) Examples of classical trajectories leading to the same point M on a detector placed 10 μm from an atom, which is photoionized in a presence of an electric field F = 1 V/cm and at energy E = -2 cm^{-1}. The thin dashed line indicates the field axis and allows distinguishing the direct trajectories (labeled 0^+ and 1^-), which do not cross the z-axis, from the indirect trajectories (labeled 1^+ and 2^+), which cross the z-axis once. The thick dashed line specifies the classically allowed region (on the left). The gray shaded area shows launched angles smaller than the critical angle β_c, for which the electron motion is bound [162]. (b) Relation between critical angles β_c and β_0 and the reduced energy $\varepsilon = E/|E_{sp}|$. Depending on the ejection angle β the electron motion is bound ($\beta \leqslant \beta_c$), complex ($\beta_c \leqslant \beta \leqslant \beta_0$) or simple ($\beta \geqslant \beta_0$) (figure adopted from Ref. [163]).

Direct and indirect trajectories can also be distinguished by introducing a critical angle β_0 such that the electron launched at angles smaller than β_0 follows a complex motion (indirect ionization), whereas for angles larger than β_0 the electron's motion is simple (direct ionization). Both critical angles β_c and β_0 divide the energy space into three regions as shown in Fig. 4.2b.

4.2.4 Interference patterns – semiclassical wave function

The fact that distinct photoelectron trajectories pass through the same point on the detector leads to the appearance of an interference pattern, which may be observed experimentally. When the photoionization process does not involve resonant excitation into a Stark state the observed patterns can be interpreted exclusively by making use of the semiclassical approximation developed for this problem that considers the phase accumulated by the electron on a way between the atom and the detector [161].

The wave function of a hydrogen atom placed in a DC electric field expressed in parabolic coordinates (see Eq. (2.31)) is a product of functions $\chi_1(\xi)$ and $\chi_2(\eta)$, which satisfy the ordinary differential equations:

$$\left(\frac{d^2\chi_1}{d\xi^2}\right) + \left(\frac{E}{2} + \frac{Z_1}{\xi} - \frac{m^2-1}{4\xi^2} - \frac{F\xi}{4}\right)\chi_1 = 0, \tag{4.12a}$$

$$\left(\frac{d^2\chi_2}{d\eta^2}\right) + \left(\frac{E}{2} + \frac{Z_2}{\eta} - \frac{m^2-1}{4\eta^2} + \frac{F\eta}{4}\right)\chi_2 = 0. \tag{4.12b}$$

Similar to the discussion regarding the classical electron motion, here only the planar motion is further considered i.e. $m = 0$. Hence, modified momenta along both parabolic coordinates have the form [76]:

$$\tilde{p}_\xi = \left(\frac{E}{2} + \frac{Z_1}{\xi} - \frac{F\xi}{4}\right)^{1/2}, \tag{4.13a}$$

$$\tilde{p}_\eta = \left(\frac{E}{2} + \frac{Z_2}{\eta} + \frac{F\eta}{4}\right)^{1/2}. \tag{4.13b}$$

Fig. 4.2a shows only four examples from the infinite number of photoelectron trajectories, which pass via the point $M(\xi_0, \eta_0)$ in the classically accessible region. In the semiclassical approximation the wave function at the point M can be represented as a sum of all trajectories connecting this point with the photoionization region:

$$\psi(M) = \sum_{N=0}^{\infty} X_{N^+} exp(iS_{N^+}) + \sum_{N=1}^{\infty} X_{N^-} exp(iS_{N^-}), \tag{4.14}$$

with $X_{N^\pm}$ being a slowly varying real function depending on the ejection angle β and the angle θ between the x-axis and the plane of trajectory, and $S_{N^\pm}$ being the action along the classical trajectories $N^\pm$. The expression for the total action in terms of modified momenta along the parabolic coordinates ξ and η is given by:

$$S_{N^\pm} = \int_0^{\eta_0} \tilde{p}_\eta(Z_2, E)d\eta + 2N \int_0^{\xi_{max}} \tilde{p}_\xi(Z_1, E)d\xi \pm \int_0^{\xi_0} \tilde{p}_\xi(Z_1, E)d\xi. \tag{4.15}$$

Thus, the total action takes into account the number of complete oscillations of the photoelectron along the ξ coordinate and the accumulated phase from the last axis crossing of the trajectory before reaching the point M. The explicit expressions of the phase integrals can be found in Ref. [50, 89, 90, 107].

Finally, in the laboratory polar coordinates (R, θ) the wave function measured at the point $M(R, \theta)$ on the plane detector can be written as:

$$\psi(M(R,\theta)) = \sum_i [X(\beta_i,\theta)(sin\beta_i d\beta_i)/(RdR)]^{1/2} exp\{i[S_\xi(\beta_i) + S_\eta(\beta_i)]\}, \quad (4.16)$$

where the function $X(\beta_i,\theta) = X_{N^\pm}$ represents the weight of a given classical trajectory, β_i denotes all ejection angles for which photoelectron trajectories are detected at the radius R; $S_\xi(\beta_i)$ and $S_\eta(\beta_i)$ are the phase integrals for the motion along the ξ and η coordinates [161].

The first experimental observation of the interference pattern resulting from interference among various classical trajectories was presented by the group of Blondel in experiments employing a photodetachment microscope [164]. The observed oscillatory patterns were interpreted as interferences between *only* two possible trajectories by which electrons move when ejected from negative ions in a presence of a DC electric field. On the contrary, in photoionization of a neutral atom the launched electron experiences a combined DC + Coulomb potential, where the latter cannot be neglected and leads to existence of an infinite number of photoelectron trajectories. These interference patterns were first observed by photoionizing metastable $(6s[3/2]_{J=2})$ Xe atoms and also first revealed the presence of direct and indirect trajectories [162, 165]. The observed photoelectron density distributions were in good agreement with calculations based on the semiclassical theory described above.

4.3 Experimental results and discussion

In this section the aforementioned interference effects will be illustrated by presenting a series of new experimental results, which were obtained by performing photoionization microscopy experiments on hydrogen atoms. A detailed description of these experiments is given in Chapter 3 and here only the general concept is explained.

In the experiments a beam of atomic hydrogen was produced by photodissociating H_2S gas making use of 213 nm light delivered by a Nd:YAG laser. The atomic beam was formed by a skimmer separating a source vacuum chamber from a main vacuum chamber, which contained a velocity map imaging (VMI) spectrometer [114]. The hydrogen atoms entered the VMI through a hole in the repeller plate. In the VMI a DC electric field was imposed by applying a voltage difference across the repeller and extractor electrodes. The hydrogen atoms were excited to a mixture of $n = 2$ s– and p–states by means of a two–photon transition, making use of 243 nm pulses from a tunable dye laser. From there, they were ionized using narrowband, tunable laser light in the range from 365 to 367 nm, obtained from a Fourier-limited, home-built pulsed dye amplifier. At this step the emphasis was on ionization processes resulting from the excitation into a continuum of Stark states in the energy region between the saddle point energy E_{sp} and the field free ionization potential ($E = 0$). The polarization of the 243 nm laser was chosen to be perpendicular to the static electric field (i.e. parallel to the two-dimensional detector), whereas the polarization of the 365-367 nm laser was parallel or perpendicular to the static electric field. The

resulting photoelectrons were projected onto a position sensitive detector comprising a stack of two microchannel plates, a phosphor screen and a CCD camera. In order to distinguish individual interference fringes in the recorded photoelectron images, an electrostatic zoom lens was used [116], which magnified the images by one order of magnitude without deteriorating their quality.

4.3.1 Semiclassical interpretation of the interference patterns

In the experiments on hydrogen atoms distinct interference patterns were investigated for different values of the electric field ranging from 200 to 850 V/cm and for the photoionization laser polarization chosen to be parallel (π–polarized) or perpendicular (σ–polarized) to the field axis. Observed patterns were independent of the laser polarization, as shown in Fig. 4.3, where two images recorded for the photoelectrons excited 10 cm^{-1} above the field-free ionization limit with π–polarized (a) and σ–polarized (b) laser light are compared. From these experimental images the radial probability distributions, defined as $P_{exp}(R) = R \int P(R,\theta) d\theta$, where $P(R,\theta)$ denotes the intensity distribution in polar coordinates R and θ, are extracted and compared in Fig. 4.3c. Regardless the laser polarization the same number of fringes is observed and the interference patterns are similar. The inner part of the image, i.e. for the image radius $0 < R \leqslant 4$ mm, is dominated by direct trajectories whereas in the outer part ($4 < R \leqslant 5.3$ mm) the indirect trajectories are noticeable. The classical photoelectron trajectories are described in detail in the next section. Note that the radial distribution for the π–polarization (black line) corresponds to the photoelectron image acquired for 25000 laser shots whereas in the case of the σ–polarization (gray line) the image was recorded only for 10000 events. Therefore, in the former case the signal to noise ratio is better and the interference fringes are more conspicuous.

All photoelectron images discussed in this chapter resulted from photoexcitation of hydrogen atoms into the continuum of Stark states. Recorded images showed a smooth evolution of interference patterns with the increasing excess energy, confirming the lack of resonance effects. Therefore, observed oscillatory structures can be explained exclusively as a result of constructive and deconstructive interferences between classical photoelectron trajectories. To validate this interpretation experimentally measured radial probability distributions $P_{exp}(R)$ were compared with calculated ones, by means of the semiclassical theory developed in Ref. [161], where radial probability distributions were defined as $P_{calc}(R) = R \int |\psi(M(R,\theta))|^2 d\theta$, with $\psi(M(R,\theta))$ given by Eq. (4.16). The left column in Fig. 4.4 shows four photoelectron images recorded by making use of σ-polarized laser light and setting the electric field in the interaction region to 822 V/cm. The signal intensity was normalized per image: red corresponds to the highest intensity whereas black corresponds to the lowest signal intensity. In the right column the experimental radial probability distributions (solid lines) are compared with the results of semiclassical calculations (dashed lines) for a given value of the reduced energy $\varepsilon = E/|E_{sp}|$, where $E_{sp} = 175.4$ cm^{-1}. The calculated distributions were scaled radially to get the best fit with the experimental result at ε = -0.825. Even though experimentally observed fringes for $R < 0.5$ mm

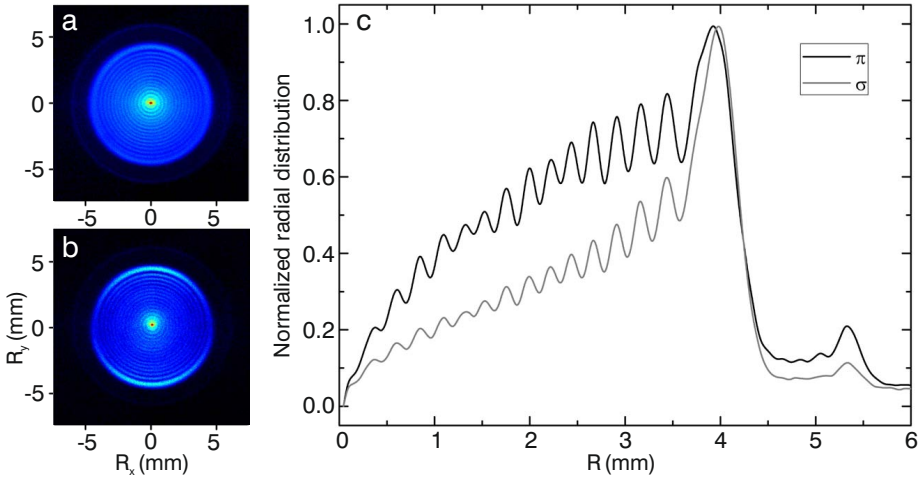

Figure 4.3: Raw photoelectron images resulting from the excitation of electrons 10 cm^{-1} above the field-free ionization limit with the laser polarization chosen to be parallel (a) and perpendicular (b) to the electric field axis. Note that images ware acquired for 25000 and 10000 laser shots for the π–polarized (a) and σ–polarized (b) laser light, respectively. (c) Normalized radial probability distributions extracted from images shown in (a) - black line, and in (b) - gray line. Despite the laser polarization the same interference patterns are observed, which in the inner and outer part of the images corresponds to direct and indirect trajectories, respectively.

are not very well resolved the agreement between $P_{calc}(R)$ and $P_{exp}(R)$ is satisfying, validating the interpretation of the observed oscillatory structures as a result of interferences between the infinite number of classical trajectories by which photoelectrons move towards the detector. Visible singularities in the calculated radial probability distributions (dashed lines in Fig. 4.4) are due to classical singularities (caustics) in the used semiclassical approximation. As shown in Ref. [166] incorporation of the uniform Ariy approximation removes the divergences at caustics and implementation of the Bessel-function approximation fixes the divergent behavior of the wave function near $R = 0$ (apparent in the image for $\varepsilon = -0.797$).

4.3.2 Direct and indirect ionization processes

Fig. 4.5 shows examples of photoelectron images resulting from photoionization of hydrogen atoms in a DC electric field $F = 804$ V/cm. By scanning the laser frequency, atoms were excited into the continuum located in the energy range: $E_{sp} \leqslant E \leqslant 0$. The polarization of the laser was chosen to be parallel to the electric field and each image was recorded for 10000 laser shots. The photoelectron image presented in the top left corner corresponds to the case when the excitation energy was equal to the field-free ionization potential. The subsequent images were recorded by decreasing the excess energy in steps of approximately 5 cm^{-1}. The last image, shown in the

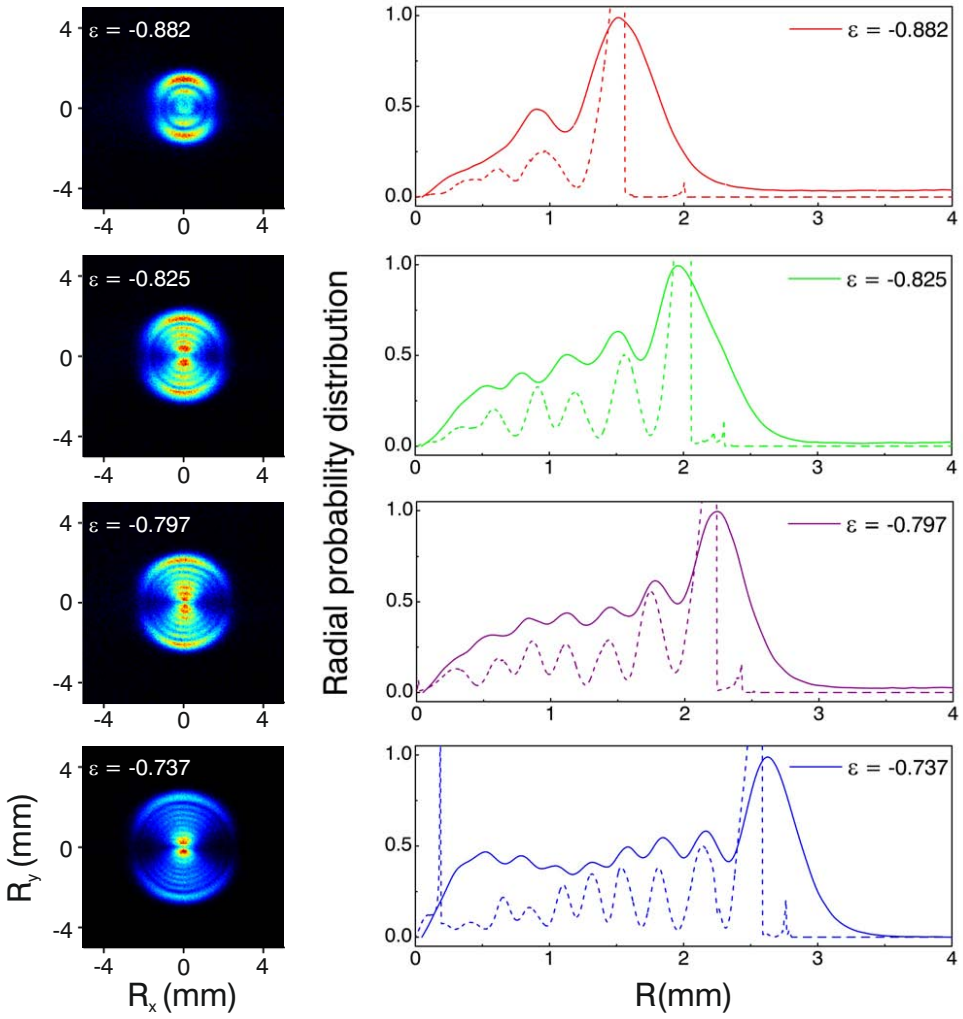

Figure 4.4: The left column shows four photoelectron images recorded for electrons ejected at reduced energies $\varepsilon = -0.882$, $\varepsilon = -0.825$, $\varepsilon = -0.797$ and $\varepsilon = -0.737$. Hydrogen atoms were placed in an electric field $F = 822$ V/cm and the laser polarization was perpendicular to the electric field. In the right column the experimentally measured radial probability distributions $P_{exp}(R)$ (solid lines) are compared with the calculated probability densities $P_{calc}(R)$ (dashed lines) showing a good agreement in the number of fringes. Note that singularities in $P_{calc}(R)$ are due to limitations of the used semiclassical theory.

bottom left corner, was acquired for an excitation energy circa 3.7 cm^{-1} above the saddle point energy, which for the given electric field was located at energy E_{sp} = -173.5 cm^{-1}.

The major observation in Fig. 4.5 is the presence of two distinct concentric struc-

tures, which are clearly visible in the top three rows. The inner structure can be correlated with direct trajectories i.e., with the photoelectrons ejected downfield during the ionization process (direct ionization) and the outer structure with the photoelectrons ejected upfield, which interacted with the parent ion and crossed the field axis at least once (indirect ionization). This is confirmed by the fact that the inner structure becomes visible in photoelectron images recorded at reduced energies: $\varepsilon > -0.777$. This observation agrees well with the classically predicted threshold energy, given by Eq. (4.11), above which direct trajectories are allowed. By analyzing photoelectron images in the bottom two rows one can see that the outer concentric structure, corresponding to the indirect ionization process, dominates in the excess energy region close to the saddle point energy. As shown in Fig. 4.2b, when the reduced energy is smaller than -0.775 E_{sp} the angle β is always smaller than β_0 meaning that photoelectrons have to interact with the parent ion in order to go through a bottleneck in the Coulomb + Stark potential. With increase of the excess energy the opening in the effective potential becomes larger and when $E > E_{dir}$ the opening is large enough for photoelectrons to directly escape through it, i.e. without interaction with the ion. With increase of the photoelectron energy the size of photoelectron images increases and the radius of the outermost ring, built up by indirect trajectories, can be calculated with [161]:

$$R_{max} = \sqrt{2L}\left(\frac{E}{F} + \frac{2}{\sqrt{F}}\right)^{1/2}, \tag{4.17}$$

where L is the distance between the photoionization region and the detector.

Another observation is the appearance of an intense peak in the center of the photoelectron image corresponding to a radius of $R = 0$. If the Coulomb potential is neglected this structure can be built up only with electrons launched at $\beta = 0$ or $\beta = 180°$. However, when the Coulomb force is taken into account there exist many trajectories with $\beta \neq 0$ or $\beta = 180°$ which form this intense and narrow peak at $R = 0$ [163]. Since the number of classical trajectories is proportional to $sin(\beta)$ the peak at $R = 0$ is observable for all energies above the saddle point, though, it becomes especially prominent with the appearance of direct trajectories.

4.3.3 Beating effect

Direct and indirect trajectories differ not only in their origin but they also create distinctively different interference structures. The oscillatory pattern resulting from an indirect ionization process shows smaller spacings between the fringes compared to the structure resulting from direct trajectories (see Fig. 8 in Ref. [161]). Therefore, in the inner part of a photoelectron image direct and indirect oscillatory patterns give rise to a beating pattern, which is visible in the photoelectron images shown in Fig. 4.5. Particularly it is noticeable in the image recorded at ε = -0.287, which is presented in Fig. 4.6a with the experimental radial probability distribution (solid line in (b)). At radii close to the center of the image, i.e. ($R \leqslant 1.5$ mm) the

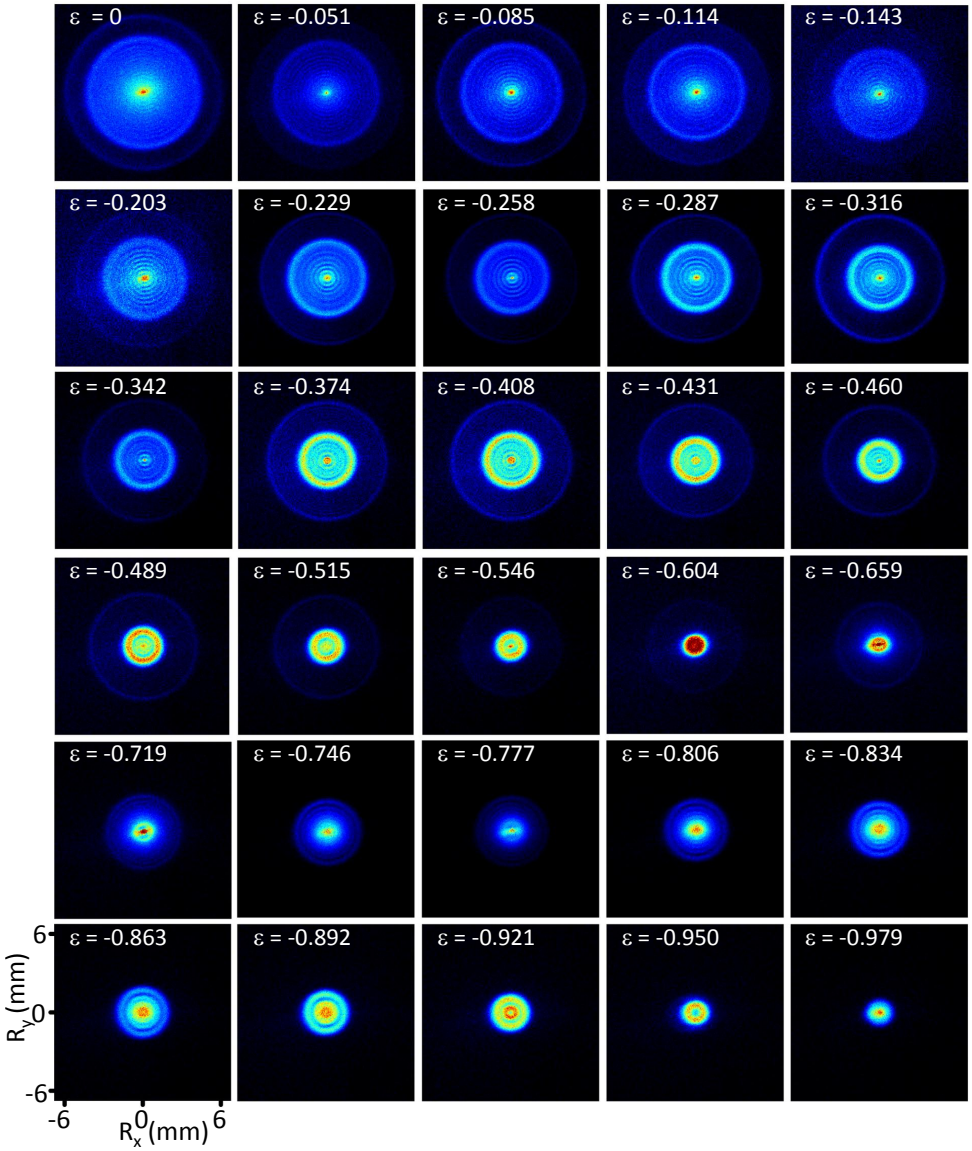

Figure 4.5: Examples of photoelectron images recorded at an electric field of 804 V/cm for different values of the reduced energy ε. The photoelectron energy decreases from the field-free ionization potential (ε = 0 – top left image) to the energy close to the saddle point energy (ε = -0.979 – bottom right image).

interference is enhanced and distinct rings can be distinguished whereas for larger R the two contributions, direct and indirect, partially cancel each other leading to a structureless area. This situation is very well reproduced by the semiclassical

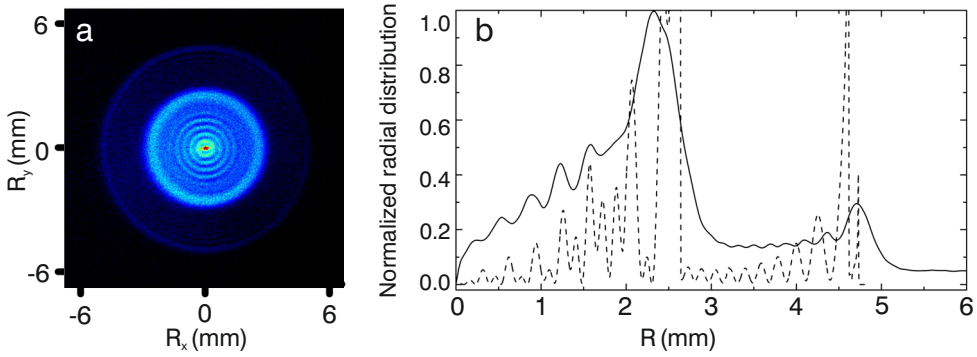

Figure 4.6: (a) Photoelectron image recorded at the scaled energy $\varepsilon = -0.287$ with a conspicuous beating patter, in the inner part of the image, resulting from constructive and deconstructive interferences between direct and indirect photoelectron trajectories. (b) Experimental radial distribution (solid line) indicating a presence of individual ring for $R \leqslant 1.5$ mm and a blurred area for larger R, what agrees well with the semiclassical calculations (dashed line).

calculations (dashed line in (b)), which for $R \leqslant 1.5$ mm demonstrate two groups of fringes: intense ones, which are interleaved with small fringes and consequently dominate the observed interference pattern. For larger R the intensities in both groups of fringes become comparable resulting in a blurred region, where individual rings are indistinguishable.

To investigate the beating effect in detail an experiment was performed where hydrogen atoms were placed in an electric field $F = 796$ V/cm and irradiated with π–polarized laser light. Photoelectron images were recorded in the energy range from -80 to 0 cm^{-1} by changing the excess energy in steps of only 2 cm^{-1} and keeping the exposure time at 10000 laser shots per image. The experimental results are presented in the form of a contourplot shown in Fig. 4.7a, where measured intensity distributions for a given excess energy are plotted as a function of the image radius R. For a better visualization of the beating effect the individual measurements were normalized to the total intensity of the image. Two intense branches, which at energy E = -80 cm^{-1} appear at $R = 1.1$ mm and $R_{max} = 4$ mm and are marked with white dashed lines, correspond to the outer rings created by direct and indirect trajectories, respectively. The most striking observation in this plot is the presence of a sequence of interference structures in the inner part of the photoelectron images, i.e. below the first outer ring where both direct and indirect trajectories interfere. This beating pattern is particularly conspicuous in the energy range from -80 to -40 cm^{-1}, where at least five beating branches can be distinguished with an average spacing between the fringes equal to 4 cm^{-1} , as indicated with a white arrow. These beating structures are very well reproduced by semiclassical calculations shown in Fig. 4.7b. The calculations reveal more branches of beating patterns, which are present in the energy range where direct and indirect trajectories interfere, i.e. $E_{dir} < E$. Most likely limitations in the spatial resolution of the recorded images is the reason why

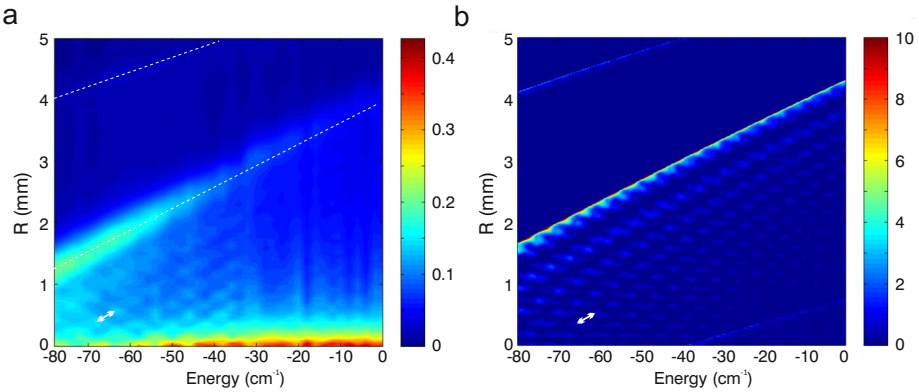

Figure 4.7: Measured (a) and calculated (b) contourplots of the radial intensity distributions in photoelectron images, which resulted from ionization of hydrogen atoms in a F = 796 V/cm DC electric field with π–polarized laser light. White dashed lines in (a) indicates intense branches corresponding to the outermost rings created by direct and indirect trajectories. In both plots the beating patterns created by constructive and deconstructive interference between direct and indirect photoelectron trajectories are visible. The measured and the calculated spacing between the beating fringes are 4 cm^{-1} and 4.3 cm^{-1}, respectively, as marked in white arrows.

only a limited number of beating structures are experimentally observed in the energy range close to E_{dir}. The calculated spatial frequency of the beating fringes is 4.3 cm^{-1}, which agrees very well with the experimentally determined spacing between the patterns. However, the calculations are not free from computational problems, which lead to the appearance an artifact at E = -39 cm^{-1}.

Furthermore, the recorded data show a periodic modulation in the intensity of the outermost ring, which is particularly conspicuous in the energy range between -40 and 0 cm^{-1}. This effect is emphasized in Fig. 4.8 by presenting four photoelectron images (a-d), which were recorded at energies close to each other, and where one can see that the outermost ring is visible only in two images recorded at E = -2 cm^{-1} and E = -6 cm^{-1}. The measured intensities of the outermost rings for different excess energies were normalized to the total intensity per image and are shown in (e) as black squares. To exclude that the observed oscillations are caused by fluctuations in the signal intensity, the total intensity of photoelectron images, normalized to the intensity of the image recorded at E = -32 cm^{-1}, is plotted in (f). One can see that the periodic modulation observed in (e), with an average energy spacing between extrema ΔE = 5.3 cm^{-1}, does not show any correlations with fluctuations in the total signal intensity shown in (f). The semiclassical calculations, partially shown in Fig. 4.7b, reveal a periodic oscillation in the intensity of the outermost ring with an average spacing between two extrema equal to ΔE = 5.2 cm^{-1}, what agrees very well with the experimentally measured value.

At the moment when this thesis is written many semiclassical calculations are running in order to understand the origin of this periodic modulation. One possible

explaination is that the observed intensity modulation may be created as a result of the interaction between the indirect trajectories with the so-called *closed orbits* [167–169]. As explained in Section 3.1, when the ejection angle is smaller than the critical angle β_c the electron stays forever in the vicinity of the atom. These types of photoelectron trajectories are called *bound orbits*, in contrast to *open orbits*, i.e. trajectories along which the electron escapes from the atom. Direct and indirect trajectories are both open orbits. There exists a special set of trajectories belonging to the bound orbits – so-called *closed orbits*, which are related to the occurrence of blue-shifted Stark states [166, 168]. Hence, the classical picture would be that along these trajectories the electron first goes out from the atom and then it is returned back by the electric field. When the electron propagates back towards the atom it starts interfering with outgoing waves and produces oscillations, which can be observed in the absorption spectrum [81, 156, 170]. For $E > 0$ there is only one closed orbit, which is along the electric field, thus oscillations will be visible only for laser light polarized along the electric field axis (π–polarized). One experimental observation which confirms this hypothesis of interference between indirect trajectories and closed orbits is the fact the modulation in the intensity of the outer ring was not observed for σ–polarized laser light. However, this problem requires further theoretical and experimental studies before any conclusions are drawn.

4.4 Resonance effects in photoionization microscopy

In the discussed energy range i.e., $E_{sp} \leqslant E \leqslant 0$, an electron may be resonantly excited into a quasi-bound Stark state. In this situation the electron motion (given by Eq. (4.12)) is always bound along the ξ coordinate and classically bound along the η coordinate, since its energy lies below the top of the $V(\eta)$ potential. However, from a quantum mechanical point of view the electron has a nonzero probability to tunnel through the $V(\eta)$ potential barrier and to escape from the atom. Such a quantum effect may be incorporated into the discussed semiclassical approximation by the Bohr-Sommerfeld quantization condition [50]:

$$\int_{\xi_0}^{\xi_{max}} \tilde{p}_\xi d\xi = \pi\Big[n_1 + \frac{1}{2}\Big(|m| + 1\Big)\Big], \tag{4.18}$$

which relates the separation constant Z_1 with the resonance energy E. With such a condition for a given value of E the separation constant Z_2 can be determined, and thus by integrating Eq. (4.12b) the outgoing wave function can be expressed by [51]:

$$\chi_2(\eta) \approx \frac{1}{2i} C \eta^{-1/4} exp\Big[i\Big(\frac{1}{3}F^{1/2}\eta^{3/2} + \delta\Big)\Big], \tag{4.19}$$

with a constant C and some phase δ . When a position-sensitive detector is placed far enough from the photoionization region the η = const coordinate crossing the

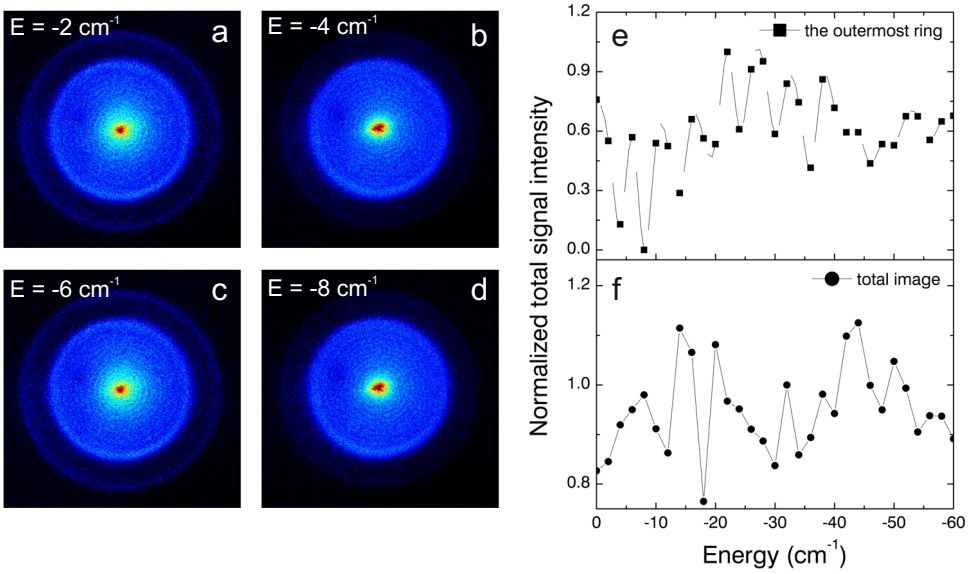

Figure 4.8: (a-d) Photoelectron images recorded in the vicinity of the field free ionization potential, which show the change in the intensity of the outermost ring over a short interval of the excess energy. (e) Periodic oscillation in the intensity of the outermost ring, which is particularly prominent in the energy range from 0 to -40 cm^{-1}. Note that here the intensity of the outermost ring was normalized to the total signal in the image. (f) The total signal intensity of a series of recorded photoelectron images normalized to the intensity of the image recorded at E = -32 cm^{-1}.

plane of the detector can be approximated by a plane surface, which is perpendicular to the z-axis. The component of the photocurrent density perpendicular to the surface $\eta = \text{const}$ is denoted by:

$$j_\eta \approx i\Big(\psi\frac{d\psi^*}{d\eta} - \psi^*\frac{d\psi}{d\eta}\Big), \tag{4.20}$$

where ψ represents the final state electron wave function given by Eq. (2.31). Combination of Eq. (2.31), (4.19) and (4.16) gives the photoelectron current density measured on the detector:

$$j_\eta = \frac{1}{4}|C|^2 F^{1/2}\frac{1}{\xi}|\chi_1(\xi)|^2. \tag{4.21}$$

Thus, when the hydrogen atom is excited into a Stark state prior to being ionized, the observed interference pattern represents the squared modulus of the electronic wave function $\chi_1(\xi)$, which describes the electron motion along the ξ coordinate.

The radius of the resonant interference pattern is given by:

$$R^c_{mac} = \sqrt{2L}\left[\frac{E}{F} + \left(\frac{E^2}{F^2} + \frac{4Z_1}{F}\right)^{1/2}\right]^{1/2}, \tag{4.22}$$

and can be compared with the expression given by Eq. (4.17), which describes the classically allowed region along the ξ coordinate for the non-resonant case. One sees that $R^c_{max} > R_{max}$ meaning that the interference pattern resulting from resonant excitation into a Stark state extends radially further compared to the non-resonant case. Moreover, the positions of the minima in the photoelectron image are given by $R_n = \sqrt{2L\xi_n}$, where ξ_n is the n^{th} zero of the electronic wave function $\chi_1(\xi)$. Hence, the experimentally observed minima are a direct projection of the nodal structure of the electronic wave function along the ξ coordinate. Therefore, photoionization microscopy is a technique, which allows direct observation of the electronic wave function on a microscopic scale.

4.5 Resonance effects in experiments and theory to date

In the first experimental implementation of the photoionization microscopy technique, Xe atoms were used, which were photoionized in a DC electric field of 320 V/cm with one UV photon, revealing the presence of direct and indirect ionization processes [165]. Photoelectron images recorded for resonant excitation to Stark states showed interference patterns, for which the number of dark fringes increased smoothly with the excess energy, hence showing no sign of the transverse component of the electronic wave function. The results were qualitatively explained within the framework of the semiclassical approximation and it was shown that the continuum contribution dominated the interference structure in Xe atoms [161]. In a following paper [162], which treated the experimental results with greater detail, it was suggested that information regarding the localization of the wave function could be extracted from relative intensities between direct and indirect contributions.

In the last few years new semiclassical and quantum mechanical theories on photoionization microscopy were developed. The already mentioned work of Zhao and Delos [166] extended the semiclassical approximation of Bordas [161] by means of Airy-function and Bessel-function approximations and Maslov indices. By using the Bohr-Sommerfeld quantization condition, the tunneling effect into the classically forbidden regions was included. To analyze effects of Stark resonances on spatial interference patterns the authors developed a quantum mechanical theory [171]. In their approach mixed parabolic and semiparabolic coordinates were used, i.e. $\xi = \sqrt{r+z}$ and $\eta = r - z$, and a new expression for the outgoing wave function was derived. By numerically solving the Schrödinger equation for H atoms in an electric field F = 5714 V/cm with energies near and at a resonance, the authors calculated the probability densities shown in Fig. 4.9. The image in the middle corresponds to

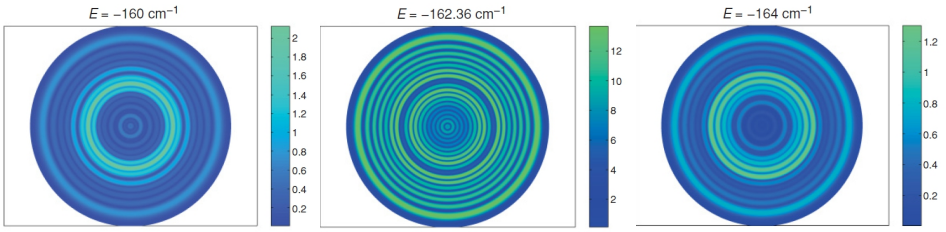

Figure 4.9: Calculated probability densities for H atoms places in an electric field F = 5714 V/cm and excited with π-polarized laser light to three energies: E = -160 and -164 cm^{-1} correspond to non-resonant transitions and show a moderate change in the shape of the interference patterns, whereas E = -162.36 cm^{-1} corresponds to a resonant excitation into a Stark state. In the latter case the shape and the intensity of the interference pattern changes dramatically and the number of dark fringes equals the number of nodes of the electronic wave function $\chi_1(\xi)$ [171].

resonant excitation into a narrow Stark state (n, n_1, n_2, m)=(21, 17, 3, 0) and shows that the total probability distribution is one order of magnitude higher compared to the other non-resonant images. Additionally, the shape of the interference pattern is different – it shows more rings and the number of dark fringes equals the parabolic quantum number n_1, which is the number of nodes of the electronic wave function $\chi_1(\xi)$. On top of that the size of the resonant image is larger than the other two, although this is hardly visible in this figure. The authors showed that the (21, 17, 3, 0) Stark state contributes to the total densities at the other two energies E = -160 and -164 cm^{-1}, however, its contribution is very small compared to the situation at E = -162.36 cm^{-1}. Thus the differences in the spatial distributions of the probability densities at E = -162.36 cm^{-1} are attributed to the presence of the Stark state and are associated with tunneling through the $V(\eta)$ potential barrier. Experimentally the resonance effect was observed in hydrogen [52], helium and lithium atoms [172], with first two cases being further discussed in this thesis (Chapters 5 & 6).

5 Hydrogen atoms under magnification: direct observation of the nodal structure of Stark states

To describe the microscopic properties of matter, quantum mechanics uses wave functions, whose structure and time dependence is governed by the Schrödinger equation. In atoms the charge distributions described by the wave function are rarely observed. The hydrogen atom is unique, since it only has one electron and, in a DC electric field, the Stark Hamiltonian is exactly separable in terms of parabolic coordinates (η, ξ, φ). As a result, the microscopic wave function along the ξ coordinate that exists in the vicinity of the atom, and the projection of the continuum wave function measured at a macroscopic distance share the same nodal structure. In this chapter photoionization microscopy experiments where this nodal structure is directly observed are reported. The experiments provide a validation of theoretical predictions that have been made over the last three decades.

5.1 Introduction

The development of quantum mechanics in the early part of the last century has had a profound influence on the way that scientists understand the world. Central to quantum mechanics is the concept of a wave function that satisfies the time-dependent Schrödinger equation [21]. According to the Copenhagen interpretation, the wave function describes the probability of observing the outcome of measurements on a quantum mechanical system, such as measurements of the energy or the position or momenta of constituents [173]. The Copenhagen interpretation thus allows reconciling the occurrence of nonclassical phenomena on the nano-scale with manifestations and observations made on the macro-scale, which correspond to viewing one of a number of possible realizations allowed for by the wave function.

Despite the overwhelming impact on modern electronics and photonics, understanding quantum mechanics and the many possibilities that it describes continues to be intellectually challenging, and has motivated numerous experiments that illustrate the intriguing predictions contained in the theory [174]. Using ultrafast lasers, Rydberg wave packet experiments have been performed illustrating how coherent superpositions of quantum mechanical stationary states describe electrons that move on periodic orbits around nuclei [175]. The wave function of each of these electronic stationary states is a standing wave, with a nodal pattern that reflects the quantum

numbers of the state. Mapping of atomic and molecular momentum wave functions has been extensively explored by means of (e, 2e) spectroscopy, using coincident detection of the momentum of both an ejected and a scattered electron to retrieve the momentum distribution of the former prior to ionization [28]. In the spirit of scanning tunneling methods, orbital tomography based on high harmonic generation was developed as a method allowing the determination of atomic and molecular orbitals [38, 39]. In this chapter experiments are presented where the nodal structure of electronic wave functions of hydrogen atoms is measured, making use of a photoionization microscopy experiment.

The hydrogen is a unique atom, since it only has one electron and, in a DC electric field, the Stark Hamiltonian is exactly separable in terms of parabolic coordinates. For this reason, an experimental method was proposed about thirty years ago, when it was suggested that experiments ought to be performed projecting low-energy photoelectrons resulting from the ionization of hydrogen atoms onto a position-sensitive two-dimensional detector placed perpendicularly to the static electric field, thereby allowing the experimental measurement of interference patterns directly reflecting the nodal structure of the quasi-bound atomic wave function [49, 51, 158].

5.2 Resonance phenomenon in photoionization microscopy

In a static electric field F the wave function of atomic hydrogen can be separated in terms of the parabolic coordinates (η, ξ, φ) and consequently, the wave function may be written as a product of functions $\chi_1(\xi)$ and $\chi_2(\eta)$ that separately describe the dependence along ξ and η , i.e. $\psi(\eta, \xi, \varphi) = \frac{1}{\sqrt{2\pi\xi\eta}}\chi_1(\xi)\chi_2(\eta)e^{im\varphi}$. The functions $\chi_1(\xi)$ and $\chi_2(\eta)$ satisfy the ordinary differential equations:

$$\frac{d^2\chi_1}{d\xi^2} + \left(\frac{E}{2} + \frac{Z_1}{\xi} - \frac{m^2-1}{4\xi^2} - \frac{1}{4}F\xi\right)\chi_1 = 0, \tag{5.1a}$$

$$\frac{d^2\chi_2}{d\eta^2} + \left(\frac{E}{2} + \frac{Z_2}{\eta} - \frac{m^2-1}{4\eta^2} + \frac{1}{4}F\eta\right)\chi_2 = 0. \tag{5.1b}$$

In these expressions m is the magnetic quantum number and Z_1 and Z_2 are separation constants subject to the condition $Z_1 + Z_2 = 1$. The parabolic quantum numbers n_1 and n_2 are related to the principal quantum number via $n = n_1 + n_2 + |m| + 1$. Functions $\chi_1(\xi)$ and $\chi_2(\eta)$ have n_1 and n_2 nodes along the ξ and η coordinates, respectively. Fig. 5.1a shows the potential energy landscape for the hydrogen atom in an 808 V/cm electric field. The electron motion is always bound in the ξ coordinate whereas the motion along the η coordinate depends on the energy available for its motion. Figures in the bottom panel illustrate the potential energy curves:

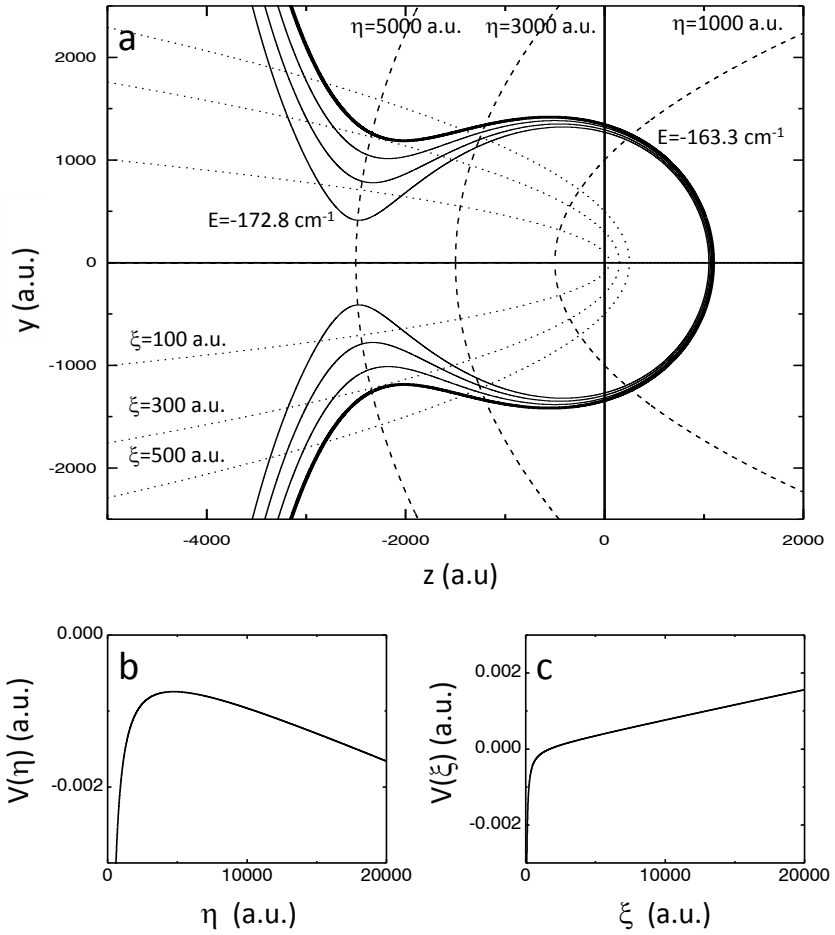

Figure 5.1: (a) Potential energy landscape and relevant coordinate system for hydrogen atom photoionization microscopy in an 808 V/cm electric field. The hydrogen atom sits at the origin of the (z, y) coordinate system and the electric field is along the z-axis (a.u. = atomic units). The boundary between the classically allowed and the classically forbidden region is plotted (solid lines) at the excitation energies of the four measurements that are shown in Fig. 5.3, i.e. ranging from E = -172.8 cm^{-1} to E = -163.3 cm^{-1} (thick outer solid line). Close to the saddle-point, the electron can only escape through a very narrow gap in the Coulomb + dc field potential. The parabolic coordinates $\eta = r - z$ and $\xi = r + z$ are illustrated by plotting a series of contours at constant η (dashed lines) and ξ (dotted lines). The electron motion is always bound in the ξ coordinate whereas the motion along the η coordinate depends on the energy available for the η-motion. (b) and (c) Potential energy curves $V(\eta) = -\frac{Z_2}{2\eta} + \frac{m^2-1}{8\eta^2} - \frac{F\eta}{8}$ and $V(\xi) = -\frac{Z_1}{2\xi} + \frac{m^2-1}{8\xi^2} + \frac{F\xi}{8}$, describing the motion along the η and ξ coordinates [65], where $Z_1 = (n_1 + \frac{|m|+1}{2})/n$ and $Z_2 = (n_2 + \frac{|m|+1}{2})/n$. $V(\eta)$ and $V(\xi)$ are shown for the (n, n_1, n_2, m)=(30, 3, 26, 0) quasi-bound state at E = -163.3 cm^{-1}.

$$V(\eta) = -\frac{Z_2}{2\eta} + \frac{m^2-1}{8\eta^2} - \frac{F\eta}{8}, \tag{5.2a}$$

$$V(\xi) = -\frac{Z_1}{2\xi} + \frac{m^2-1}{8\xi^2} + \frac{F\xi}{8}, \tag{5.2b}$$

defining the motion along the η and ξ coordinates, respectively. Ref. [49] contained a remarkable prediction for the special case where the atomic hydrogen photoionization involves the excitation of quasi-bound Stark states. In this case, where both n_1 and n_2 are good quantum numbers and the electron tunnels through the barrier in the potential energy curve associated with the η coordinate, the measurements should show a total of n_1 dark fringes, directly revealing an important signature of the Stark state involved. However, to date, this experiment was never performed.

Motivated by the theoretical predictions for the configuration of the abovementioned "photoionization microscope" [49], a photodetachment microscope for negative ions was first constructed by Blondel et al. [164]. Their experiments clearly revealed interferences between the photoelectrons en route to the detector, in agreement with simple semiclassical considerations by Du [176]. In photodetachment, the photoelectrons follow one of two possible parabolic trajectories to the two-dimensional detector. By contrast, in a photoionization experiment that starts from a neutral sample, the photoelectrons move in a combined static electric + Coulomb field, significantly complicating the dynamics and leading to the existence of an infinite number of trajectories that the photoelectron can follow to the detector [163].

Given the considerable challenges connected to the experimental use of atomic hydrogen, first attempts to implement photoionization microscopy were performed on Xe atoms by Nicole et al. [165]. Observed interference rings were interpreted in the framework of a semiclassical treatment [161], excluding the possibility of resonant excitation of a Stark state. The experiments themselves were performed both with and without the resonant excitation of quasi-bound Stark states, and no significant differences were observed [162]. More recently, photoionization microscopy experiments were performed for Li atoms [172], revealing first indications of differences in the radial distributions for on- and off-resonance excitation. This work provides the motivation for the hydrogen experiments reported in this chapter, where results for both resonant and non-resonant ionization are presented, and where the long-time predictions of Demkov et al. [49, 158] is convincingly validated.

5.3 Experimental results and discussion

In the experiments an atomic hydrogen beam was formed by collimating hydrogen atoms resulting from the photodissociation of H_2S gas in a first vacuum chamber (see Fig. 5.2 and Chapter 3 for details). The hydrogen atoms were ionized in the active region of a velocity map imaging (VMI) spectrometer [114], where a DC electric field ranging between 250 and 850 V/cm was applied. The atoms were resonantly

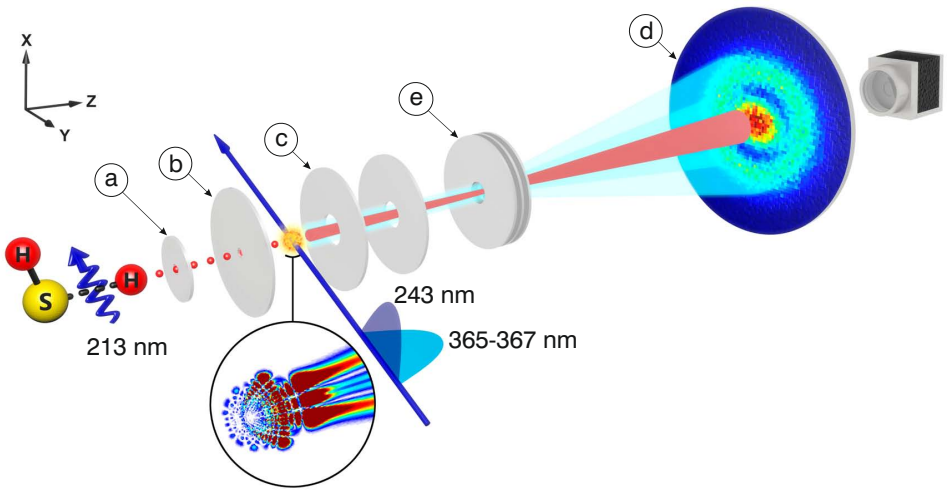

Figure 5.2: Schematic overview of the experiment. An atomic hydrogen beam was formed by photodissociating H_2S and placing a 3 mm aperture (a) 65 mm downstream. In the active region of a velocity map imaging (VMI) spectrometer, the ground state hydrogen atoms were first excited to a mixture of $n = 2$ $s-$ and $p-$states by a two-photon transition using a pulsed 243 nm laser. Next, they were ionized by a Fourier-limited, tunable (365-367 nm), UV laser. By applying a voltage difference across the repeller (b) and extractor (c) electrodes, the photoelectrons were accelerated towards a two-dimensional detector (d), consisting of a set of microchannel plates (MCPs), a phosphor screen and a CCD camera. En route to the MCP detector, the photoelectrons passed through a three-element Einzel lens (e), allowing an increase of the diameter of the recorded image by about one order of magnitude.

excited to a mixture of $n = 2$ $s-$ and $p-$states by a two-photon transition (λ_{laser} = 243 nm) and were ionized using narrowband, tunable laser pulses (λ_{laser} = 365-367 nm, τ_{laser} = 8 ns) from a Fourier-limited, home-built pulsed dye amplifier [130]. The polarization of the 365-367 nm laser was chose to be parallel or perpendicular the static electric field (i.e. $\pi-$polarized or $\sigma-$polarized) to populate $m = 0$ or $m = 1$ Stark states, respectively. A dual micro-channel plate (MCP) detector followed by a phosphor screen and a CCD camera was used to record the photoelectrons. An electrostatic zoom lens magnified the images by about one order of magnitude compared to the size that would have been measured without this lens [116].

5.3.1 $m = 0$ Stark states in high electric fields

In one set of the performed experiments the DC electric field in the interaction region was set to 808 V/cm and the photoionization laser was polarized along the electric field axis ensuring excitation of the $m = 0$ Stark states. The main results of the experiments are shown in Fig. 5.3. In this figure calculated and experimental results are shown for four experiments, where the hydrogen atoms were excited to the

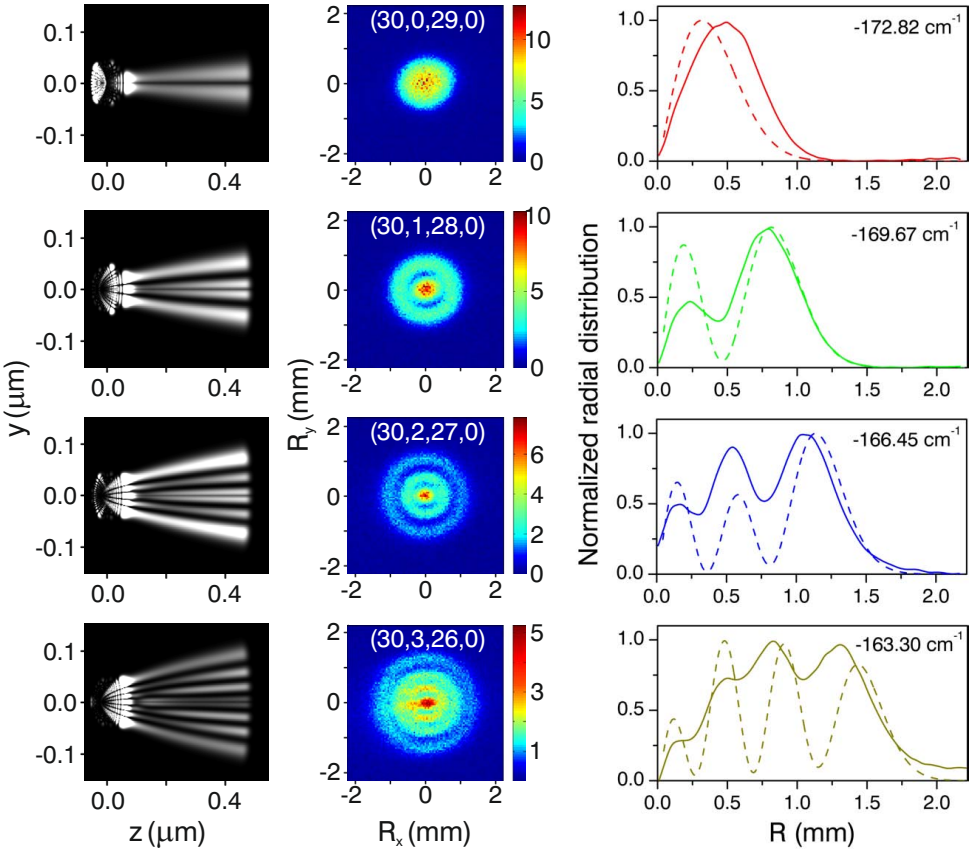

Figure 5.3: Experimental observation of the transverse nodal structure of four atomic hydrogen Stark states. The images in the middle show experimental measurements for $(n,\ n_1,\ n_2,\ m)$*= (30, 0, 29, 0), (30, 1, 28, 0), (30, 2, 27, 0) and (30, 3, 26, 0). Interference patterns are clearly observed where the number of nodes corresponds to the value of* n_1*. The results may be compared to TDSE calculations shown to the left (for details see text), revealing that the experimentally observed nodal structures originate from the transverse nodal structure of the initial state that is formed upon laser excitation. A comparison of the experimentally measured (solid lines) and calculated radial (dashed lines) probability distributions P(R) is shown to the right of the experimental results. In order to make this comparison, the computational results were scaled to the macroscopic dimensions of the experiment. Please note that since,* $P(R) = \int P(R,\alpha)Rd\alpha$*, the radial probability distributions,*$P(R)$ *have a zero at* $R = 0$*, even if the two-dimensional images* $P(R,\alpha)$ *do not.*

$(n,\ n_1,\ n_2,\ m)$= (30, 0, 29, 0), (30, 1, 28, 0), (30, 2, 27, 0) and (30, 3, 26, 0) quasi-bound Stark states. As indicated in Fig. 5.3, the states lie at energies of -172.82 cm^{-1}, -169.67 cm^{-1}, -166.45 cm^{-1} and -163.30 cm^{-1} with respect to the field-free ionization limit, i.e. just above the saddle-point in the Coulomb + DC field poten-

tial, which lies at -174.00 cm^{-1}. According to Eq. (2.35), the validity of which was checked experimentally [177], the ionization rate of these states covered a range from Γ=2.2×10^{10} s^{-1} to Γ=7.25×10^{9} s^{-1}, which (using $\delta E(cm^{-1}) = 5.3 \times 10^{-12}\ \Gamma(s^{-1})$) implies line widths comparable to the effective bandwidth of our excitation laser (0.005 cm^{-1}). These states could readily be identified in wavelength scans, since the ionization is complete before the hydrogen atoms leave the interaction region of the VMI [75]. By contrast, in the same energy range Stark states in the $n = 31$ manifold ($\Gamma > 10^{12}$ s^{-1}) lead to very broad resonances, while states in the $n = 29$ manifold (($\Gamma < 10^{6}$ s^{-1}) undergo insufficient ionization before the atoms fly out of the interaction region. Total ionization spectra as a function of excitation energy in the given static electric field were successfully reproduced by means of the semiclassical Stark theory of Harmin (see [89, 107] and Section 2.5.2). The parabolic quantum number n_1 was identified by comparing the experimental spectra with separate theoretical excitation curves for each n_1-channel. Given the value of n_1, the value of n_2 was subsequently determined by applying the WKB quantization rule along the η coordinate.

The main result of the experiment, which is directly visible in the four images shown in the middle of Fig. 5.3, is the observation of an interference pattern with a number of dark fringes corresponding to the value of n_1. This observation validates the prediction by Demkov and co-workers [8, 9] and illustrates that photoionization microscopy can be used to visualize the nodal structure of $\chi_1(\xi)$ for quasi-bound Stark states of the hydrogen atom. A rationalization for this behavior can be found in the calculations shown to the left of the experimental images. Here, results of propagating the time-dependent Schrödinger equation (TDSE) following excitation of the hydrogen atom at the energies used in the experiments are shown (see [109] and Section 2.5.3). The graphs represent time-integrated plots of the two-dimensional electron density $\rho|\psi(\vec{r},t))|^2$, where $\rho = \sqrt{r^2 - z^2}$, evaluated from the time of excitation ($t = 0$) to a time delay of 600 ps. The nodal structure that is observable at a large distance from the proton (here: 0.4 μm) clearly has its origin in the transverse nodal structure of the initial state that is formed upon laser excitation. The calculation was also carried beyond a distance of 0.4 μm and showed no significant changes.

A direct comparison of the experimental (solid line) and calculated (dashed line) results that is obtained by scaling the radial coordinate in the calculation, is shown to the right of the experimental results. Here a comparison of the measured radial probability distribution $P_{exp}(R) = \int P(R,\alpha)Rd\alpha$ (where $P(R,\alpha)$ represents the intensity distribution in the experimental image in polar coordinates R and α), and the calculated radial probability distribution $P_{calc} = R|\psi(R,t)|^2$ is given, showing very satisfactory agreement and validating the assignment of the number of dark fringes as the parabolic quantum n_1. Observed differences between the experimental and calculated results may be due to differences in the experimental conditions and the assumptions made in the calculations (where the Stark states were excited using a 250 ps excitation pulse), imperfections in the experimental images, and possible smearing effects due to the finite lifetime of the excited Stark states.

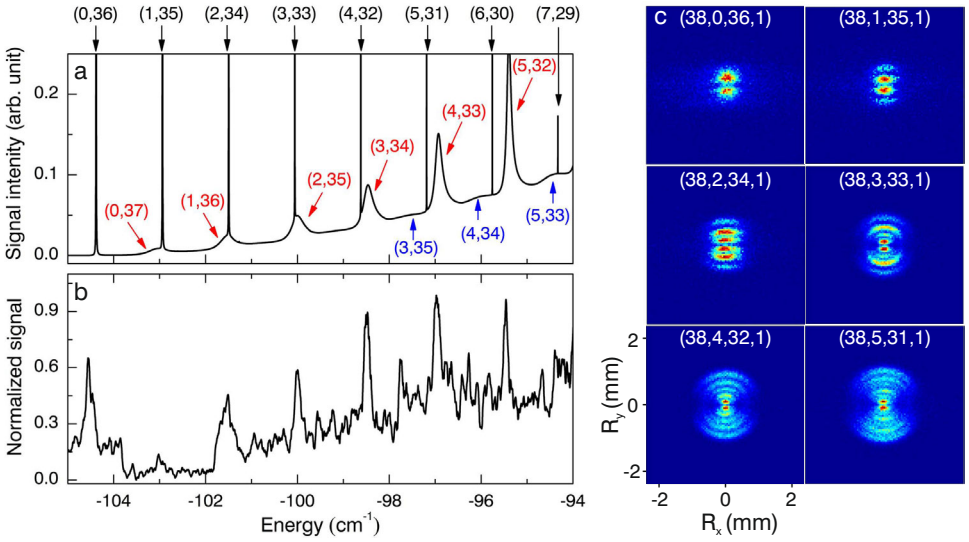

Figure 5.4: (a) Photoionization spectrum for hydrogen atoms ionized in a DC electric field of 295.5 V/cm calculated, by means of Harmin's WKB-QD theory, where resonances associated with quasi-bound Stark states are indicated by arrows. For this plot a different notation of the Stark states is used, i.e. the numbers in the brackets correspond to the parabolic quantum numbers (n_1, n_2) and colors reflect different manifolds: $n = 38$ (black), $n = 39$ (red) and $n = 40$ (blue). (b) An experimental photoionization spectrum in the same energy range as in (a), with prominent resonances originating from photoexcitation of hydrogen atoms into the $n = 38$ Stark manifold. (c) Photoelectron images recorded for quasi-bound Stark states (n, n_1, n_2, m)=(38, 0, 36, 1), (38, 1, 35, 1), (38, 2, 34, 1), (38, 3, 33, 1), (38, 4, 32, 1) and (38, 5, 31, 1), with the number of observed dark fringes equal to the parabolic quantum number n_1, i.e. the number of nodes of the electronic wave function $\chi_1(\xi)$, meaning that the transverse component of the wave function along the ξ coordinate is directly projected on the detector in the experiments.

5.3.2 $m = 1$ Stark states in low electric fields

The transverse component of the electronic wave function $\chi_1(\xi)$ was also observed at lower electric fields as well as in Stark manifolds containing $m = 1$ states, which were populated by making use of σ–polarized laser light, i.e. polarized perpendicular to the electric field axis. The main results of the experiments, where the hydrogen atoms were ionized in a DC electric field of 295.5 V/cm, are shown in Fig. 5.4. In the top panel (a) a calculated, by means of the WKB-QD theory (see Section 2.5.2), photoionization spectrum for the given electric field strength indicates the presence of three overlapping Stark manifolds, i.e. $n = 38$, $n = 39$ and $n = 40$ for excess energies just above the saddle point ($E_{sp} = -105.17$ cm^{-1}). It should be noted that due to a limited energy gap between the resonances a different notation for the Stark states is used in this plot, namely numbers in brackets correspond to the parabolic quantum numbers (n_1, n_2). The experimental photoionization spectrum (b), mea-

sured by scanning the photoexcitation laser frequency, demonstrates prominent resonances in the vicinity of the saddle point energy. However, their number suggests that only one Stark manifold was populated during the experiments due to the aforementioned limitation of the experimental setup. Calculated ionization rates for the reddest states in adjacent manifolds have values of Γ=2.5×10^7 s^{-1}, Γ=1.3×10^{11} s^{-1} and Γ=9.9×10^{12} s^{-1} for the (n, n_1, n_2, m)=(38, 0, 36, 1), (39, 0, 37, 1) and (40, 0, 38, 1) state, respectively, indicating that the observed resonances originated from the excitation of the hydrogen atoms into the $n = 38$ Stark manifold. Therefore, for the resonances lying at energies of -104.55 cm^{-1}, -103.02 cm^{-1}, -101.46 cm^{-1}, -99.95 cm^{-1}, -98.51 cm^{-1} and -96.98 cm^{-1} the following quasi-bound Stark states are assigned: (38, 0, 36, 1), (38, 1, 35, 1), (38, 2, 34, 1), (38, 3, 33, 1), (38, 4, 32, 1) and (38, 5, 31, 1), respectively. The photoelectron images recorded for these states are shown in Fig. 5.4c. The main observation here is that the agreement between the number of observed dark fringes and the parabolic quantum number n_1 is satisfying, which validates the proper assignment of the quantum numbers.

To confirm that the measured oscillatory patterns share the same nodal structure as the electronic wave function $\chi_1(\xi)$ TDSE calculations were performed. The Stark states measured at F = 295.5 V/cm have lifetimes three orders of magnitude longer compared to the Stark states excited at 808 V/cm, hence, the propagation time of the wave packets needed to be extended from 600 ps to 10 ns to ensure a sufficient decay of these states in the calculations. Additionally, the increased stability of the Stark states results in narrower widths of the resonances and consequently, the excitation pulse in the calculations must be long enough to resolve such spectral lines. In Fig. 5.5b the calculated radial distributions using a pulse duration of 250 ps (red dotted line) and 4000 ps (blue dashed line) are compared with the experimentally measured radial distribution (black solid line) of the (38, 3, 33, 1) state, which is shown in the upper panel (a). When the excitation pulse is too short the resonant state is populated along with a fraction of the continuum and as a result the calculated radial distribution contains both resonant and non-resonant contributions, which lead to the appearance of overlapping fringes as shown in the calculations using 250 ps pulses. For a pulse duration of 4000 ps only the resonant contribution is calculated providing a good agreement between the experimental and calculated radial probability distributions. The number of observed dark fringes is identical to n_1, which confirms that the transverse component of the $\chi_1(\xi)$ function is directly observed also in the experiments employing σ–polarized laser light and low electric fields.

As the photoelectron image size scales with $F^{-1/2}$ (see Eq. (4.17) and (4.22)) it is advantageous to use lower electric fields, which ensure larger images and ipso facto higher spatial resolution. Consequently, the electrostatic lens can be operated at lower voltages, which significantly reduces the effects of finite aberrations in the zoom lens and therefore the recorded images appeared to be sharper. This improvement in the image quality is noticeable by comparing the photoelectron images recorded at F = 808 V/cm (Fig. 5.3) with the ones obtained at F = 295.5 V/cm (Fig. 5.4). However, the Stark splitting is linearly proportional to the field strength, hence the electric field cannot be set too low as individual Stark states need to be resolved with the laser

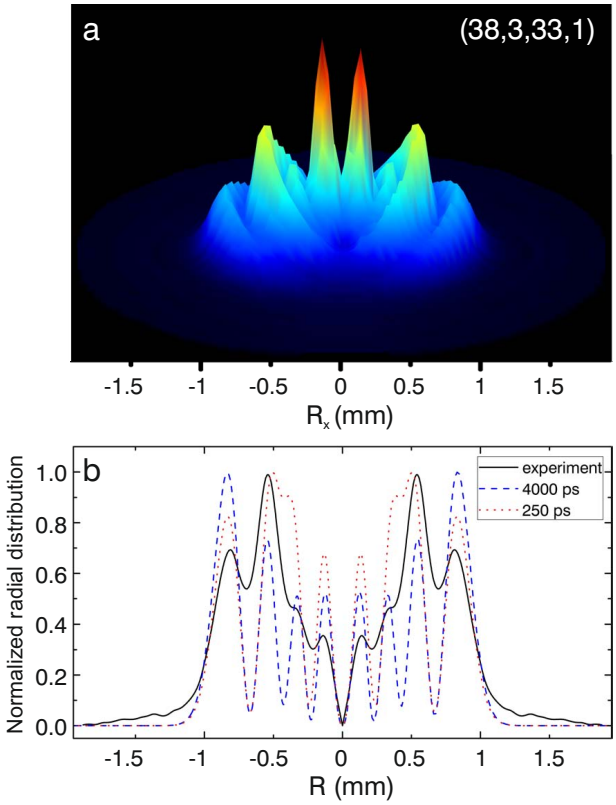

Figure 5.5: (a) 3D representation of the photoelectron image measured for the (38, 3, 33, 1) state obtained by smoothing the raw data with a Legendre fit and plotting the signal intensity as the z-axis. (b) Direct comparison between the measured (black solid line) and calculated (dashed and dotted lines) radial probability distributions for the (38, 3, 33, 1) Stark state. TDSE calculations shown here used a 250 ps (red dotted line) and 4000 ps (blue dashed line) excitation pulse to emphasize that the long lifetime of the Stark state ($\tau = 0.23$ μs) results in a narrow resonance that can be excited along with a fraction of the continuum if the excitation pulse is too short. As a result the calculated radial probability contains both resonant and non-resonant contributions that conceal the wave function of the Stark state and the agreement between the calculation and experiment is diminished. Note that for 250 ps two fringes at $R = 0.5$ mm overlap whereas with the excitation pulse of 4000 ps only the Stark state is populated in the calculations and all fringes are resolved.

bandwidth, which in the experiments was 0.005 cm^{-1}. Furthermore, with a decrease of the electric field the saddle point energy increases and experimentally available quasi-bound states belong to manifolds with high principal quantum numbers, i.e. are located at energies where the density of Stark states is higher and many adjacent manifolds overlap. The latter effect may be troublesome in the calculations and in experiments making use of broad-band laser light.

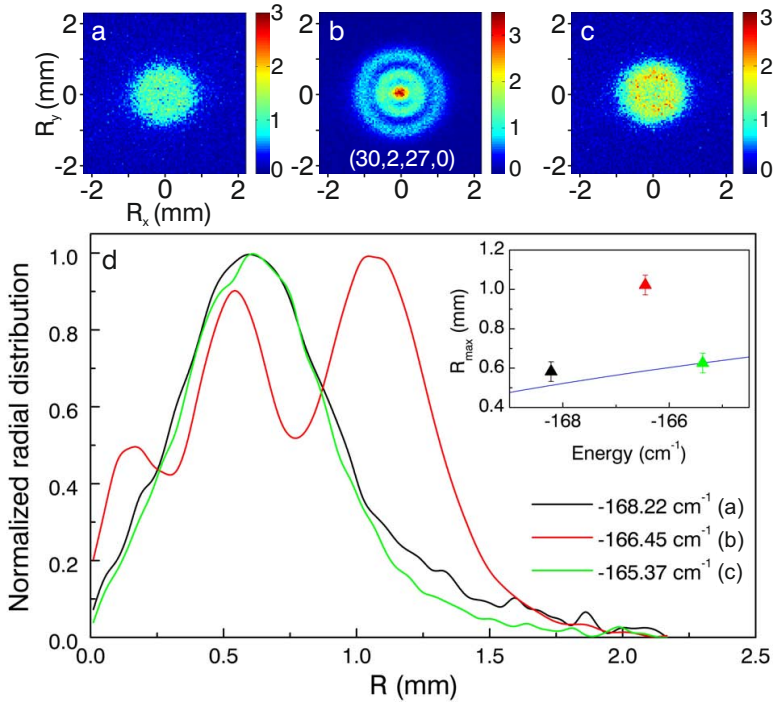

Figure 5.6: Evidence for resonant ionization by tunneling through the Coulomb + DC electric field potential. A comparison is shown between a measurement carried out for the (n, n_1, n_2, m) = (30, 2, 27, 0) resonance (b) and two non-resonant measurements performed 1.8 cm^{-1} below (a) and 1.1 cm^{-1} above (c) this resonance. The normalized radial distribution of the resonant measurement extends significantly further outwards than the non-resonant measurements (d). The inset in (d) shows a comparison of the radial extension of the experimental images, defined as the position of the outer maximum (color triangles) and the theoretical radial extension R_{max} (blue line) according to the classical formula (excluding tunneling contributions) given by Eq. (4.17). The experimental and theoretical radial extensions were matched for the measurement at E = -165.37 cm^{-1}.

5.3.3 Differences between resonant and non-resonant excitations

A striking observation in the experiments is the pronounced difference between images recorded following resonant excitation of a quasi-bound Stark state and images recorded following non-resonant excitation of the ionization continuum. This is illustrated in Fig. 5.6, where a comparison is shown between the image for the (n, n_1, n_2, m)=(30, 2, 27, 0) state and two non-resonant images recorded 1.8 cm^{-1} below and 1.1 cm^{-1} above this resonance. Remarkably, the outermost ring in the resonant image extends significantly further radially than in the two surrounding images. In fact, when comparing the experimental results (color triangles in the inset) to calculations using the classical method used in Ref. [163] (solid blue line), one

sees that the position of the outer ring in the image for the (30, 2, 27, 0) resonance extends further outwards by about 70 %. This is in line with recent theoretical work by Zhao and Delos, who developed both a semiclassical and a quantum mechanical theory for the hydrogen atom photoionization microscopy problem [166, 171]. They predicted a "remarkable tunneling effect" that applies *only* in the case of resonant excitation of quasi-bound Stark states. Classically, the electron is trapped by the potential barrier $V(\eta)$ (see Fig. 5.1b) if the emission angle is smaller than a critical angle $\beta_c = 2arcsin\left(\frac{-E}{2\sqrt{F}}\right)$. However, in case of excitation to a quasi-bound state, electrons with an emission angle smaller than β_c may tunnel through the $V(\eta)$ potential barrier, leading to a situation where the electron can reach a position on the detector that is not classically accessible.

Generally, the image measured at a resonance corresponds to a coherent superposition of resonant and non-resonant contributions, the latter corresponding to direct excitation into the ionization continuum. As a consequence a beating between these two contributions is expected. In the hydrogen measurements that are presented here, the resonant contribution strongly dominates. For example, the signal (i.e. the total number of detected electrons per acquisition) at the (30, 2, 27, 0) resonance in Fig. 5.6 (case b) was stronger than the signal at the adjacent non-resonant positions (cases a and c) by a factor 10. Therefore, the image essentially represents a direct macroscopic projection of the microscopic electronic quantum state. In other atoms electron-electron interactions (as manifested by quantum defects) that couple the initial state ($n,\ n_1,\ n_2,\ m$) to other states have a major influence on the electronic wave that is observed. For example, the above-mentioning tunneling in the η coordinate is largely absent in non-hydrogenic systems, because ($n,\ n_1,\ n_2,\ m$) initial states that require tunneling couple to states that do not. In Xe, the coupling among parabolic states led to a complete disappearance of the resonant effects [165], whereas in Li it led to a substantial reduction of the contrast between resonant and non-resonant excitation [172].

5.4 Summary

In conclusion it was shown that the concept of photoionization microscopy, as theoretically proposed more than 30 years ago and the subject of recent theoretical work predicting the possibility to experimentally observe non-classical photoionization dynamics involving tunneling through the $V(\eta)$ potential barrier, can be experimentally realized, providing both a beautiful demonstration of the intricacies of quantum mechanics and a fruitful playground, where the fundamental implications of this theory can be further explored. For example, predictions have already been made for the case where both electric and magnetic fields are present [178]. The experimental observations of the nodal structures of the wave functions presented in this chapter are not specific to the field strengths and laser excitation conditions (i.e. the polarization direction of the exciting laser) used, but are a general phenomenon that is observable and can be exploited over a wide range of experimental conditions.

6 Visualizing the coupling between red and blue Stark states using photoionization microscopy

In nonhydrogenic atoms placed in a DC electric field, the finite size of the ionic core introduces a coupling between quasi-bound Stark states that leads to the occurrence of avoided crossings between states that otherwise would cross. Near an avoided crossing, the interacting states may have decay amplitudes that cancel each other, leading to a decoupling of one of the states from the ionization continuum. This well-known interference narrowing effect, observed as a strongly electric field-dependent decrease in the ionization rate, has previously been observed in several atoms [87, 88, 94–96]. Here the photoionization microscopy technique is used to visualize the interference narrowing effect, thereby explicitly revealing the mechanism by which Stark states decay. The interference narrowing allows measurements of the nodal patterns of red Stark states, which are otherwise not observable due to their intrinsic short lifetime.

6.1 Introduction

In the previous chapter we have seen that hydrogen atoms placed in an external field are conveniently described using parabolic coordinates (ξ, η, φ), since the Schrödinger equation becomes exactly separable and the Stark wave function can be written as $\psi(\eta, \xi, \varphi) = \frac{1}{\sqrt{2\pi\xi\eta}}\chi_1(\xi)\chi_2(\eta)e^{im\varphi}$. For a given value of the principal quantum number n, the Rydberg states fan out into Stark manifolds that are characterized by parabolic quantum numbers n_1 and n_2. The energy of the Stark states is, to first order in the electric field strength F, given by $E = -\frac{1}{2n^2} + \frac{3}{2}Fn(n_1 - n_2)$. Red Stark states ($n_1 < n_2$) are localized downhill on the Coulomb + DC field potential and display higher ionization rates than blue Stark states ($n_1 > n_2$), where the electron is located uphill. For field strengths $F > 1/3n^5$ adjacent Stark manifolds overlap, and blue and red Stark states cross each other without coupling.

Substantial differences occur in the case of nonhydrogenic atoms, where, due to the finite size of the ionic core, the interaction of the Rydberg electron with the core deviates from being purely Coulombic. In the absence of an electric field, the energy levels of the Rydberg states are now given by a Rydberg-like formula, where the principal quantum number n is replaced by $n^* = n - \delta_l$, where δ_l is the quantum defect [71]. The existence of non-zero quantum defects leads to couplings among the

Stark states. Avoided crossings arise when two Stark states cross each other [68] and Stark states ionize by a process similar to autoionization [84], which significantly decreases the lifetimes of the states. Moreover, the coupling between the blue states and the red continua leads to interferences in the excitation amplitudes and gives rise to asymmetric line shapes resembling Fano profiles [86].

Studies of Stark states around an avoided crossing have included observations of interference narrowing [87, 88, 92, 94–96], i.e. a localized and strongly electric field-dependent increase in the lifetime of some of the Stark states. As explained in Ref. [87]and in Section 2.4.2, this interference narrowing occurs because the matrix element describing the ionization rate can be written as a sum of individual contributions from uncoupled Stark states that may have opposite signs, and that may therefore cancel each other. For example, a two orders of magnitude reduction in the line width of the $(n,\ n_1,\ n_2,\ m)$=(20, 19, 0, 0) Stark state of sodium was observed in Ref. [87].

6.2 Ionization process in hydrogenic and nonhydrogenic

In this chapter, the photoionization microscopy technique [52, 165, 172] is applied to observe changes in the nature of the Stark wave function at a point where a blue and a red Stark state cross, and where interference narrowing occurs. Photoionization microscopy, proposed about thirty years ago [49, 51, 158], predicts that the projection of very slow (typically meV) photoelectrons that are formed by photoionization in the presence of a DC electric field onto a position-sensitive two-dimensional detector would lead to the observation of interference patterns, resulting either from the nodal structure of Stark states prepared in the experiment, or from quantum-mechanical path length differences experienced by the photoelectron along multiple interfering pathways connecting the ionized atom to a particular position on the detector. In a first experimental realization, Nicole and co-workers observed interference patterns for the ionization of xenon atoms in a DC electric field [165], which could be fully explained by the latter mechanism [161]. The same non-resonant effect was observed in hydrogen atoms and is described in detail in Chapter 4. Observation of the nodal structure of quasi-bound Stark states was only accomplished very recently in photoionization microscopy experiments on hydrogen (Ref. [52, 179] and Chapter 5) and lithium [172].

The nature of the ionization process leaves its signature in the interference patterns that can be recorded in a photoionization microscopy experiment. If the ionization of the hydrogen atom takes place from a quasi-bound Stark state, the electron must tunnel through an effective potential along the η coordinate, $V(\eta) = -\frac{Z_2}{2\eta} - \frac{m^2-1}{8\eta^2} + \frac{F\eta}{8}$ (see e.g. Fig. 2.4). This tunneling only affects the electronic wave function $\chi_2(\eta)$, and therefore experimentally observed dark fringes directly reveal the nodal structure of $\chi_1(\xi)$. If the ionization takes place by direct excitation into the continuum (in other words, when the electron is excited above the barrier in $V(\eta)$),

interferences due to semiclassical path length differences along trajectories are observed [161]. A special case arises in nonhydrogenic systems, where the Schrödinger equation is no longer separable in parabolic coordinates, n_1 and n_2 are no longer good quantum numbers and ionization from a quasi-bound Stark state (i.e. a state that is bound in the $V(\eta)$ potential) can occur when the electron is scattered by the core into parabolic states lying above the barrier in the $V(\eta)$ potential. The latter process, similar to autoionization, is the dominant mechanism of field ionization in nonhydrogenic atoms.

6.3 Experimental methods

Here, the case of a singlet state in helium is considered, where $\delta_s = 0.14$, $\delta_p = -0.012$, $\delta_d = 0.002$ and $\delta_{l\geqslant 3} \approx 0$. In the experiments (see Fig. 6.1 and for more detail Chapter 3), metastable helium atoms (2^1S) were generated in a water-cooled source, where a cw discharge was maintained between a Tantalum needle, surrounded by a 6 mm diameter quartz tube filled with He gas, and a grounded, stainless steel skimmer [146]. The intensity of the metastable helium beam was 7.5×10^{12} He^*/sec/steradian. The He^* atoms were photoexcited using the frequency-doubled output of a cw ring dye laser (899-29, Coherent) that was tunable between 625 and 630 nm. Second harmonic generation was accomplished making use of an external ring cavity frequency doubler (WaveTrain, Spectra Physics), which ensured 10% efficiency. The resulting photoelectrons were detected using a velocity map imaging (VMI) spectrometer [114], with a 33 cm flight length and an Einzel lens placed half-way to the two-dimensional detector, which enabled a ten-fold magnification of the images observed on the position-sensitive detector [116]. The detector consisted of a stack of 4 cm diameter microchannel plates (MCPs), followed by a phosphor screen and a CCD camera. To suppress contributions from Penning ionization of background gas, the VMI was surrounded by a LN_2 cold trap, and photoelectron images were recorded by measuring the difference between acquisitions with and without the UV laser.

6.4 Results and discussion

Throughout the experiments the DC field strength was maintained at approximately 468 V/cm and the polarization of the UV laser was set parallel to the DC electric field axis, resulting in the population of $m = 0$ Stark states ($\delta_s = 0.14$). By scanning the dye laser frequency with a simultaneous acquisition of the signal on the detector a photoionization spectrum was acquired, which revealed a large number of quasi-bound Stark states lying between the saddle-point in the Coulomb + DC field potential at an energy $E_{sp} = -2\sqrt{F} = -132.4$ cm^{-1} and the field-free ionization limit ($E = 0$). A part of this spectrum, for excitation energies in the vicinity of the saddle point, is shown in Fig. 6.2a, where distinct Stark states are observed. The hydrogenic quantum numbers (n, n_1, n_2, m) were assigned to most of the spectral lines using the numerical calculations based on Harmin's WKB-QD theory (see

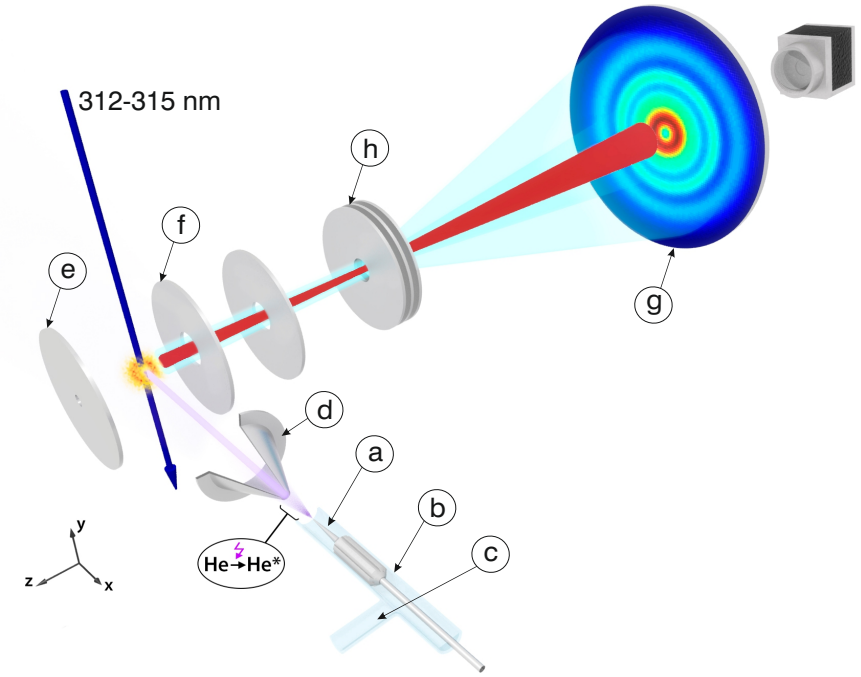

Figure 6.1: Schematic representation of the experimental setup. Metastable (2^1S) helium atoms are created by means of a DC electric discharge maintained between a Tantalum needle (a), surrounded by a quartz tube (b) filled with He gas provided by a gas inlet (c), and a grounded skimmer (d). The ignition starts at -2 kV and is sustained at -0.7 kV and 20 mA. The He beam, formed by the skimmer, crosses a tunable UV laser inside a velocity map imaging spectrometer, permitting the excitation of quasi-bound Stark states that subsequently ionize. By applying a voltage difference across the repeller (e) and extractor (f) plates the photoelectrons are accelerated towards a position-sensitive detector (g) comprising 4 cm diameter MCP plates, a phosphor screen and a CCD camera. Halfway towards the detector, the photoelectrons pass through an Einzel lens (h), enabling magnification of the recorded photoelectron images by one order of magnitude.*

Section 2.5.2). For example the most prominent spectra lines, marked with black arrows, belong to the $n = 28$ Stark manifold and are equally spaced by $E = 1.70$ cm^{-1}. The spectral line at $E = -118.07$ cm^{-1} corresponds to the bluest state in the manifold, i.e. (28, 27, 0, 0), whereas the line at $E = -129.99$ cm^{-1} is identified as the (28, 20, 7, 0) Stark state. The $n = 28$ is one of the lowest (in terms of energy) manifolds observed in the spectrum and due to its high stability the observed spectral lines are intense and very narrow, e.g. the experimental full width at half maximum (FWHM) of the (28, 27, 0, 0) state is 0.0060 ± 0.0003 cm^{-1}. By contrast, the red state (33, 5, 27, 0), marked with a gray arrow, has a width of 0.026 ± 0.002 cm^{-1}, meaning that its lifetime is one order of magnitude shorter than the lifetime of the (28, 27, 0, 0) state. In hydrogen, blue and red states differ in their lifetimes by

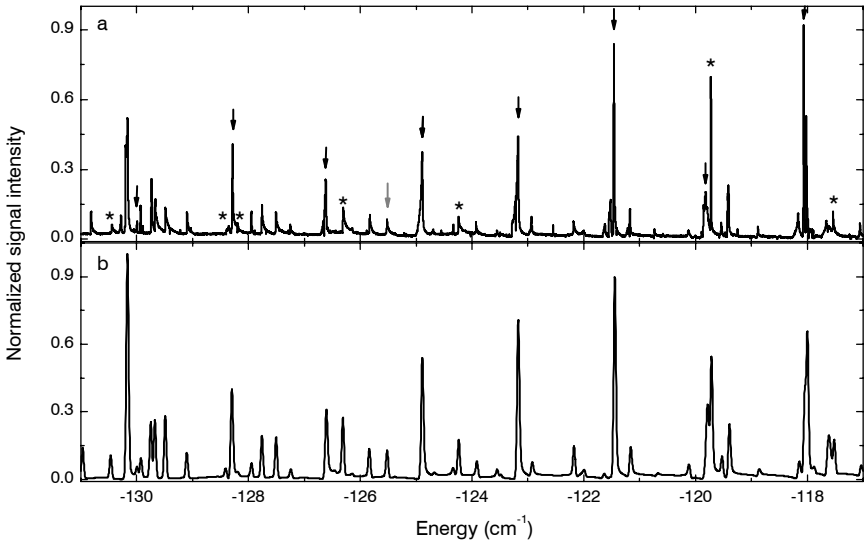

Figure 6.2: (a) Experimental photoionization spectrum of helium atoms placed in a DC electric field of 468 V/cm and ionized in the vicinity of the saddle point ($E_{sp} = -132.4$ cm^{-1}). The numerous quasi-bound Stark states observed here belong to different manifolds ranging from $n = 27$ to $n = 34$. Black arrows indicate intense and narrow spectral lines from the $n = 28$ manifold with the bluest state, i.e. (n, n_1, n_2, m)=(28, 27, 0, 0) at $E = -118.07$ cm^{-1}. A gray arrow points at a red state (33, 5, 27, 0), whose lifetime is one order of magnitude shorter compared to the bluest state in the $n = 28$ manifold. Black asterixes (star symbols) indicate resonances for which the interference narrowing effect was observed. The spectral lines show asymmetric Fano profiles, which are characteristic for autoionization processes. (b) Calculated photoabsorption spectrum, by means of numerical calculations, displaying a very good agreement, in terms of intensity and position, with the experimental spectral lines shown in (a).

many orders of magnitude [75], whereas in helium, or other nonhydrogenic atoms, the blue states are coupled to the red continua and decay much faster. This type of field ionization is a dominant process in nonhydrogenic atoms and it manifests itself by asymmetric profiles of the spectral lines. Such Fano profiles, resulting from constructive and destructive interference between the transition strengths to the mixed discrete-continuum eigenfunctions, are conspicuous in the experimental spectrum.

Fig. 6.2b shows the calculated photoabsorption spectrum for helium atoms in an electric field of 468 V/cm. The photoabsorption cross section was computed by Fourier transforming the correlation function $\langle\psi(t=0)|\psi(t)\rangle$ as implemented in Ref. [98]. This calculation is similar to the wave packet code (see Section 2.5.3) except $\psi(t=0) = z\psi_g$, where $z = rcos(\theta)$ and ψ_g is a ground state wave function. The calculation reproduces very well the experimentally observed spectral lines including their positions and relative intensities. The Fourier transform is performed in all calculations meaning that the calculated line widths are inversely related to the computational time.

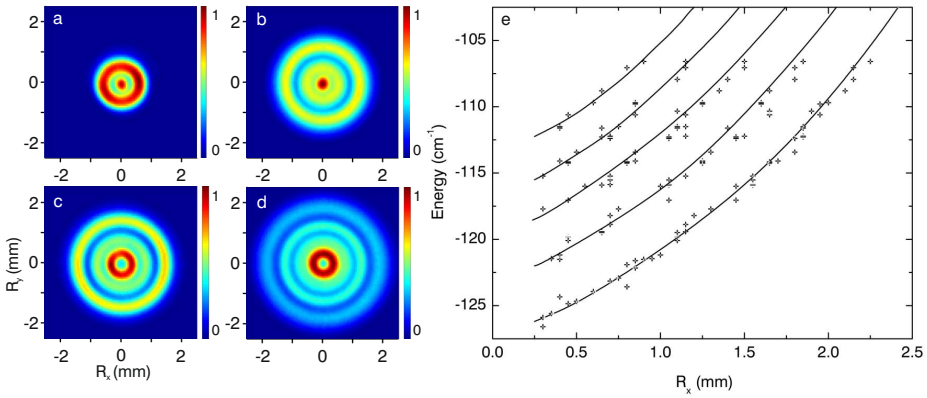

Figure 6.3: Photoelectron images recorded for Stark states that decay via core-induced coupling to fast-ionizing red states. The examples shown in (a)-(d) are the (28, 22, 5, 0), (28, 25, 2, 0), (29, 21, 7, 0) and (21, 23, 5, 0) states, acquired at energies of -126.59 cm^{-1}, -121.46 cm^{-1}, -119.42 cm^{-1} and -115.87 cm^{-1}, respectively, in the presence of a 468 V/cm DC electric field. In all images, the intensities are normalized to the maximum occurring intensity. The main observation is that the number of interference minima increases smoothly as a function of the energy. The interferences can be explained by considering the phase difference between different trajectories by which electrons can move from the ion to the detector. This is further illustrated in (e), where the positions of experimentally observed interference minima (+) are compared with semiclassically calculated positions (solid lines, using the method described in [161]).

6.4.1 Above the $V(\eta)$ barrier ionization of helium atoms

In the experiments photoelectron images were acquired for all Stark resonances in the energy range between the saddle point and E = -75 cm^{-1}, resulting in more than 120 images. The available signal levels did not permit measurements away from the pronounced Stark resonances. In Figure 6.3 (a)-(d), a series of representative images are displayed, revealing the appearance of an interference structure. Images (a)-(d) were recorded for the (28, 22, 5, 0), (28, 25, 2, 0), (29, 21, 7, 0) and (21, 23, 5, 0) Stark states, respectively. However, there is no correlation between a number of nodes and the parabolic quantum number n_1. On the contrary, the number of dark fringes increases smoothly with the photoelectron kinetic energy (defined with respect to the saddle-point). As illustrated in Fig. 6.3e, the energy dependence of this interference structure can be understood semiclassically by considering the phase accumulation along different trajectories that allow the electron to reach the same position on the two-dimensional detector, as discussed in Section 4.2 and in Ref. [161]. In other words these results, which account for about 95% of the images that were recorded, are fully consistent with the results previously reported for xenon in Ref. [165] and for hydrogen in Chapter 4. Consequently, these results will not be further discussed.

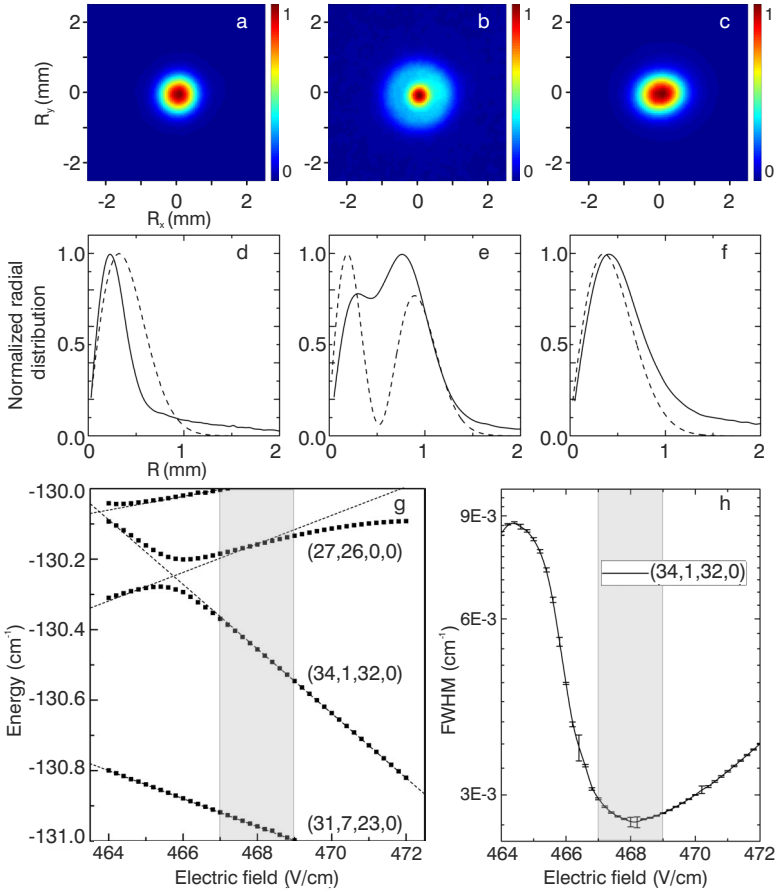

Figure 6.4: (a)-(c) Three raw photoelectron images recorded at energies of -130.95 cm^{-1}, -130.43 cm^{-1} and -130.19 cm^{-1} corresponding to adjacent Stark states identified as (n, n_1, n_2, m)=(31, 7, 23, 0), (34, 1, 32, 0) and (27, 26, 0, 0) respectively. (d)-(f) Comparison between the experimental radial distributions (solid line), extracted from the images in the top panel, and calculated radial distributions (dashed lines) obtained by means of TDSE calculations. The main result is the appearance of a minimum in the radial distribution for the (34, 1, 32, 0) state, which corresponds to the value of n_1 and directly reveals the nodal structure of the $\chi_1(\xi)$ wave function. N.B. The computational results shown here and in Fig. 6.6 were scaled to the dimensions of the experiment in order that the best fit is achieved for the (34, 1, 32, 0) state. (g) Stark map for helium obtained from the calculated photoabsorption cross sections (squares); super-imposed dashed lines schematically indicate the field dependence of the related diabatic, uncoupled Stark states. The gray bar indicating the experimental field strength illustrates that the photoelectron image for the (34, 1, 32, 0) state was recorded in the vicinity of an avoided crossing of this red state with the blue (27, 26, 0, 0) state. (h) Field-dependent reduction in the line width of the (34, 1, 32, 0) state, extracted from the calculated photo-absorption spectra and confirming the occurrence of the interference narrowing effect.

6.4.2 Interference narrowing effects in helium

For eight Stark states the observed nodal pattern differed markedly from the semiclassical predictions. These images were recorded in the vicinity of avoided crossings between red and blue Stark states, and reveal the nodal structure along the ξ coordinate of the red Stark states involved. To illustrate this, Fig. 6.4 (a)-(f) show raw images and extracted radial distributions for three measurements performed at energies just above the saddle-point, involving the (31, 7, 23, 0), (34, 1, 32, 0) and (27, 26, 0, 0) states. The (34, 1, 32, 0) state is an extreme red Stark state, whereas the other two states are a state in the middle of the Stark manifold and an extreme blue state. Remarkably, the radial distribution of the red (34, 1, 32, 0) state extends further than that of the two adjacent states, and – unlike the adjacent images – has a minimum. Both of these observations point towards hydrogenic behavior [52]. The observed minimum in the radial distribution reflects the value of the parabolic quantum number n_1, which describes the nodes of the electronic wave function $\chi_1(\xi)$. Furthermore, the increased radial extension of the image reflects the occurrence of a tunneling process, which allows the electron to reach positions on the detector that are not accessible when the electron ionizes by passing over the saddle-point in the Coulomb + DC field potential [166, 171]. This interpretation is further confirmed by comparing the experimental radial distributions shown in Fig. 6.4 (d)-(f) with results from wave packet calculations based on numerical solution of the time-dependent Schrödinger equation (TDSE) [98]. In these calculations, the He^* atoms were ionized using a 1.5 ns long bandwidth-limited laser pulse, and the propagation was continued up to a time delay of 3 ns. To extract a two-dimensional image from the calculations, the flux through a screen placed at a distance of 0.8 μm was evaluated. It was checked that the radial distributions do not change anymore qualitatively beyond this distance. The numerical radial distributions (scaled to the size of the experimentally measured distributions) show satisfactory agreement and reproduce the essential features of the experiment, i.e. the occurrence of a minimum in the radial distribution for the (34, 1, 32, 0) state and the larger radial extension of this image.

From the calculated photoabsorption cross sections for helium in different energy and field ranges Stark maps were obtained by reading off local maxima in the computed absorption strength as a function of laser wavelength. The Stark map shown in Fig. 6.4g reveals that the measurement for the (34, 1, 32, 0) state was performed in the vicinity of an avoided crossing with the (27, 26, 0, 0) state. The approximate hydrogenic assignments of the diabatic, uncoupled Stark states indicated in Fig. 6.4g were obtained by exploiting the similarities between the calculated Stark map and a hydrogenic calculation (using the formulas given in Section 2.5.1). Monitoring the line widths of the Stark states in the photoabsorption spectra (by fitting a Lorentz profile to the observed resonances), it was discovered that the condition under which the experiment for the (34, 1, 32, 0) state was performed, coincided with a minimum in the line width of this state (Fig. 6.4h). In other words, the observation of the nodal pattern of the (34, 1, 32, 0) state was made possible by a lifetime enhancement (i.e. interference narrowing) of this state, due to the coupling of this state with the blue

(27, 26, 0, 0) state near a field strength of 468 V/cm.

Fig. 6.5a presents the calculated photoabsorption spectra in the vicinity of the avoided crossing between the (34, 1, 32, 0) and (27, 26, 0, 0) Stark states. The spectra were calculated by increasing the electric field from 464 V/cm (top line) in steps of 0.2 V/cm till 468 V/cm (bottom line). The narrowing effect is admittedly visible here, but it is not very apparent since in this particular case the line-narrowing occurs over a wide range of the electric field with a minimum width at 468 V/cm, as shown in Fig. 6.4h. Nevertheless, the main observation here is the disappearance of the oscillator strength of one of the interfering components at about 466.6 V/cm. The same effect was observed experimentally by McNichol et al. in sodium [92] and was explained as interference between the dipole transition matrix elements. Thus it is an analogues effect to the line-narrowing effect, but the cancelation in the amplitude is for other process, which in this case is an electric dipole transition [93, 180]. The energy-field region where this effect occurs, marked with a box, is shown in 6.5b in greater detail. Closer examination of this figure shows that the asymmetry of the line shape is reversed when the electric field changes from 466.4 to 466.6 V/cm. As stated at the beginning of this chapter and in Section 2.4.2, the spectral lines of nonhydrogenic atoms resemble Fano profiles that are characterized by the line shape parameter q, which is proportional to the ratio of the transition amplitude to a bound state and the amplitude of the direct photoionization (to the continuum) [86]. The q reversal observed in 6.5b indicates a sign change of the transition amplitude related to the direct ionization amplitude as shown in Ref. [92]. By that very fact the conditions for the interference narrowing effect to occur are created, i.e. the interfering states have transition amplitudes of opposite signs that can cancel each other leading to a decoupling of one of the interfering states from the continuum. Indeed, the experimental photoionization spectrum (shown in Fig. 6.2a) revealed that the states, where the line-narrowing effect was observed, showed reversed Fano profiles compared to the states with which they interfered in the vicinity of an avoided crossing.

A very similar reasoning underlies the measurement of seven other photoelectron images, listed in Table 6.1 and marked by black stars in Fig. 6.2a, where the experimentally observed interference patterns disagree with the semiclassical prediction. In each of these cases, an avoided crossing between a red and a blue Stark state can be identified, and the nodal structure observed on the detector was that of the red Stark state involved. Furthermore, all these states showed a strongly field-dependent increase in their lifetimes and the photoionization spectrum revealed a reversal of Fano profiles between the interfering states. Here, only the case of the (35, 5, 29, 0) state is further discussed as this measurement was taken a strongly perturbed region due to the vicinity of another avoided crossing, i.e. between the (31, 13, 17, 0) and (28, 26, 1, 0) states.

In Fig. 6.6a a raw photoelectron image of the (35, 5, 29, 0) state measured at an energy of -119.73 cm^{-1} and an electric field of 467.4 V/cm is presented. The extracted radial probability distribution, shown in (b) as a red line, differs significantly from the radial distributions of the adjacent states, which were measured at E = -119.83 cm^{-1} (black line) and E = -119.42 cm^{-1} (green line). The red line shows

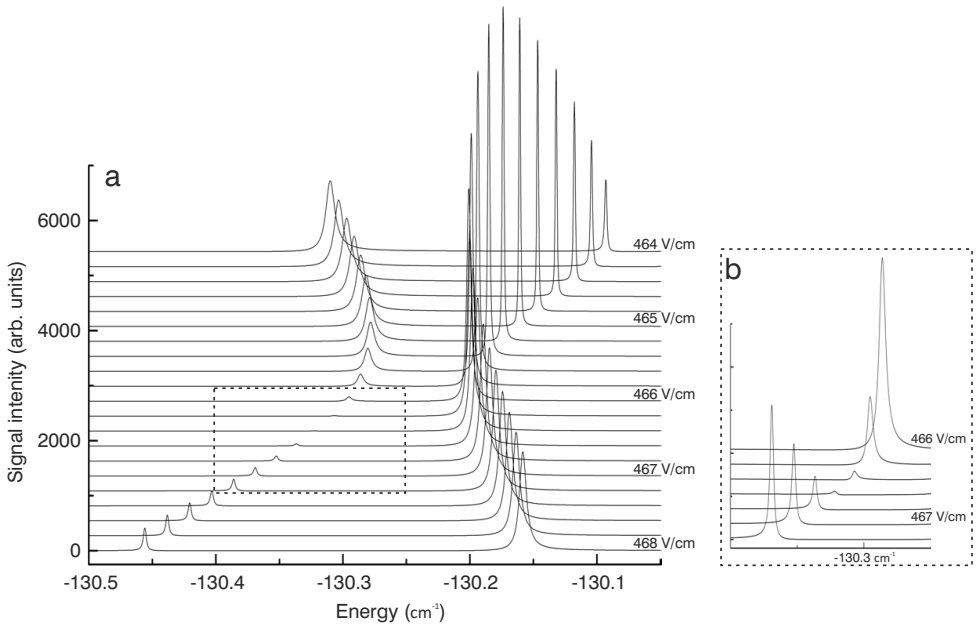

Figure 6.5: (a) Photoabsorption spectra in the region of an avoided crossing between the (34, 1, 32, 0) and (27, 26, 0, 0) states calculated with a step of 0.2 V/cm for an electric field ranging between 464 V/cm (top line) to 468 V/cm (bottom line). The main observation here is the disappearance of the oscillator strength in the line on the left side due to the interference of electric dipole transition matrix elements. (b) Magnification of the region marked with a box in (a), indicating a reversal of the asymmetry of the line shape, resulting from a sign change in the transition amplitude related to the ionization into the continuum.

five minima reflecting the nodes of the electronic wave function $\chi_1(\xi)$ since $n_1 = 5$, which is further confirmed in (c), where the experimental radial probability distribution for the (35, 5, 29, 0) state (solid line) is compared with TDSE calculations (dashed line), displaying a very good agreement. Moreover, the radial expansion of the photoelectron image for the (35, 5, 29, 0) state is larger compared to the adjacent states, which validates the involvement of the tunneling effect. According to the semiclassical formula given by Eq. (4.17), the image at -119.83 cm^{-1} should have the smallest radius as the photoelectrons' kinetic energy in this case is the lowest. However, the image size at -119.83 cm^{-1}, given by the black line in (b), exceeds the radius of the image recorded at -119.42 cm^{-1} (green line), what suggests that this state, i.e. (28, 26, 1, 0) is also perturbed due to coupling to the (35, 5, 29, 0) state. This is further confirmed by investigating the plotted Stark map in (d), where the experimental electric field (467.4 $\pm$ 0.5 V/cm) is marked by a grey bar showing that measurements at 119.42 cm^{-1} and -119.73 cm^{-1} were taken in a strongly perturbed region coinciding with crossings between the (35, 5, 29, 0) and (31, 13, 17, 0) and (28, 26, 1, 0) hydrogenic states. In the calculated photoabsorption spectra a line

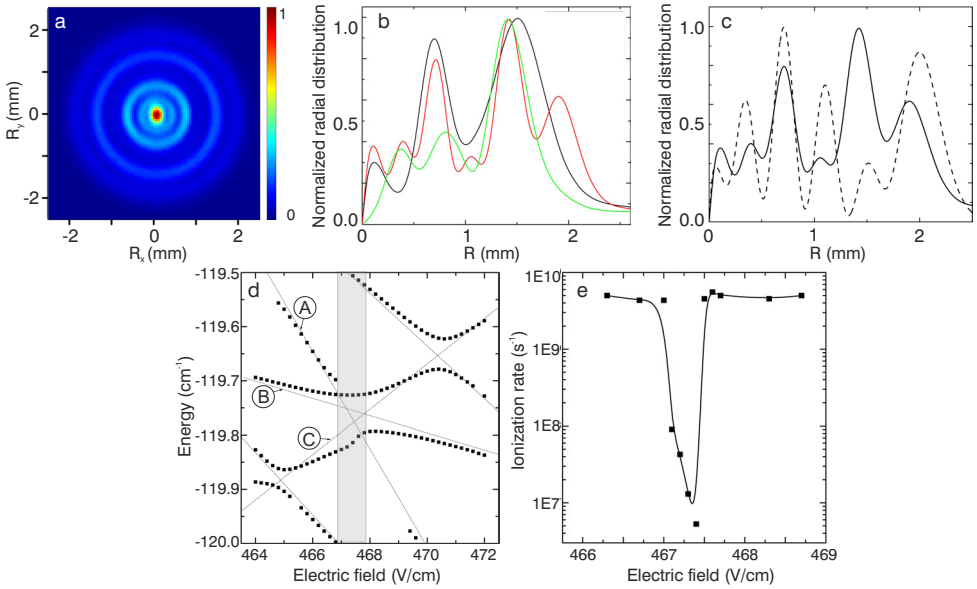

Figure 6.6: (a) Raw photoelectron image for the (35, 5, 29, 0) state measured at E = -119.73 cm^{-1} in the vicinity of an avoided crossing. (b) Experimental radial distributions of three adjacent resonances: E = -119.83 cm^{-1} (black line), E = -119.73 cm^{-1} (red line) and E = -119.49 cm^{-1} (green line), showing that the (35, 5, 29, 0) state has five minima and extends radially further than the other two states, which suggests the involvement of tunneling in the ionization process. (c) Comparison between the experimental (solid line) and theoretical (dashed line, obtained from TDSE calculations) radial distribution showing an excellent agreement in the position of the nodes. A calculated Stark map (d) indicates that the measurement was taken for a DC electric field of approximately 467.4 V/cm, where the (35, 5, 29, 0) state (A) has an avoided crossing with the (31, 13, 17, 0) (B) and (28, 26, 1, 0) (C) states. Note that the absence of black squares implies a disappearance of the oscillator strength in the photoabsorption spectra for a given state. The calculated ionization rate of the (35, 5, 29, 0) state, shown in (e), decreases by three orders of magnitude within a field range of 0.5 V/cm, due to the occurrence of interference narrowing.

width of the (35, 5, 29, 0) state was too broad to fit any Lorentz profile and consequently, it was impossible to determine the line-narrowing effect in this way. On the other hand, in TDSE calculations the (35, 5, 29, 0) state was very distinct due to its unique radial distribution with five minima. Therefore, for this state photocurrent fluxes as a function of time were computed for different values of the electric field, providing information about its lifetime and revealing a three orders of magnitude drop in the ionization rate over a field range of 0.5 V/cm as shown in (e), ipso facto confirming the occurrence of the interference narrowing effect.

Table 6.1: List of quasi-bound Stark states for which the nodal structure of the electronic wave function $\chi_1(\xi)$ was directly observed in the experiments due to the interference narrowing effect.

Energy (cm^{-1})	Electric field (V/cm)	Stark state (n, n_1, n_2, m)	Avoided crossing with: (n, n_1, n_2, m)
-130.43	468.0	(34, 1, 32, 0)	(27, 26, 0, 0)
-128.39	468.0	(35, 1, 33, 0)	(28, 21, 6, 0)
-128.23	468.0	(34, 2, 31, 0)	(29, 16, 12, 0)
-126.35	468.0	(35, 2, 32, 0)	(29, 17, 11, 0)
-124.28	468.0	(35, 3, 31, 0)	(30, 14, 15, 0)
-119.73	467.4	(35, 5, 29, 0)	(31, 13, 17, 0) (28, 26, 1, 0)
-117.42	467.4	(35, 6, 28, 0)	(29, 22, 6, 0)
-108.80	468.0	(35, 10, 24, 0)	(29, 27, 1, 0)

6.5 Conclusions

Hence, the observations encountered in the present experiments can be fully explained. Given the Stark lifetime ($\geqslant$ 100 ps) needed for the observation of sharply defined resonances in the photoexcitation efficiency as a function of laser wavelength, most helium photoionization microscopy measurements involved the excitation of quasi-bound Stark states in the middle or on the blue side of the Stark manifold. These states are strongly bound along both the ξ and η coordinates, and can only ionize as a result of core-induced coupling to red continuum states, i.e. states where the motion along the η coordinate is unbound. Consequently, as shown in Fig. 6.3, the interference patterns that are observed for these states are governed by the phase differences that the photoelectrons accumulate along multiple classical paths that they can follow between the ion and the detector. Moreover, a number of experiments were performed, where quasi-bound Rydberg states were excited on the red side of a Stark manifold, and in the vicinity of an avoided crossing with a blue state that induced an enhancement of the Rydberg state lifetime as a result of interference narrowing (listed in Table 6.1 and shown in Fig 6.4 and 6.6). All of these red states furthermore had in common that they occurred at energies just below the parabolic critical energy, which marks the top of the $V(\eta)$ potential. Under these circumstances, the electron may leave the atom by means of a tunneling process that leaves the quantization along the ξ coordinate intact. This ionization mechanism occurs in competition with the core-induced coupling mechanism and is more prominent for atoms with very small quantum defects ($\delta_l \ll 1$), where the hydrogenic structure of interfering Stark states is preserved to a greater degree [93]. Interference narrowing is essential, because it causes a destructive interference between the bound-continuum coupling amplitudes of the red and blue states that cross, decoupling one of these states from the ionization continuum. The lack of coupling causes

the hydrogenic tunneling to be the dominant ionization mechanism, thereby allowing the observation of the n_1 quantum number of the red Stark state on the detector, similar to the recent work on the hydrogen atom (Chapter 5 and [52]). At the same time the presented results are different from the photoionization microscopy experiments on lithium [172], where the hydrogenic behavior was forced by exciting only $m = 1$ Stark states, which are characterized by small quantum defects ($\delta_p = 0.0048$). For the similarities between hydrogen and lithium in $m = 1$ states see e.g. Fig. 2.3.

The utility of the photoionization microscopy technique in the present experiments on helium is that it visualizes, through an observation of the nodal structure of the red Stark state, the DC electric field-induced coupling between the red and blue Stark states in the vicinity of the avoided crossing. In future, it will be of great interest to perform experiments such as the ones presented here in a field-dependent manner, thereby allowing a complete mapping out the couplings that occur in Stark manifolds around field-induced avoided crossings.

Bibliography

[1] E. T. Whittaker. *A History of the theories of aether and electricity.* Green and Co., Dublin (1910).

[2] A. A. Michelson and E. W. Morley. *On the Relative Motion of the Earth and the Luminiferous Ether.* American Journal of Science, **34**, 333–345 (1887).

[3] A. Einstein. *Zur Elektrodynamik bewegter Körper.* Annalen der Physik, **322**, 891–921 (1905).

[4] R. C. Douga. *The presentation of the Planck radiation formula (tutorial).* Physics Education, **11**, 438–443 (1976).

[5] M. Planck. Verh. Dt. Phys. Ges., **2**, 202–204 (1900).

[6] M. Planck. Verh. Dt. Phys. Ges., **2**, 237–245 (1900).

[7] H. Becquerel. *Sur les radiations émises par phosphorescence.* Comptes Rendus, **122**, 420–421 (1896).

[8] J. Thomson. *Cathode rays.* Philosophical Magazine, **44**, 293 (1897).

[9] J. J. Thomson. *XXIV. On the structure of the atom: an investigation of the stability and periods of oscillation of a number of corpuscles arranged at equal intervals around the circumference of a circle; with application of the results to the theory of atomic structure.* Philosophical Magazine Series 6, **7**, 237–265 (1904).

[10] L. M. Rutherford. Philosophical Magazine, **21**, 669 (1911).

[11] N. Bohr. Philosophical Magazine, **26**, 476 (1913).

[12] G. H. J. Franck. *Über Zusammenstösse zwischen Elektronen und Molekülen des Quecksilberdampfes und die Ionisierungsspannung desselben.* Verh. Dtsch. Phys. Ges., **16**, 457–467 (1914).

[13] A. Sommerfeld. Annalen der Physik, **56**, 1 (1916).

[14] P. S. Epstein. *Zur Theorie des Starkeffektes.* Annalen der Physik, **50**, 489–520 (1916).

[15] K. Schwarzschild. *Zur Quantenhypothese.* Sitzungsberichten der Kgl. Preuss. Akad. d. Wiss., **26**, 548–568 (1916).

[16] A. Sommerfeld. *Zur Theorie des Zeeman-Efekts der Wasserstofflinien, mit einem Anhang uber den Stark-Efekt.* Physikalische Zeitschrift, **17**, 491–507 (1916).

[17] A. Messiah. *QUANTUM MECHANICS ; VOL. 1.* Amsterdam, North-holland (1964).

[18] L. de Brogile. Nature, **112**, 540 (1923).

[19] A. Einstein. *Über einen die Erzeugung und Verwandlung des Lichtes betreffenden heuristischen Gesichtspunkt.* Annalen der Physik, **17**, 132–148 (1905).

[20] W. Heisenberg. Zeitschrift für Physik, **33**, 879 (1925).

[21] E. Schrödinger. *An Undulatory Theory of the Mechanics of Atoms and Molecules.* Physical Review, **28**, 1049–1070 (1926).

[22] M. Born. *Zur Quantenmechanik der Stossvorgänge.* Zeitschrift für Physik, **37**, 863–867 (1926).

[23] W. Heisenberg. *Über den anschaulichen Inhalt der quantentheoretischen Kinematik und Mechanik.* Zeitschrift für Physik, **43**, 172–198 (1927).

[24] N. Bohr. *The Quantum Postulate and the Recent Development of Atomic Theory.* Nature, **121**, 580–590 (1928).

[25] H. White. *Introduction to atomic spectra.* McGraw-Hill book company, inc. (1934).

[26] W. K. Wootters and W. H. Zurek. *A single quantum cannot be cloned.* Nature, **299**, 802–803 (1982).

[27] B. Lohmann and E. Weigold. *Direct measurement of the electron momentum probability distribution in atomic hydrogen.* Physics Letters A, **86**, 139–141 (1981).

[28] I. E. Mccarthy and E. Weigold. *Wavefunction Mapping in Collision Experiments.* Reports on Progress in Physics, **51**, 299–392 (1988).

[29] C. E. Brion. *Looking at orbitals in the laboratory: The experimental investigation of molecular wavefunctions and binding energies by electron momentum spectroscopy.* International Journal of Quantum Chemistry, **29**, 1397–1428 (1986).

[30] C. E. Brion, G. Cooper, Y. Zheng, I. V. Litvinyuk and I. E. McCarthy. *Imaging of orbital electron densities by electron momentum spectroscopy - a chemical interpretation of the binary (e,2e) reaction.* Chemical Physics, **270**, 13–30 (2001).

[31] J. W. Watson, M. Ahmad, D. W. Devins, B. S. Flanders, D. L. Friesel, N. S. Chant, P. G. Roos and J. Wastell. ^{40}Ca(p, pn)^{39}Ca *and* ^{48}Ca(p, pn)^{47}Ca *neutron knockout reactions at 149.5 MeV.* Phys. Rev. C, **26**, 961–964 (1982).

[32] J. Mougey, M. Bernheim, A. Bussire, A. Gillebert, P. X. H, M. Priou, D. Royer, I. Sick and G. Wagner. *Quasi-free (e, e'p) scattering on 12C, 28Si, 40Ca and 58Ni.* Nuclear Physics A, **262**, 461 – 492 (1976).

[33] C. Monroe. *Quantum information processing with atoms and photons.* Nature, **416**, 238–246 (2002).

[34] D. T. Smithey, M. Beck, M. G. Raymer and A. Faridani. *Measurement of the Wigner distribution and the density matrix of a light mode using optical homodyne tomography: Application to squeezed states and the vacuum.* Physical Review Letters, **70**, 1244–1247 (1993).

[35] A. I. Lvovsky, H. Hansen, T. Aichele, O. Benson, J. Mlynek and S. Schiller. *Quantum State Reconstruction of the Single-Photon Fock State.* Physical Review Letters, **87**, 050402 (2001).

[36] A. Ourjoumtsev, H. Jeong, R. Tualle-Brouri and P. Grangier. *Generation of optical 'Schrödinger cats' from photon number states.* Nature, **448**, 784–786 (2007).

[37] J. S. Lundeen, B. Sutherland, A. Patel, C. Stewart and C. Bamber. *Direct measurement of the quantum wavefunction.* Nature, **474**, 188–191 (2011).

[38] J. Itatani, J. Levesque, D. Zeidler, H. Niikura, H. Pepin, J. C. Kieffer, P. B. Corkum and D. M. Villeneuve. *Tomographic imaging of molecular orbitals.* Nature, **432**, 867–871 (2004).

[39] D. Shafir, Y. Mairesse, D. M. Villeneuve, P. B. Corkum and N. Dudovich. *Atomic wavefunctions probed through strong-field light-matter interaction.* Nature Physics, **5**, 412–416 (2009).

[40] P. Puschnig, S. Berkebile, A. J. Fleming, G. Koller, K. Emtsev, T. Seyller, J. D. Riley, C. Ambrosch-Draxl, F. P. Netzer and M. G. Ramsey. *Reconstruction of Molecular Orbital Densities from Photoemission Data.* Science, **326**, 702–706 (2009).

[41] N. Hay, M. Lein, R. Velotta, R. D. Nalda, E. Heesel, M. Castillejo, P. L. Knight and J. P. Marangos. *Investigations of electron wave-packet dynamics and high-order harmonic generation in laser-aligned molecules.* Journal of Modern Optics, **50**, 561–577 (2003).

[42] S. Haessler *et al. Attosecond imaging of molecular electronic wavepackets.* Nature Physics, **6**, 200–206 (2010).

[43] H. Niikura. *Mapping Molecular Orbital Symmetry on High-Order Harmonic Generation Spectrum Using Two-Color Laser Fields.* Physical Review Letters, **105(5)**, p. 053003 (2010).

[44] H. Niikura. *Probing the Spatial Structure of a Molecular Attosecond Electron Wave Packet Using Shaped Recollision Trajectories.* Physical Review Letters, **107(9)**, p. 093004 (2011).

[45] M. F. Crommie, C. P. Lutz and D. M. Eigler. *Confinement of Electrons to Quantum Corrals on a Metal-Surface.* Science, **262**, 218–220 (1993).

[46] J. Repp, G. Meyer, S. M. Stojkovi, A. Gourdon and C. Joachim. *Molecules on Insulating Films: Scanning-Tunneling Microscopy Imaging of Individual Molecular Orbitals.* Physical Review Letters, **94**, 026803 (2005).

[47] L. Holmegaard *et al. Photoelectron angular distributions from strong-field ionization of oriented molecules.* Nature Physics, **6**, 428–432 (2010).

[48] A. Rouzée, A. Harvey, F. Kelkensberg, W. K. Siu, G. Gademann, O. Smirnova and M. J. Vrakking. *Imaging the electronic structure of bonding orbitals in the XUV ionization of aligned molecules.* (submitted for publication) (2013).

[49] Y. N. Demkov, V. D. Kondratovich and V. N. Ostrovskii. *Interference of electrons resulting from the photoionization of an atom in an electric field.* JETP Letters, **34**, 403– (1981).

[50] V. D. Kondratovich and V. N. Ostrovsky. *Resonance and interference phenomena in the photoionisation of a hydrogen atom in a uniform electric field. I. Resonances below and above the potential barrier.* Journal of Physics B-Atomic Molecular and Optical Physics, **17**, 1981–2010 (1984).

[51] V. D. Kondratovich and V. N. Ostrovsky. *Resonance and interference phenomena in the photoionization of a hydrogen atom in a uniform electric field. IV. Differential cross sections.* Journal of Physics B-Atomic Molecular and Optical Physics, **23**, 3785–3809 (1990).

[52] A. S. Stodolna, A. Rouzée, F. Lépine, S. Cohen, F. Robicheaux, A. Gijsbertsen, J. H. Jungmann, C. Bordas and M. J. J. Vrakking. *Hydrogen Atoms under Magnification: Direct Observation of the Nodal Structure of Stark States.* Physical Review Letters, **110**, 213001 (2013).

[53] P. Zeeman. *The Effect of Magnetisation on the Nature of Light Emitted by a Substance.* Nature, **55**, 347 (1897).

[54] W. Voigt. *Ueber das elektrische Analogon des Zeemaneffectes.* Annalen der Physik, **309**, 197–208 (1901).

[55] J. Stark. *Observation of the Separation of Spectral Lines by an Electric Field.* Nature, **92**, 401 (1913).

[56] A. Surdo. *Sul fenomeno analogo a quello di Zeeman nel campo elettrico.* Rendiconti della Reale Accademia dei Lincei, **22**, 664–666 (1913).

[57] A. Surdo. *Über das elektrische Analogon des Zeeman-Phnomens.* Zeitschrift für Physik, **15**, 122 (1914).

[58] J. S. Foster. *Observations on the Stark Effect in Hydrogen and Helium.* Physical Review, **23**, 667–684 (1924).

[59] A. Sommerfeld. *Atombau und Spektrallinien.* Fiedr. Vieweg & Sohn (1960).

[60] T. Takamine and N. Kokubu. *The Effect of an Electric Field on the Spectrum Lines of Hydrogen Part III.* Memoirs of the College of Science, Kyoto Imperial University, **3**, 271–273 (1918).

[61] H. Kramers. *Intensities of Spectral Lines.* Andr. Fred. Host & Son (1919).

[62] P. S. Epstein. *The Stark Effect from the Point of View of Schroedinger's Quantum Theory.* Physical Review, **28**, 695–710 (1926).

[63] H. Bethe and E. Salpeter. *Quantum mechanics of one- and two- electron atoms.* Springer (1957).

[64] E. M. Landau, L. D. & Lifshitz. *Quantum Mechanics Non-Relativistic Theory.* Oxford, Pergamon Press (1965).

[65] T. F. Gallagher. *Rydberg atoms.* Cambridge University Press (1994).

[66] D. Park. *Relation between the parabolic and spherical eigenfunctions of hydrogen.* Zeitschrift für Physik, **159**, 155–157 (1960).

[67] H. J. Silverstone. *Perturbation theory of the Stark effect in hydrogen to arbitrarily high order.* Physical Review A, **18**, 1853–1864 (1978).

[68] M. L. Zimmerman, M. G. Littman and D. Kleppner. *Stark structure of the Rydberg states of alkali-metal atoms.* Physical Review A, **20**, 2251–2275 (1979).

[69] G. J. Hatton. *Avoided crossings of resonance energy curves of one-electron atoms in an external electric field.* Physical Review A, **16**, 1347–1351 (1977).

[70] T. Bergeman. *Relativistically Enhanced Ionization Rates at Stark-Effect Level Crossings in Hydrogen.* Physical Review Letters, **52**, 1685–1688 (1984).

[71] M. J. Seaton. *Quantum defect theory.* Reports on Progress in Physics, **46**, 167 (1983).

[72] C. Fabre, Y. Kaluzny, R. Calabrese, L. Jun, P. Goy and S. Haroche. *Study of non-hydrogenic near degeneracies between m sublevels in the linear Stark effect of sodium Rydberg states.* Journal of Physics B: Atomic and Molecular Physics, **17**, 3217 (1984).

[73] R. Gebauer and H. R. van Traubenberg. *Über den Starkeffekt dritter Ordnung bei den Serienlinien H_β und H_γ des Wasserstof.* Zeitschrift für Physik, **62**, 289 (1930).

[74] C. Lanczos. Zeitschrift für Physik, **68**, 204 (1931).

[75] P. M. Koch and D. R. Mariani. *Precise Measurement of the Static Electric-Field Ionization Rate for Resolved Hydrogen Stark Substates.* Physical Review Letters, **46**, 1275–1278 (1981).

[76] M. H. Rice and J. R. H. Good. *Stark Effect in Hydrogen.* Journal of Optical Society of America, **52**, 239–246 (1962).

[77] J. O. Hirschfelder and L. A. Curtiss. *Spontaneous Ionization of a Hydrogen Atom in an Electric Field. I.* The Journal of Chemical Physics, **55**, 1395–1402 (1971).

[78] D. S. Bailey, J. R. Hiskes and A. Riviere. *Electric field ionization probabilities for the hydrogen atom.* Nuclear Fusion, **5**, 41 (1965).

[79] R. J. Damburg and V. V. Kolosov. *An asymptotic approach to the Stark effect for the hydrogen atom.* Journal of Physics B: Atomic and Molecular Physics, **11**, 1921 (1978).

[80] R. J. Damburg and V. V. Kolosov. *A hydrogen atom in a uniform electric field. III.* Journal of Physics B: Atomic and Molecular Physics, **12**, 2637 (1979).

[81] H. Rottke and K. H. Welge. *Photoionization of the hydrogen atom near the ionization limit in strong electric fields.* Physical Review A, **33**, 301–311 (1986).

[82] S. Feneuille, S. Liberman, J. Pinard and A. Taleb. *Observation of Fano Profiles in Photoionization of Rubidium in the Presence of a dc Field.* Physical Review Letters, **42**, 1404–1406 (1979).

[83] M. G. Littman, M. L. Zimmerman and D. Kleppner. *Tunneling Rates for Excited States of Sodium in a Static Electric Field.* Physical Review Letters, **37**, 486–489 (1976).

[84] M. G. Littman, M. M. Kash and D. Kleppner. *Field-Ionization Processes in Excited Atoms.* Physical Review Letters, **41**, 103–107 (1978).

[85] W. van de Water, D. R. Mariani and P. M. Koch. *Ionization of highly excited helium atoms in an electric field.* Physical Review A, **30**, 2399–2412 (1984).

[86] U. Fano. *Effects of Configuration Interaction on Intensities and Phase Shifts.* Physical Review, **124**, 1866–1878 (1961).

[87] J.-Y. Liu, P. McNicholl, D. A. Harmin, J. Ivri, T. Bergeman and H. J. Metcalf. *Interference narrowing at crossings of sodium Stark resonances.* Physical Review Letters, **55**, 189–192 (1985).

[88] S. Feneuille, S. Liberman, E. Luc-Koenig, J. Pinard and A. Taleb. *Field-induced stabilisation of Stark states in the rubidium atom.* Journal of Physics B: Atomic and Molecular Physics, **15**, 1205 (1982).

[89] D. A. Harmin. *Hydrogenic Stark effect: Properties of the wave functions.* Physical Review A, **24**, 2491–2512 (1981).

[90] D. A. Harmin. *Theory of the Stark effect.* Physical Review A, **26**, 2656–2681 (1982).

[91] D. A. Harmin. *Analytical study of quasidiscrete Stark levels in Rydberg atoms.* Physical Review A, **30**, 2413–2428 (1984).

[92] P. McNicholl, T. Bergeman and H. J. Metcalf. *Lifetime measurements of interference-narrowed sodium Stark resonances.* Physical Review A, **37**, 33023312 (1988).

[93] D.-H. Yang, D. Lieberman, P. van der Straten, T. Bergeman and H. Metcalf. *Precision mapping of electrostatic fields using interference-narrowed Stark resonances.* Physical Review A, **40**, 5026–5039 (1989).

[94] A. Nussenzweig, E. E. Eyler, T. Bergeman and E. Pollack. *Line shapes of ionizing Stark resonances in helium.* Physical Review A, **41**, 4944–4957 (1990).

[95] G. D. Stevens, C.-H. Iu, T. Bergeman, H. J. Metcalf, I. Seipp, K. T. Taylor and D. Delande. *Precision measurements on lithium atoms in an electric field compared with R -matrix and other Stark theories.* Physical Review A, **53**, 1349–1366 (1996).

[96] A. König, J. Neukammer, H. Hieronymus and H. Rinneberg. *Field-ionization Stark spectra of Ba Rydberg atoms at high density of states.* Physical Review A, **43**, 2402–2415 (1991).

[97] E. Titchmarsh. *Elgenfunction Expansions Associated With Second Order Differential Equations Part II.* Oxford Univ. Press (1958).

[98] F. Robicheaux and J. Shaw. *Calculated electron dynamics in an electric field.* Physical Review Letters, **56**, 278–289 (1997).

[99] R. J. Damburg and V. V. Kolosov. *A hydrogen atom in a uniform electric field.* Journal of Physics B: Atomic and Molecular Physics, **9**, 3149 (1976).

[100] E. Luc-Koenig and A. Bachelier. *Interpretation of Electric-Field-Induced Oscillations in the Cross Section of a One-Electron Atom above the Ionization Limit.* Physical Review Letters, **43**, 921–924 (1979).

[101] E. Luc-Koenig and A. Bachelier. *Systematic theoretical study of the Stark spectrum of atomic hydrogen. II. Density of oscillator strengths. Comparison with experimental absorption spectra in solid-state and atomic physics.* Journal of Physics B: Atomic and Molecular Physics, **13**, 1769 (1980).

[102] Y. Ishida and S. Hiyama. Scientific Papers of the Institute of Physical and Chemical Research, **9**, 1 (1928).

[103] S. Alliluev and I. Malkin. *Calculations of the Stark effect in hydrogen atoms by using the dynamical symmetry O(2,2) × O(2).* Journal of Experimental and Theoretical Physics, **39**, 627 (1974).

[104] J. Killingbeck. *Quantum-mechanical perturbation theory.* Reports on Progress in Physics, **40**, 963 (1977).

[105] P. M. Koch. *Resonant States in the Nonperturbative Regime: The Hydrogen Atom in an Intense Electric Field.* Physical Review Letters, **41**, 99–103 (1978).

[106] C. Lanczos. Zeitschrift für Physik, **65**, 431 (1930).

[107] D. A. Harmin. *Theory of the Nonhydrogenic Stark Effect.* Physical Review Letters, **49**, 128–131 (1982).

[108] G. M. Lankhuijzen and L. D. Noordam. *Atomic streak camera.* Optics Communications, **129**, 361–368 (1996).

[109] F. Robicheaux and J. Shaw. *Calculated electron dynamics in a strong electric field.* Physical Review Letters, **77**, 4154–4157 (1996).

[110] A. M. Ollagnier. *Microscopie de Photoïonisation :une étude classique, semi-classique et quantiqu.* Ph.D. thesis, lUNIVERSITÉ CLAUDE BERNARD - LYON 1 (2007).

[111] M. J. Amoruso and W. R. Johnson. *Relativistic One-Electron Calculations of Shielded Atomic Hyperfine Constants.* Physical Review A, **3**, 6–12 (1971).

[112] W. Johnson, D. Kolb and K.-N. Huang. *Electric-dipole, quadrupole, and magnetic-dipole susceptibilities and shielding factors for closed-shell ions of the He, Ne, Ar, Ni (Cu+), Kr, Pb, and Xe isoelectronic sequences.* Atomic Data and Nuclear Data Tables, **28**, 333 – 340 (1983).

[113] D. Kolb, W. R. Johnson and P. Shorer. *Electric and magnetic susceptibilities and shielding factors for closed-shell atoms and ions of high nuclear charge.* Physical Review A, **26**, 19–31 (1982).

[114] A. Eppink and D. Parker. *Velocity Map Imaging of ions and electron using electostatic lenses: Application in photoelectron and photofragment ion imaging of molecular oxygen.* Review of Scientific Instruments, **68**, 3447–3484 (1997).

[115] W. Johnson and G. Soff. *The lamb shift in hydrogen-like atoms, 1⩽ Z ⩽ 110.* Atomic Data and Nuclear Data Tables, **33**, 405 – 446 (1985).

[116] H. L. Offerhaus, C. Nicole, F. Lepine, C. Bordas, F. Rosca-Pruna and M. J. J. Vrakking. *A magnifying lens for velocity map imaging of electrons and ions.* Review of Scientific Instruments, **72**, 3245–3248 (2001).

[117] L. C. Lee, X. Wang and M. Suto. *Quantitative photoabsorption and fluorescence spectroscopy of H2S and D2S at 49-240 nm.* Journal of Chemical Physics, **86**, 4353–4361 (1987).

[118] D. Proch and T. Trickl. *A High-Intensity Multi-Purpose Piezoelectric Pulsed Molecular-Beam Source.* Review of Scientific Instruments, **60**, 713–716 (1989).

[119] G. van Veen, K. Mohamed, T. Baller and A. de Vries. *Photofragmentation of H2S in the first continuum.* Chemical Physics, **74**, 261 – 271 (1983).

[120] D. S. Bethune. *Dye cell design for high-power low-divergence excimer-pumped dye lasers.* Applied Optics, **20**, 1897–1899 (1981).

[121] U. Czarnetzki, K. Miyazaki, T. Kajiwara, K. Muraoka, M. Maeda and H. F. Döbele. *Comparison of various two-photon excitation schemes for laser-induced fluorescence spectroscopy in atomic hydrogen.* Journal of Optical Society of America Bbickel, **11**, 2155–2162 (1994).

[122] G. A. Bickel and G. A. McRae. *Determination of the 1s-2s two-photon excitation cross-section in atomic hydrogen.* Spectrochimica Acta Part B: Atomic Spectroscopy, **55**, 57 – 63 (2000).

[123] P. Drell and S. Chu. *A megawatt dye laser oscillator-amplifier system for high resolution spectroscopy.* Optics Communications, **28**, 343 – 348 (1979).

[124] M. Ashfold, R. Dixon, K. Rosser, R. Stickland and C. Western. *Sub-doppler spectroscopy of the C' v2 = 2 Rydberg level of ND3 at vacuum ultraviolet energies.* Chemical Physics, **101**, 467 – 482 (1986).

[125] L. A. Rahn, R. L. Farrow and G. J. Rosasco. *Measurement of the self-broadening of the* H_2 *Q (0˘5) Raman transitions from 295 to 1000 K.* Phys. Rev. A, **43**, 6075–6088 (1991).

[126] M. D. D. Rosa and R. L. Farrow. *Cross sections of photoionization and ac Stark shift measured from Doppler-free B ⩽ X(0, 0) excitation spectra of CO.* Journal of Optical Society of America B, **16**, 861–870 (1991).

[127] M. Salour. *Powerful dye laser oscillator-amplifier system for high resolution and coherent pulse spectroscopy.* Optics Communications, **22**, 202 – 206 (1977).

[128] E. S. Lee and J. W. Hahn. *Four-pass amplifier for the pulsed amplification of a narrow-bandwidth continuous-wave dye laser.* Optics Letters, **21**, 1836–1838 (1996).

[129] J. W. Hahn and Y. S. Yoo. *Suppression of Amplified Spontaneous Emission from a Four-Pass Dye Laser Amplifier.* Applied Op, **37**, 4867–4870 (1998).

[130] E. Cromwell, T. Trickl, Y. T. Lee and A. H. Kung. *Ultranarrow Bandwidth Vuv-Xuv Laser System.* Review of Scientific Instruments, **60**, 2888–2892 (1989).

[131] J. T. F. Johnston, R. H. Brady and W. Proffitt. *Powerful single-frequency ring dye laser spanning the visible spectrum.* Applied Optics, **21**, 2307–2316 (1982).

[132] E. Hecht. *Optics.* Addison Wesley (2002).

[133] V. Blanchet. *Femtosecond resolved dynamics in small polyatomic molecules by velocity map imaging.* AIP Conference Proceedings, **1501**, 1355–1364 (2012).

[134] M. E. Corrales, G. Gitzinger, J. Gonząlez-Vązquez, V. Loriot, R. de Nalda and L. Baśares. *Velocity Map Imaging and Theoretical Study of the Coulomb Explosion of CH3I under Intense Femtosecond IR Pulses.* The Journal of Physical Chemistry A, **116**, 2669–2677 (2012).

[135] G. Sansone *et al. Electron Localization following Attosecond Molecular Photoionization.* Nature, **465**, 763–766 (2010).

[136] F. Calegari *et al. Observation of ultrafast electron dynamics in N2 molecules induced by attosecond pulses.* In *CLEO: 2013.* Optical Society of America (2013), QF2C.5.

[137] J. H. Jungmann, A. Gijsbertsen, J. Visser, J. Visschers, R. M. A. Heeren and M. J. J. Vrakking. *A new imaging method for understanding chemical dynamics: Efficient slice imaging using an in-vacuum pixel detector.* Review of Scientific Instruments, **81**, 103112 (2010).

[138] A. T. Clark *et al. Multimass Velocity-Map Imaging with the Pixel Imaging Mass Spectrometry (PImMS) Sensor: An Ultra-Fast Event-Triggered Camera for Particle Imaging.* The Journal of Physical Chemistry A, **116**, 10897–10903 (2012).

[139] C. Hock, J. B. Kim, M. L. Weichman, T. I. Yacovitch and D. M. Neumark. *Slow photoelectron velocity-map imaging spectroscopy of cold negative ions.* The Journal of Chemical Physics, **137**, 244201 (2012).

[140] Y. Huismans *et al. Time-Resolved Holography with Photoelectrons.* Science, **331**, 61–64 (2011).

[141] K. S. E. Eikema, W. Ubachs, W. Vassen and W. Hogervorst. *Lamb shift measurement in the* $1\mathrm{t}^1S$ *ground state of helium.* Phys. Rev. A, **55**, 1866–1884 (1997).

[142] J. Q. Searcy. *A supersonic molecular beam metastable atom source initiated by direct discharge.* Review of Scientific Instruments, **45**, 589–590 (1974).

[143] A. V. Phelps. *Absorption Studies of Helium Metastable Atoms and Molecules.* Physical Review, **99**, 1307–1313 (1955).

[144] E. L. Leasure, C. R. Mueller and T. Y. Ridley. *"Hot" metastable atom, molecular beam source.* Review of Scientific Instruments, **46**, 635–637 (1975).

[145] D. W. Fahey, W. F. Parks and L. D. Schearer. *High flux beam source of thermal rare-gas metastable atoms.* Journal of Physics E: Scientific Instruments, **13**, 381 (1980).

[146] W. Rooijakkers, W. Hogervorst and W. Vassen. *An intense collimated beam of metastable helium atoms by two-dimensional laser cooling.* Optics Communications, **123**, 321–330 (1996).

[147] J. Ashmore and R. Sang. *Cathode design for a low-velocity metastable neon cold cathode discharge source.* MEASUREMENT SCIENCE & TECHNOLOGY, **12**, N17–N21 (2001).

[148] F. B. Dunning, R. D. Rundel and R. F. Stebbings. *Determination of secondary electron ejection coefficients for rare gas metastable atoms.* Review of Scientific Instruments, **46**, 697–701 (1975).

[149] M. Brieger, H. Bsener, A. Hese, F. v.Moers and A. Renn. *Enhancement of single frequency {SGH} in a passive ring resonator.* Optics Communications, **38**, 423 – 426 (1981).

[150] R. Drever, J. Hall, F. Kowalski, J. Hough, G. Ford, A. Munley and H. Ward. *Laser phase and frequency stabilization using an optical resonator.* Applied Physics B, **31**, 97–105 (1983).

[151] S. Hussain, M. Saleem and M. A. Baig. *Measurement of the oscillator strength distribution in helium.* Physical Review A, **76**, – (2007).

[152] P. J. J. Tol, N. Herschbach, E. A. Hessels, W. Hogervorst and W. Vassen. *Large numbers of cold metastable helium atoms in a magneto-optical trap.* Phys. Rev. A, **60**, R761–R764 (1999).

[153] W. Ubachs, W. Vassen, E. J. Salumbides and K. S. E. Eikema. *Precision metrology on the hydrogen atom in search for new physics.* Annalen der Physik, **525**, A113–A115 (2013).

[154] J. C.-H. Chen, B. L. Hanson, S. Z. Fisher, P. Langan and A. Y. Kovalevsky. *Direct observation of hydrogen atom dynamics and interactions by ultrahigh resolution neutron protein crystallography.* Proceedings of the National Academy of Sciences, **109**, 15301–15306 (2012).

[155] P. M. Koch and D. R. Mariani. *Double-resonance Stark spectroscopy as a probe of hydrogen substate production in fast atomic collisions.* Journal of Physics B: Atomic and Molecular Physics, **13**, L645 (1980).

[156] W. L. Glab and M. H. Nayfeh. *Stark-induced resonances in the photoionization of hydrogen.* Physical Review A, **31**, 530–532 (1985).

[157] G. Alvarez, R. J. Damburg and H. J. Silverstone. *Photoionization of atomic hydrogen in an electric field.* Physical Review A, **44**, 3060–3082 (1991).

[158] V. D. Kondratovich and V. N. Ostrovsky. *Resonance and interference phenomena in the photoionisation of a hydrogen atom in a uniform electric field. II. Overlapping resonances and interference.* Journal of Physics B-Atomic Molecular and Optical Physics, **17**, 2011–2038 (1984).

[159] V. D. Kondratovich and V. N. Ostrovsky. *Resonance and interference phenomena in the photoionisation of a hydrogen atom in a uniform electric field. III. Comparison with recent experimental and theoretical results.* Journal of Physics B-Atomic Molecular and Optical Physics, **23**, 21–43 (1990).

[160] V. V. Beletsky. *Essays on the motion of celestial bodies.* Birkhäuser Verlag (2001).

[161] C. Bordas, F. Lepine, C. Nicole and M. J. J. Vrakking. *Semiclassical description of photoionization microscopy.* Physical Review A, **68**, – (2003).

[162] F. Lepine, C. Bordas, C. Nicole and M. J. J. Vrakking. *Atomic photoionization processes under magnification.* Physical Review A, **70**, 033417 (2004).

[163] C. Bordas. *Classical motion of a photoelectron interacting with its ionic core: Slow photoelectron imaging.* Physical Review A, **58**, 400–410 (1998).

[164] C. Blondel, C. Delsart and F. Dulieu. *The photodetachment microscope.* Physical Review Letters, **77**, 3755–3758 (1996).

[165] C. Nicole, H. L. Offerhaus, M. J. J. Vrakking, F. Lépine and C. Bordas. *Photoionization Microscopy.* Phys. Rev. Lett., **88**, 133001 (2002).

[166] L. B. Zhao and J. B. Delos. *Dynamics of electron wave propagation in photoionization microscopy. I. Semiclassical open-orbit theory.* Physical Review A, **81**, 053417 (2010).

[167] M. L. Du and J. B. Delos. *Effect of Closed Classical Orbits on Quantum Spectra - Ionization of Atoms in a Magnetic-Field .1. Physical Picture and Calculations.* Physical Review A, **38**, 1896–1912 (1988).

[168] J. Gao, J. B. Delos and M. Baruch. *Closed-Orbit Theory of Oscillations in Atomic Photoabsorption Cross-Sections in a Strong Electric-Field .1. Comparison between Theory and Experiments on Hydrogen and Sodium above Threshold.* Physical Review A, **46**, 1449–1454 (1992).

[169] J. Gao and J. B. Delos. *Closed-orbit theory of oscillations in atomic photoabsorption cross sections in a strong electric field. II. Derivation of formulas.* Physical Review A, **46**, 1455–1467 (1992).

[170] T. S. Luk, L. DiMauro, T. Bergeman and H. Metcalf. *Continuum Stark Spectroscopy.* Physical Review Letters, **47**, 83–86 (1981).

[171] L. B. Zhao and J. B. Delos. *Dynamics of electron wave propagation in photoionization microscopy. II. Quantum-mechanical formulation.* Physical Review A, **81**, 053418 (2010).

[172] S. Cohen, M. M. Harb, A. Ollagnier, F. Robicheaux, M. J. J. Vrakking, T. Barillot, F. Lépine and C. Bordas. *Wave Function Microscopy of Quasibound Atomic States.* Physical Review Letters, **110**, 183001 (2013).

[173] H. Wimmel. *Quantum Physics & Observed Reality: A Critical Interpretation of Quantum Mechanics.* World Scientific, Singapore (1992).

[174] C. Jönsson. *Elektroneninterferenzen an mehreren künstlich hergestellten Feinspalten.* Zeitschrift für Physik, **161**, 454–474 (1961).

[175] L. D. Noordam and R. R. Jones. *Probing Rydberg electron dynamics.* Journal of Modern Optics, **44**, 2515–2532 (1997).

[176] M. L. Du. *Oscillations of electron flux in photodetachment of* H^- *in an electric field.* Physical Review A, **40**, 4983–4987 (1989).

[177] C. Delsart, L. Cabaret, C. Blondel and R. J. Champeau. *Two-step high-resolution laser spectroscopy of the Stark substates of the n=44 level in atomic hydrogen.* Journal of Physics B: Atomic and Molecular Physics, **20**, 4699 (1987).

[178] H. Wang, M. Chini, S. Chen, C.-H. Zhang, F. He, Y. Cheng, Y. Wu, U. Thumm and Z. Chang. *Attosecond Time-Resolved Autoionization of Argon.* Physical Review Letters, **105**, 143002 (2010).

[179] C. T. L. Smeenk. *A New Look at the Hydrogen Wave Function.* Physics, **6**, 58 (2013).

[180] C. A. Kocher. *Vanishing of Dipole Matrix Elements at Level Crossings.* Physical Review A, **6**, 35–37 (1972).

Summary

The development of *QuantumMechanics* in the early 20^{th} century provided a new mathematical tool to describe phenomena occurring at the nano-scale and changed the way that scientists understand nature. Although the theory gives a qualitative explanation of the effects taking place on the nano-scale, it contains numerous elements that cannot be classically intuited, such as wave-particle duality, the Heisenberg uncertainty principle, the Pauli exclusion principle etc. A fundamental role in quantum mechanics plays the wave function ψ, which satisfies the time-dependent Schrödinger equation and provides all information about the dynamical properties of a quantum system at a given instant of time t. From the theoretical point of view it is possible to predict what a wave function is, but a measurement of a wave function remains tough due to its exquisite fragility. Strictly speaking, one of the peculiarities of quantum mechanics is that most attempts to directly observe a wave function actually destroy it in a process called collapse. Despite this difficulty, in the last decades many direct and indirect experimental methods were proposed resulting in wave function imaging of such quantum objects as photons, nuclei, atoms and molecules (Chapter 1).

In this thesis a novel technique – photoionization microscopy – is exploited to directly observe electronic wave functions in atoms like hydrogen and helium. This alternative imaging technique, proposed more than 30 years ago, makes use of a unique property of the hydrogen atom placed in a static electric field, namely, the symmetry of its Hamiltonian operator, which ensures that the Schrödinger equation is separable in parabolic coordinates (ξ, η, φ). Consequently, the wave function may be written as: $\psi(\eta, \xi, \varphi) = \frac{1}{\sqrt{2\pi\xi\eta}}\chi_1(\xi)\chi_2(\eta)e^{im\varphi}$, where $\chi_1(\xi)$ and $\chi_2(\eta)$ are functions describing the electron motion along the ξ and η coordinate, respectively, and have n_1, n_2 nodes, where n_1, n_2 are so-called parabolic quantum numbers. As shown explicitly in Chapter 2, for each coordinate there exists a certain effective potential acting on the electron and resulting in motion that is always finite along the ξ coordinate. Hence, for the ionization to occur the electron must escape to $\eta = \infty$, which is possible in two situations: (1) if it has enough energy to surmount the top of the $V(\eta)$ potential or (2) when the energy lies below the top of the $V(\eta)$ potential, and when the electron has a nonzero probability of tunneling through the barrier. In the latter case the ideal conditions for photoionization microscopy are created since the tunneling process leaves the quantization along the ξ coordinate intact. The theory predicts that a projection of such photoelectrons onto a two-dimensional detector placed perpendicularly to the static electric field would allow the experimental measurement of interference patterns directly reflecting the nodal structure of the electronic wave function $\chi_1(\xi)$.

In the framework of this thesis the validity of photoionization microscopy as a

technique suitable for imaging electronic wave functions is tested for two, fundamentally different (from the point of view of quantum mechanics) atoms: hydrogen and helium. The main purpose of Chapter 2 is to present theoretical and experimental consequences resulting from the finite size of the ionic core in helium and other nonhydrogenic atoms in contrast to hydrogen, whose core contains only a single proton. It is shown that the non–Coulombic potential of nonhydrogenic atoms leads to coupling among Stark states. Consequently, so-called avoided crossings arise between levels that in hydrogen would cross and an additional type of field ionization mechanism occurs: (3) when the electron's energy lies below the top of the $V(\eta)$ potential the electron can be scattered by the core into another parabolic state, which lies above the barrier in $V(\eta)$, resulting in a process similar to autoionization. However, this type of field ionization, which is a dominant decay mechanism in nonhydrogenic atoms, removes the quantization along the ξ coordinate and by that very fact precludes a measurement of the electronic wave function in nonhydrogenic atoms. Nevertheless, as shown in Chapter 2, a peculiar effect takes place in the vicinity of avoided crossings, so-called interference narrowing, which alters the ionization process and in principle may permit a direct observation of the nodal structure in $\chi_1(\xi)$, as explored in Chapter 6.

To turn the idea of mapping wave functions with photoionization microscopy into experimental reality was by no means trivial. According to the theoretical description a "photoionization microscope" should comprise two plates producing a homogeneous electric field, a beam of neutral atoms, a focused laser beam that photoionizes the atoms, and a position-sensitive detector placed perpendicular to the electric field axis, on which the resulting photoelectrons are projected. Chapter 3 provides a detailed description of the experimental realization of this concept, separately for hydrogen and for helium, since the intrinsic differences between these atoms resulted in designing two distinct experimental setups. The hydrogen atom, in contrast to helium, does not exist as a chemically stable species in nature and thus in the experiments it had to be produced by means of photodissociation of a H_2S molecule. High ionization thresholds in both atoms excluded the original idea of one-photon excitation from the ground state into high lying Stark states. Therefore, alternative photoionization schemes were used, which took advantage of atoms prepared in metastable states prior to being photoexcited. For helium, which as a noble gas has metastable states resistant to a DC electric field, a discharge source providing a high-flux beam of (2^1S) metastable helium atoms was built. Since hydrogen does not have the same property it was photoexcited into $n = 2$ states, by absorbing two photons at 243 nm, in the same interaction region where it was subsequently photoexcited into Stark states by absorbing one photon of UV light delivered by a home-built, tunable and narrow-band pulsed dye amplifier. The final photoexcitation step in the helium experiments was accomplished by making use of one photon of UV light produced by frequency doubling the output of a cw ring dye laser. To fulfill the requirements regarding the homogeneous electric field and the position-sensitive detector, a velocity map imaging spectrometer was used. Inside this device a DC electric field was created by applying a voltage difference across the electrodes, which acted as an electrostatic lens enabling to focus the created pho-

toelectrons sharply on the detector. In our experiments the detector consisted of two micro-channel plates, a phosphor screen and a CCD camera. The last crucial element in both setups was an Einzel lens, which ensured magnification of recorded photoelectron images by one order of magnitude. The calculated efficiencies of the overall process in both experiments are given in Chapter 3 together with the description of the main limiting factors in both systems.

During the photoionization microscopy experiments hydrogen and helium atoms were photoionized in the presence of DC electric fields and the resulting photoelectrons were projected on a detector, creating characteristics oscillatory structures. In the experiments where atoms were photoexcited into the continuum of Stark states, i.e. when the field ionization process was via mechanism (1), the observed interference patterns are fully understood considering the phase accumulation along different trajectories that allow the photoelectrons to reach the same position on the two-dimensional detector. In Chapter 4 the experimental results for hydrogen atoms are presented, where the aforementioned interference patterns are observed and explained within the framework of semiclassical theory. In the recorded photoelectron images distinct oscillatory structures are distinguished, related to so-called "direct" and "indirect" ionization processes, which differ in the circumstances under which the photoelectron is launched, i.e. whether it interacted with the parent ion or not. For the first time it was observed that direct and indirect trajectories lead to beating patterns in the inner part of the photoelectron images. This effect was studied in greater detail and was very well reproduced by the semiclassical calculations.

According to the theory of photoionization microscopy, in the special case when the photoionization follows a resonant excitation into a Stark state, the observed interference patterns directly reflect the nodal structure of the Stark state prepared in the experiment. This resonant effect is extensively investigated in Chapter 5, where the photoelectron images recorded for hydrogen atoms excited into various Stark states are presented. Remarkably, the number of observed dark fringes equals to n_1, i.e. the number of nodes of the electronic wave function $\chi_1(\xi)$, irrespective of the laser polarization or the electric field strength. To confirm that the observed interference structures are caused by the resonant effect, photoelectron images were recorded also for energies lying below and above the Stark state. For these non-resonant cases the interference patterns have less rings and their origin can be fully understood considering quantum-mechanical path length differences experienced by the photoelectron along multiple interfering pathways, as presented in Chapter 4. Moreover, the image recorded at the resonance extends radially further indicating an involvement of a quantum effect since the photoelectrons reach classically forbidden positions on the detector. This observation confirms that the ionization mechanism was via tunneling through the potential barrier in $V(\eta)$ keeping the quantization along the ξ coordinate intact. Finally, an excellent agreement between the experimental results and the quantum mechanical calculations was achieved, ipso facto validating the theoretical predictions made more than three decades ago and showing a new technique enabling the direct observations of electronic wave functions.

The nature of the ionization process governs whether the microscopic wave function $\chi_1(\xi)$, that exists in the vicinity of the atom, and the projection of the continuum

wave function, measured at a macroscopic distance, share the same nodal structure. In nonhydrogenic atoms the ionization occurs predominantly via the process (3), which prevents a successful measurement of electronic wave functions. However, this limitation can be overcome by enforcing a hydrogenic behavior either by populating states with small quantum defects or by taking a measurement in the vicinity of an avoided crossing, where the interference narrowing effect occurs. The latter approach was used in the experiments on helium atoms, whose results are presented and discussed in Chapter 6. 95% of the recorded images showed interference patterns similar to those presented in Chapter 4, hence without any imprint of the wave function, and in several cases, coinciding with the occurrence of the interference narrowing effect, the presence of the nodal structure of $\chi_1(\xi)$ was revealed. By that very fact it was demonstrated that photoionization microscopy may be a technique suitable for imaging wave functions in nonhydrogenic atoms. In Chapter 6 it is also shown that a "photoionization microscope" can be applied as a tool in the investigations of couplings between Stark states.

Samenvatting

De ontwikkeling van de kwantummechanica in het begin van de twintigste eeuw zorgde voor nieuw wiskundig gereedschap om natuurlijke fenomenen te beschrijven die zich op de nano-schaal afspelen en het veranderde de manier waarop wetenschappers de natuur begrijpen. Hoewel de theorie een kwalitatieve beschrijving geeft voor effecten die op de nano-schaal plaatsvinden, bevat het ook verscheidene elementen die klassiek niet intuïtief af te leiden zijn, zoals de golf-deeltjes dualiteit, het onzekerheidsprincipe van Heisenberg, het Pauli uitsluitingsprincipe enzovoorts. Een fundamentele rol in de kwantummechanica is weggelegd voor de golffunctie ψ, welke moet voldoen aan de tijdafhankelijke Schrödingervergelijking en alle informatie bevat over de dynamische eigenschappen van een kwantumsysteem op elk gegeven moment in tijd t. Vanuit theoretisch oogpunt is het mogelijk een golffunctie te beschrijven, maar een golffunctie experimenteel te observeren blijft uitdagend door zijn extreme gevoeligheid. Één van de eigenaardigheden van de kwantummechanica is dat de meeste pogingen om een golffunctie direct te observeren deze daadwerkelijk vernietigen in een proces dat *collapse* (ineenstorting) wordt genoemd. Toch zijn er in de afgelopen decennia vele directe en indirecte experimentele methodes voorgesteld, wat geresulteerd heeft in het afbeelden van de golffunctie van kwantumobjecten zoals het foton, atoomkernen, atomen en molekulen (Hoofdstuk 1).

In dit proefschrift wordt een nieuwe techniek – fotoionisatie-microscopie - aangewend om de elektrongolffunctie in atomen zoals waterstof en helium direct te observeren. Deze alternatieve techniek, die meer dan 30 jaar geleden is voorgesteld, maakt gebruik van een unieke eigenschap van het waterstof atoom dat zich in een statisch elektrisch veld bevindt. De symmetrie van zijn Hamiltoniaanse operator maakt het namelijk mogelijk dat de Schrödingervergelijking geschreven kan worden in parabolische coördinaten (ξ, η, φ). Hierdoor kan de golffunctie geschreven worden als: $\psi(\eta, \xi, \varphi) = \frac{1}{\sqrt{2\pi\xi\eta}}\chi_1(\xi)\chi_2(\eta)e^{im\varphi}$, waar $\chi_1(\xi)$ en $\chi_2(\eta)$ functies zijn die de elektronenbeweging langs de ξ en η coördinaat beschrijven en respectievelijk n_1 en n_2 knopen hebben. De getallen n_1 en n_2 zijn de zogenoemde parabolische kwantumgetallen. Zoals expliciet is aangetoond in hoofdstuk 2, bestaat er voor elke cordinaat een zekere effectieve potentiaal die op de elektronen werkt en resulteert in beweging langs de ξ coördinaat die altijd eindig is. Om ionisatie plaats te laten vinden moet het elektron daarom ontsnappen naar $\eta = \infty$. Dit is in twee gevallen mogelijk: (1) als het elektron genoeg energie heeft om de top van de $V(\eta)$ potentiaal te overbruggen of (2) wanneer de energie lager is dan het maximum van de $V(\eta)$ potentiaal, maar er een eindige waarschijnlijkheid is om door de barriére te tunnelen. In het laatste geval worden de ideale omstandigheden gecreëerd voor fotoionisatie-microscopie, omdat het tunnelproces de kwantisatie langs de ξ-coördinaat intact laat. De theorie voorspelt dat een afbeelding van zulke getunnelde foto-elektronen, op een tweedi-

mensionale detector die loodrecht op de richting van het statisch elektrisch veld is geplaatst, experimenteel een interferentiepatroon zou vertonen dat direct de knoopstructuur van de elektronengolffunctie $\chi_1(\xi)$ laat zien.

In dit proefschrift wordt de geldigheid van fotoionisatie-microscopie, als geschikte techniek voor het afbeelden van elektrongolffuncties, getest op twee fundamenteel verschillende (vanuit het oogpunt van de kwantummechanica) atomen: waterstof en helium. Het voornaamste doel van hoofdstuk 2 is om theoretische en experimentele gevolgen te presenteren van het eindige formaat van de ionenkern in helium en andere niet-waterstofachtige atomen. In vergelijking met waterstof, waar de kern slechts één enkel proton bevat. Het wordt aangetoond dat de niet–Coulombische potentiaal van niet-waterstofachtige atomen leidt tot koppelingen tussen Stark toestanden. Dit heeft tot gevolg dat zogenoemde vermeden kruisingen opkomen tussen niveaus die in waterstof zouden kruisen en een nieuw soort veldionisatiemechanisme plaatsvindt. Mechanisme (3): wanneer de energie van het elektron lager is dan het maximum van de $V(\eta)$ potentiaal, kan het elektron door de kern verstrooid worden in een andere parabolische toestand. Wanneer de energie van deze parabolische toestand boven de $V(\eta)$ barriére ligt, resulteert dit in een proces dat vergelijkbaar is met auto-ionisatie. Echter, dit type veldionisatie, welke een dominant vervalmechanisme is in niet-waterstofachtige atomen, verwijdert de kwantisatie langs de ξ-coördinaat en verzet zich daardoor tegen een meting van de elektronen golffunctie in niet-waterstofachtige atomen. Toch, zoals getoond in hoofdstuk 2, vindt er een bijzonder effect plaats in de buurt van vermeden kruisingen. Dit zogenoemde interferentieversmalling-effect, verandert het ionisatieproces en staat in principe een directe observatie van de knoopstructuur in $\chi_1(\xi)$ toe, zoals bestudeerd wordt in hoofdstuk 6.

Het idee van het afbeelden van golffuncties met fotoionisatie-microscopie in experimentele realiteit omzetten was zeker geen triviale opgave. Volgens de theoretische beschrijving zou een "fotoionisatie-microscoop"moeten bestaan uit twee platen die een homogeen elektrisch veld produceren, een straal van neutrale atomen, een gefocusseerde laserstraal die de atomen fotoioniseert, en een positiegevoelige detector die loodrecht op de elektrische veldrichting staat waar de fotoelektronen op kunnen worden geprojecteerd. Hoofdstuk 3 biedt een gedetailleerde beschrijving van de experimentele realisatie van dit concept, voor zowel waterstof als voor helium, aangezien de intrinsieke verschillen tussen deze atomen resulteerden in het ontwerpen van twee afzonderlijke experimentele opstellingen. Het waterstofatoom, in tegenstelling tot helium, bestaat niet als een chemisch stabiele soort in de natuur en daarom moest het in de experimenten geproduceerd worden door fotodissociatie van een H_2S molekuul. Hoge ionisatiebarriéres in de beide atomen sloten het originele idee van één-foton-excitatie vanuit de grondtoestand naar een hooggelegen Stark-toestand uit. Daarom zijn alternatieve foto-ionisatie concepten aangewend, welke gebruik maken van geprepareerde atomen die zich in metastabiele toestanden bevinden voordat ze foto-gexciteerd worden. Voor helium, wat als edelgas metastabiele toestanden heeft die immuun zijn voor een DC elektrisch veld, werd een ontladingsbron gebouwd die een straal van metastabiele (2^1S) heliumatomen leverde. Aangezien waterstof niet dezelfde eigenschap heeft, werd het gexciteerd naar een $n = 2$ toestand door het ab-

sorberen van twee fotonen met een golflengte van 243 nm. In dezelfde regio werd het vervolgens gexciteerd naar een Stark-toestand door het absorberen van één UV foton dat geleverd werd door een huisgemaakte, verstelbare, smalbandige, gepulseerde kleurstof versterker. De laatste foto-excitatie stap in de experimenten aan helium werd gedaan door gebruik te maken van een UV foton dat geproduceerd wordt door frequentieverdubbeling van licht uit een CW ring kleurstof laser. Om aan de eisen voor de homogeniteit van het elektrisch veld en de positiegevoelige detector te voldoen, werd gebruik gemaakt van een velocity map imaging spectrometer (VMIS). In dit apparaat werd een DC veld opgewekt door het aanleggen van een voltageverschil tussen de beide elektrodes, welke fungeerden als een elektrostatische lens die het mogelijk maakte om de gecreëerde fotoelektronen scherp te focusseren op de detector. In onze experimenten bestond de detector uit twee micro-channel plates (MCPs), een fosfor scherm en een CCD camera. Het laatste cruciale element in beide opstellingen was een Einzel-lens, welke zorgde voor een vergroting van de opgenomen fotoelektronen afbeeldingen van één ordegrootte. De berekende efficiëntie van het gehele proces in beide experimenten is gegeven in hoofdstuk 3, samen met de beschrijving van de voornaamste limiterende factoren in beide systemen.

Tijdens de fotoionisatie-microscopie-experimenten werden waterstof- en heliumatomen foto-geïoniseerd in de aanwezigheid van DC elektrische velden en de resulterende fotoelektronen werden op een detector geprojecteerd, wat karakteristiek oscillerende structuren creëerde. In de experimenten waar atomen door foto-excitatie in het continum van Stark-toestanden werden gexciteerd, oftewel wanneer het veldionisatieproces verliep via mechanisme (1), zijn de geobserveerde interferentiepatronen volledig begrepen. Hiervoor dient namelijk de faseaccumulatie, langs de verschillende banen die de fotoelektronen toestaan de tweedimensionale detector op dezelfde plaats te bereiken, in acht worden genomen. In hoofdstuk 4 worden de experimentele resultaten voor de waterstofatomen gepresenteerd, waar de genoemde interferentiepatronen worden geobserveerd en uitgelegd binnen het kader van de semiklassieke theorie. In de opgenomen afbeeldingen van de fotoelektronen worden verschillende oscillerende structuren onderscheiden die gerelateerd zijn aan de zogenoemde "directeën ïndirecteïonisatieprocessen. Deze verschillen in de omstandigheden waaronder het fotoelektron wordt gelanceerd, met andere woorden of het interageerde met het ion of niet. Hiermee is voor de eerste keer waargenomen dat directe en indirecte banen leiden tot golvende patronen in het centrale gedeelte van de afbeeldingen van de fotoelektronen. Dit effect is verder in detail bestudeerd en zeer goed gereproduceerd door semiklassieke berekeningen.

Volgens de theorie achter fotoionisatie-microscopie toont het geobserveerde interferentiepatroon, in het bijzondere geval dat de fotoionisatie volgt op een resonante excitatie naar een Stark-toestand, direct de knoopstructuur van de Stark-toestand die in het experiment wordt voorbereid. Dit resonante effect is uitgebreid onderzocht in hoofdstuk 5, waar de opgenomen afbeeldingen van de fotoelektron voor waterstofatomen, die geëxciteerd zijn naar verschillende Stark-toestanden, worden gepresenteerd. Opvallend genoeg is het aantal geobserveerde donkere ringen gelijk aan n_1, oftewel aan het aantal knopen van de elektrongolffunctie $\chi_1(\xi)$, ongeacht de laserpolarisatie of de sterkte van het elektrisch veld. Om te bevestigen dat de geob-

serveerde interferentiestructuren worden veroorzaakt door het resonante effect, zijn afbeeldingen van de fotoelektronen opgenomen voor energien die onder en boven de Stark-toestand lagen. In deze niet-resonante gevallen hebben de interferentiepatronen minder ringen en kan hun herkomst volledig worden begrepen. Hiervoor dient men kwantummechanische padlengteverschillen in acht te nemen die de het fotoelektron ervaart langs de verschillende interfererende paden, zoals gepresenteerd wordt in hoofdstuk 4. Verder moet vermeld worden dat de opgenomen afbeeldingen zich radiaal verder uitbreiden, wat lijkt te wijzen op betrokkenheid van een kwantum effect, aangezien de fotoelektronen klassiek verboden posities op de detector bereiken. Deze waarneming bevestigt dat het ionisatie mechanisme verliep via het tunnelen door de potentiaal barriére in $V(\eta)$, waardoor de kwantisatie langs de ξ-coördinaat behouden blijft. Tot slot is er een uitstekende overeenkomst bereikt tussen de experimentele resultaten en de kwantummechanische berekeningen. Dit bekrachtigt ipso facto de theoretische voorspellingen van drie decennia geleden en toont aan dat deze techniek een directe waarneming van elektrongolffuncties mogelijk maakt.

De aard van het ionisatieproces bepaalt of de microscopische golffunctie $\chi_1(\xi)$, die bestaat in de nabijheid van het atoom, en de afbeelding van de continumgolffunctie, gemeten op een macroscopische afstand, dezelfde knoopstructuur hebben. In niet-waterstofachtige atomen vindt ionisatie voornamelijk plaats via mechanisme (3), wat een succesvolle meting van de golffunctie voorkomt. Echter, deze beperking kan overwonnen worden door een waterstofachtig gedrag op te leggen. Dit kan ofwel door het vullen van toestanden met kleine kwantumdefecten of door een meting te doen in de buurt van een vermeden kruising, waar het interferentie versmalling effect plaatsvindt. De laatstgenoemde aanpak is gebruikt in de experimenten aan heliumatomen, waarvan de resultaten worden gepresenteerd en bediscussieerd in hoofdstuk 6. Ongeveer 95% van de opgenomen afbeeldingen toont interferentiepatronen vergelijkbaar met die uit hoofdstuk 4, maar dan zonder enige afdruk van de golffunctie. In verschillende gevallen vindt ook het interferentieversmalling-effect plaats, waarmee de aanwezigheid van de knoopstructuur van $\chi_1(\xi)$ was ontdekt. Door dat simpele feit is het aangetoond dat fotoionisatie-microscopie mogelijk een geschikte techniek is voor het afbeelden van golffuncties in niet-waterstofachtige atomen. In hoofdstuk 6 wordt ook getoond dat een "fotoionisatie-microscoop"kan worden aangewend als techniek in het onderzoek naar koppelingen tussen Stark-toestanden.

Acknowledgements

In my life I experienced a variety of exotic and astonishing travels, but my PhD was the journey that cost me the most energy, led to countless ups and downs and brought all kinds of emotions in return: from total hopelessness to entire satisfaction and happiness. During these few years of my doctorate I met numerous inspiring and helpful people without whom this journey would have never ended successfully. On top of that a sincere support of my family and friends helped me immensely during some rough times. Therefore, the last pages of this book I devote to these essential people and hopefully in a few simple thank words I will express my honest gratefulness to all of them.

First of all, I would like to thank my supervisor Marc Vrakking for giving me an opportunity to start a PhD in his group at AMOLF despite our "disagreement" during the job interview. Marc, I am grateful for your confidence in entrusting me with the photoionization microscopy project, which turned out to be a true challenge and at a certain point almost an impossible task, but with your motivation and support it became a world-wide success. I was really lucky to had you as my supervisor since you always had time for discussion, ridiculously even more when you moved to Berlin, had always plan "B" or even "C" when things were getting off the trajectory and have such a versatile knowledge of science and technology that there was always a solution to my problems. During my PhD I have learnt a lot from you and I appreciate the chance of *climbing Mount Everest* together – it was a pleasure and honor to work with you.

My PhD project would have never been successful without the supporting staff of AMOLF, which is one of its kind and ensures smooth and pleasant research. I would like to sincerely thank Rob for being the best technician a PhD student could wish for. Rob, I am thankful not only for your exceptional assistance in the lab, which was always quick and efficient, but also for your kindness, life-wisdom and useful advices. You are a wonderful person and I wish you all the best during your retirement. I want to thank Hinco for being our unofficial group technician on Fridays and for proving a helping hand despite lack of time. Moreover, I am thankful to Ad for teaching me the first steps with the ring-dye laser and for his sincere interest in my research even after he left the group. My experiments would not have been successful without state-of-the-art machines, which were designed and built at AMOLF. Therefore, I wish to thank the Design Department, especially Iliya for his accessibility and creativity in providing emergency solutions to my numerous disasters in the lab. Many thanks to Henk-Jan for his patience with creating beautiful figures of experimental setups for our publications and this thesis. The Mechanical Workshop in AMOLF is simply the best in manufacturing high quality parts thanks to people working there, in particular Henk, Menno and Niels, and their great manager Wim. Thank you all

for an incredible cooperation in the last few years when you never said NO to my sophisticated requests and always delivered adequate parts in no time. From the Electronic Engineering I would like to thank Duncan for his assistance in many projects, Ronald for countless repairs of the control box and making kilometers of cables for my experiments, Idsart for his support with high voltage elements and Henk for solving the biggest problem during my PhD. Many thanks to the Software Engineering, in particular to Marco Konijnenburg for making my work with Lisa Cluster completely effortless and to Marco Seynen for ensuring connection to my very old laser control computer. Sincere thanks to the ICT department, especially to Carl, Jan, Rutger and Wiebe for their excellent assistance during all these years. Finally, I would like to acknowledge people from other supportive departments in AMOLF: Anuok, Arnelli, Erny, Grace, Tatiana, Silvia, Willem, Wouter for their support, kind words and smile in AMOLF's corridors.

The work presented in this thesis is a result of collaboration with several brilliant scientists and researchers with whom I had the pleasure to work over last few years. Franck Lépine deserves honest thanks for his great contribution to the hydrogen experiment and assistance afterwards. Franck, I am grateful for the time spent together in the lab, your wise suggestions and advises, many theoretical discussions and black humor that made me laugh despite tiredness and late hours. I would like to acknowledge Francis Robicheaux for developing the wave packet code, which I used for many calculations presented in this thesis, as well as for explaining its complicated theory. Many thanks to Christian Bordas for his input to our publications. Moreover, I would like to express my gratitude to Tom Bergeman for his indispensable assistance in the interpretation of He photoionization spectra, especially for bringing back to life his old computer code, the final version of which got lost many years ago. Tom, I wish I could meet you in person to thank you for all those dozens of e-mails that we exchanged over last few years. Finally, I would like to thank Wim Vassen for his precious hints on designing and building the metastable helium source.

After my first year of PhD I became a part of the ICONIC network where I had a chance to learn a lot about different applications of the velocity map imaging technique. I would like to acknowledge the funders for giving me the opportunity to be a member of this organization and for numerous meetings and schools during which I could share my knowledge with other PhD students and postdocs. In particular I would like to thank my mentor Benjamin Whitaker for his interest in my research and stimulating discussions. I am thankful to Dave Parker for his warm welcome and to Wim van der Zande for his challenging questions which motivated me to broaden my knowledge. Many thanks to André Eppink for arranging all these great meetings, schools and dinners. Lastly, I wish to thank all other members of ICONIC for great times we had together, for their support and friendship.

People with whom I worked every day – my terrific colleagues – had a huge impact on my PhD project. From the XUV group in AMOLF I wish to thank Julia for being an amazing companion who truly shared all my ups and downs during all these years. Julia, I am thankful for your compassion, helping hand in the lab, hours of discussions, wise advises and suggestions, and of course our morning gossip sessions

and passion for chocolate ;-) You turned out to be not only the best office mate, super-helpful colleague, but also a true friend I could always count on. Many thanks to Arjan who taught me useful tricks in the lab boosting my confidence in performing experiments and gave me the best advice during my whole PhD. Arnaud, thank you for coming from Berlin and fixing my experiment within 48 hours as you promised! Ymkje, the Felice campaign under your supervision was simply the best as three of us created an unbeatable team of girls that performed a superb experiment despite all doubts of some of our male colleagues. Thank you for that great experience and for always being super helpful, friendly and very funny ;-) Many thanks to Georg, Freek and Wing Kiu for all inspiring discussions, exciting group *uitjes*, delicious dinners, and great parties – especially the one with terrible sangria! I wish to express my gratitude to Jesse for translating my summary into Dutch and also for going out with me for countless dinners in Berlin. The latter also applies to my other amazing colleagues from Berlin: Axel, Christian, ChungHsin, Faruk, Fede and Martin. Thank you all for being fantastic hosts and your efforts at showing me the city – especially by night! Moreover, Fede thank you one more time for all your suggestions and tips regarding our holidays in Argentina and Faruk for advising us Cay Caulker which turned out to be one of the best places we visited during our RTW trip!

Halfway through my PhD the whole XUV group moved to Berlin while I stayed in Amsterdam for the next couple of years. I am grateful to Huib Bakker, who became my official supervisor, for always finding time to discuss progress in my PhD project. Moreover, I wish to thank Ron Heeren for "adopting" me into his group so I had never felt redundant or alone. Moreover, many thanks to people from the BIMS group for always being enjoyable and friendly. In particular I am thankful to Andras, Don, Julia, Gert and Marc for all those fantastic lunches that we had together. Finally, to all my colleagues I forgot to mention – thanks a lot!

The final year of my PhD was really tough for me due to some health problems. However, I was lucky to meet great specialists who spent months on massaging and mobilizing my arm so I was able to work with a computer again. I would like to acknowledge Gerard Vierbergen for his patience in fixing all my new injuries, for his optimism and great stories which were always cheering me up. Many thanks to Jolanda van der Peet for very painful dry needling therapy which helped me enormously. I am thankful to Marty Cook for his alternative treatments which were restoring a balance in my body and mind.

The time of my PhD would not be so enjoyable without my awesome friends - old ones from Poland and new ones that I have met in the Netherlands. Many thanks to absolutely wonderful friends from Alkmaar: Claire and Marc, Ingrid and Hans, Nicolas, Gaga and Ben, Ellen and Tom, Raimo, Anna and Annelies, Lydia and Pichon, Virginie and Alain, Soledad, Maria and Goulven for all delicious dinners, BBQs, drinks in *Bier Museum*, litters of La Chouffe in *Provadja*, poker nights, Sinterklaas celebrations, Gondelvaarten in Koedijk and mostly for our crazy parties in the infamous bake-shed! Gorące podziękowania dla naszej wspaniałej, aczkolwiek nielicznej Polonii z południowo-centralnej Holandii: Magdy i Alicji. Dziewczyny, dzięki wielkie za wszystkie szalone weekendy spędzone razem, zapoznanie nas z elitarnym klubem *International*, a przede wszystkim za Wasze zrozumienie oraz wsparcie w

kwestiach polsko-holenderskich. Chciałabym również podziękować wyjątkowej grupie przyjaciół z Gdańska: Ani, Mai, Stachowi, Jackowi, Agacie, Michałowi, Maćkowi, Soni, Martynce i Piotrkowi za wszystkie ciepłe powitania i pożegnania w *Stacji De Luxe*, Wasze wizyty w Alkmaar, wspólne wyjazdy na narty bądź do Ekwadoru lub Malezji oraz za fakt pozostawania w bardzo dobrych kontaktach pomimo setek kilometrów które nas dzielą! Moim szalonym i cudownym przyjaciółkom z podwórka: Ani, Agnes, Kasi i Judycie jestem wdzięczna za ich wsparcie oraz wszystkie cudowne chwile spędzone razem.

Z całego serca pragnę podziękować moim dwóm wspaniałym rodzinom: Smółkowskim i Stodólnym za ich nieustającą pomoc, wyjątkowe wsparcie oraz gorący doping w trakcie mojego doktoratu. Mamie Danusi i tacie Leszkowi jestem ogromnie wdzięczna za ich trud w wychowaniu mnie na osobę ambitną, która nieprzerwanie dąży do wyznaczonego celu, ponieważ bez tej silnej cechy charakteru (częściowo odziedziczonej po Was) nigdy nie osiągnęłabym tak wiele. Ta książka jest poniekąd owocem Waszej ciężkiej pracy w zapewnieniu mi najlepszego wykształcenia. Ogromne podziękowania dla mamy Ewy i taty Krzysia za ich gorące przyjęcie do rodziny, zainteresowanie w postępach mojego doktoratu, liczne toasty za wszelkie sukcesy jak i również za bardzo ciekawe dysputy naukowe oraz gorliwe pytania odnoście "moich atomów". Mojej kochanej siostrzyczce Inusi chciałabym podziękować za jej cudowne wsparcie w trudnych chwilach, szczerą radość z moich sukcesów oraz za bardzo dobre porady techniczno-naukowe jakich nie spodziewałabym się po tak młodej osobie - jednym słowem jest z Ciebie bardzo dobry materiał na naukowca! Ogromny buziak dla Moni za nadanie ostatnich szlifów angielskiej wersji podziękowań. Arkowi i Asi dziękuję za liczne odwiedziny w Holandii. Wszystkim pozostałym Smółkom i Stodólniakom dziękuje również gorąco!

Last but not the least I wish to thank my husband Maciej for being the best travel buddy, a wonderful life partner and an outstanding scientist with whom I had many stimulating discussions regarding my research. Maciej, the most I am thankful for your remarkable support in the last year of my PhD, when I had to stop working for a few months and you overtook all my household duties (every wife dreams of that). Moreover, you became my personal secretary who typed dozens of e-mails and to spare me many working hours with a computer you edited figures for this thesis and put the whole text into LaTeX. Without your help, advice, patience and love I would have never finished this book and therefore I dedicate it to you.

Aneta S. Stodolna, Southeast Asia, April 2014

List of publications

- *Visualizing the coupling between red and blue Stark states using photoionization microscopy*, A.S. Stodolna, F. Lépine, T. Bergeman, F. Robicheaux, A. Gijsbertsen, J.H. Jungmann, C. Bordas and M.J.J. Vrakking, (*submitted for publication*).

- *Photoelectron holography in strong optical and dc electric fields*, A.S. Stodolna, Y. Huismans, A. Rouzée, F. Lépine and M.J.J. Vrakking, (*to be published in the Journal of Physics: Conference Series*).

- *Hydrogen atoms under magnification: Direct Observation of the Nodal Structure of Stark States*, A.S. Stodolna, A. Rouzée, F. Lépine, S. Cohen, F. Robicheaux, A. Gijsbertsen, J.H. Jungmann, M.J.J. Vrakking, Phys. Rev. Lett. **110**, 213001 (2013).

- *Photoelectron angular distributions from the ionization of xenon Rydberg states by midinfrared radiation*, Y. Huismans, A. Rouzée, A. Gijsbertsen, P. S. W. M. Logman, F. Lépine, C. Cauchy, S. Zamith, A. S. Stodolna, J. H. Jungmann, J. M. Bakker, G. Berden, B. Redlich, A. F. G. van der Meer, K. J. Schafer, and M. J. J. Vrakking, Phys. Rev. A **87**, 033413 (2013).

- *Scaling laws for photoelectron holography in the midinfrared wavelength regime,* Y. Huismans, A. Gijsbertsen, A.S. Smolkowska (Stodolna), J.H. Jungmann, A. Rouzée, P.S.W.M. Logman, F. Lépine, C. Cauchy, S. Zamith, T. Marchenko, J.M. Bakker, G. Berden, B. Redlich, A.F.G. van der Meer, M.Yu. Ivanov, T.-M. Yan, D. Bauer, O. Smirnova and M.J.J. Vrakking, Phys. Rev. Lett. **109**, 013002 1-5 (2012).

- *Time-resolved holography with photoelectrons,* Y. Huismans, A. Rouzée, A. Gijsbertsen, J.H. Jungmann, A.S. Smolkowska (Stodolna), P.S.W.M. Logman, F. Lépine, C. Cauchy, S. Zamith, T. Marchenko, J.M. Bakker, G. Berden, B. Redlich, A.F.G. van der Meer, H.G. Muller, W. Vermin, K.J. Schafer, M. Spanner, M.Yu. Ivanov, O. Smirnova, D. Bauer, S.V. Popruzhenko and M.J.J. Vrakking, Science **331**, 61-64 (2011).

- *Yrast structure of the two-proton- and threeneutron-hole nucleus* ^{203}*Hg from the decay of a* $53/2^+$ *isomer,* B. Szpak, K.H. Maier, A.S. Smolkowska (Stodolna), B. Fornal, R. Broda, M.P. Carpenter, N. Cieplicka, R.V.F. Janssens, W. Krolas, T. Pawlat. J. Wrzesinski and S. Zhu, Phys. Rev. C **83**. 064315 (2011).

About the author

Aneta Sylwia Stodólna (Smółkowska) was born in Ostróda, North-East Poland in 1984. She spent her childhood and attended primary school in Samborowo. In 2003 Aneta graduated with honors from Secondary School no.1 in Olsztyn in biological-chemistry class. She bet on physics and studied at Gdansk University of Technology on the Faculty of Applied Physics and Mathematics for 5 years. During that period she did several scientific internships. The first was at the Henryk Niewodniczanski Institute of Nuclear Physics, Department of the Structure of Nucleus, Cracow, Poland. The second was at the National Institute of Nuclear Physics, Legnaro, Italy. She has done a half-year schooling at AGH University of Science and Technology, Faculty of Physics and Applied Computer Science, Cracow, Poland with special emphasis on nuclear physics. She worked there in the field of "Yrast structure in neutron–rich nuclei from the vicinity of doubly magic ^{208}Pb", which was the main topic of her Master's thesis. In June 2008 Aneta received a M.Sc. degree cum laude in Applied Physics. Between July 2008 and March 2009 she worked at Katholieke Universiteit Leuven, Institute for Nuclear and Radiation Physics, Belgium, designing and building a new facility for Collinear Resonant Ionization Spectroscopy at the ISOLDE hall at CERN, Switzerland to investigate the structure of exotic nuclei. In March 2009 Aneta started her PhD research at FOM Institute for Atomic and Molecular Physics (AMOLF), Amsterdam, the Netherlands in the group of Extreme-Ultraviolet Physics. Aneta's research – photoionization microscopy of H and He atoms – brought an experimental proof of a quantum theory developed in the 1980's and allowed direct observation of one of the most elusive quantum objects – the wave function. Her recent paper in *Physics Review Letter* on "Hydrogen Atoms under Magnification: Direct Observation of the Nodal Structure of Stark States" received a significant attention in the scientific media all over the world and was highlighted in the top scientific journals as *Nature*, *Nature Nanotechnology*, *Science*, *European Physics Society*, *New Scientists* and *Physics World*. Furthermore, this work was chosen as one of the TOP 10 Breakthroughs in Physics in 2013 awarded by *Physics World*.